

A robust, high-order implicit shock tracking method for simulation of complex, high-speed flows

Tianci Huang^{a,1}, Matthew J. Zahr^{a,2,*}

^a*Department of Aerospace and Mechanical Engineering, University of Notre Dame, Notre Dame, IN 46556, United States*

Abstract

High-order implicit shock tracking (fitting) is a new class of numerical methods to approximate solutions of conservation laws with non-smooth features, e.g., contact lines, shock waves, and rarefactions. These methods align elements of the computational mesh with non-smooth features to represent them perfectly, allowing high-order basis functions to approximate smooth regions of the solution without the need for nonlinear stabilization, which leads to accurate approximations on traditionally coarse meshes. The hallmark of these methods is the underlying optimization formulation whose solution is a feature-aligned mesh and the corresponding high-order approximation to the flow; the key challenge is robustly solving the central optimization problem. In this work, we develop a robust optimization solver for high-order implicit shock tracking methods so they can be reliably used to simulate complex, high-speed, compressible flows in multiple dimensions. The proposed method integrates practical robustness measures into a sequential quadratic programming method that employs a Levenberg-Marquardt approximation of the Hessian and line-search globalization. The robustness measures include dimension- and order-independent simplex element collapses, mesh smoothing, and element-wise solution re-initialization, which prove to be necessary to reliably track complex discontinuity surfaces, such as curved and reflecting shocks, shock formation, and shock-shock interaction. A series of nine numerical experiments—including two- and three-dimensional compressible flows with complex discontinuity surfaces—are used to demonstrate: 1) the robustness of the solver, 2) the meshes produced are high-quality and track continuous, non-smooth features in addition to discontinuities, 3) the method achieves the optimal convergence rate of the underlying discretization even for flows containing discontinuities, and 4) the method produces highly accurate solutions on extremely coarse meshes relative to approaches based on shock capturing.

Keywords: Shock tracking, shock fitting, high-order methods, discontinuous Galerkin, numerical optimization, high-speed flows

1. Introduction

High-order methods such as discontinuous Galerkin (DG) methods [9, 22] offer a number of advantages for high-fidelity simulation of fluid flow including high accuracy per degree of freedom, low dissipation, geometric flexibility, and a high degree of parallel scalability. However, for high-speed flows that contain shocks and other discontinuities, spurious oscillations arise that degrade the approximation accuracy and usually lead to failure of the simulation. These nonlinear instabilities become increasingly problematic as the strength of the shock increases. The development of robust and accurate approaches to stabilize high-order approximations near shocks is critical to make them competitive for real-world problems [43].

Several approaches have been proposed to stabilize shocks, most of which are based on shock capturing, where the numerical discretization accounts for discontinuities on a fixed computational grid. Limiters, used to limit the gradient of the solution in the vicinity of shocks, are commonly used with second-order finite volume methods [41] and high-order DG methods [9] to yield total variation diminishing schemes; these

*Corresponding author

Email addresses: thuang5@nd.edu (Tianci Huang), mzahr@nd.edu (Matthew J. Zahr)

¹Graduate Student, Department of Aerospace and Mechanical Engineering, University of Notre Dame

²Assistant Professor, Department of Aerospace and Mechanical Engineering, University of Notre Dame

methods are widely accepted and commonly used to simulate real-world flows [6]. Weighted essentially non-oscillatory (WENO) methods [19, 29, 23] use a high-order reconstruction with a stencil tailored to the flow solution to mitigate spurious oscillations in the solutions near shocks. These methods lead to crisp shocks, although they require a large stencil and have not been demonstrated on unstructured meshes for practical problems. For high-order methods, artificial viscosity has also proven to be competitive, and has emerged as the preferred method for finite-element-based methods [33, 2, 14, 7] because it can smoothly resolve steep gradients with sub-cell accuracy. A recent comparative study of artificial viscosity models [44] discusses their relative merits, but notes they all suffer from a relatively strong dependency on a large number of empirical parameters that must be tuned. The main problem with all these approaches is that they are first-order near the shock, which translates into a globally first-order accurate scheme. This can be remedied by using local mesh refinement around the shock (h -adaptivity) [13], although the anisotropic elements that are required for efficiency are difficult to generate and extremely fine elements are needed near the shock.

An alternative approach is so-called *shock tracking* or *shock fitting*, where the computational mesh is moved to align faces of mesh elements with the solution discontinuities, representing them perfectly with the inter-element jump in the solution basis without requiring additional stabilization. However, it is a difficult meshing problem since it essentially requires generating a fitted mesh to the (unknown) shock surface. Most of these methods employ specialized formulations and solvers which are dimension-dependent and do not easily generalize [18, 17, 3] and/or are limited to relatively simple problems [38, 39, 42]. In addition, early approaches to shock tracking have been applied to low-order schemes where the relative advantage over shock capturing is smaller than for high-order methods [40, 1]. One popular class of methods that we will call explicit shock tracking is surveyed in [31, 37]. These methods largely consist of explicitly identifying the shock and using the Rankine-Hugoniot conditions to compute its motion and states upstream and downstream of the shock. More recent developments in explicit shock tracking [35] use more sophisticated methods to compute shock velocities and discretize the flow equations; however, they ultimately still require a specialized strategy to explicitly track the shock separately from the remainder of the flow. These methods are not easily applicable to discontinuities whose topologies are not known *a priori*. While interest in shock tracking/fitting has seen somewhat of a resurgence in recent years [8, 4, 15, 12], shock tracking is not widely used for practical applications.

A new class of high-order numerical methods has recently emerged, *implicit shock tracking*, that includes the High-Order Implicit Shock Tracking (HOIST) method [45, 48, 47] and the Moving Discontinuous Galerkin Method with Interface Condition Enforcement (MDG-ICE) [10, 24, 25]. Like traditional shock tracking, these methods align element faces with discontinuity surfaces to represent them perfectly and the high-order basis functions approximate the smooth solution away from shocks. The key difference is the implicit shock tracking methods do not attempt to explicitly generate a mesh fitted to the unknown discontinuity surface, e.g., by treating the discontinuity as an interior boundary. Rather, they discretize the conservation law on a mesh without knowledge of the flow field and pose an optimization problem over the discrete flow variables and nodal coordinates of the mesh whose solution is a discontinuity-aligned mesh and the corresponding flow solution. That is, discontinuity tracking is achieved implicitly through the solution of an optimization problem. This is the critical innovation that has overcome the limitations of explicit shock tracking and led to a general approach that is not tailored to the governing equations or specific flow problem (equation- and problem-independent), only requires one simple topological mesh operation (element removal), and is able to handle intricate shock structures (curved and reflecting shocks, shock formation, and shock-shock interaction). As such, implicit shock tracking has been used to solve steady and unsteady, viscous and inviscid, inert and reacting flows of varying degrees of complexity. While these methods have shown considerable promise, they are still lacking a robust solver for the underlying optimization problem that converges efficiently and reliably to a discontinuity-aligned mesh with high-quality elements for high Mach flows with complex discontinuity structures. This is the gap this work aims to fill.

We propose a series of algorithmic developments to the HOIST method to improve its automation and robustness, although many of the developments will apply to MDG-ICE with minor modifications. The HOIST method is based on a high-order DG discretization of the governing equations and formulates implicit tracking as an optimization problem constrained by the DG residual to endow the method with the desirable properties of DG: consistency, conservation, and stability. The objective function penalizes violation of the DG residual in an enriched test space; it is a surrogate for violation of the infinite-dimensional weak formulation of the conservation law, which endows the method with r -adaptive behavior. The optimization

problem is solved using a sequential quadratic programming (SQP) method with a Levenberg-Marquardt Hessian approximation that simultaneously converges the mesh and flow solution to their optimal values, which never requires the fully converged DG solution on a non-aligned mesh and therefore does not require nonlinear stabilization. The contributions of this paper are summarized as follows.

- We develop a general, automated procedure to guarantee planar boundaries and their intersections will be preserved as the computational mesh moves to align with shocks and detail its implementation.
- We develop a new solver for the implicit tracking optimization problem based on the SQP solver in [48]. The new solver features a new merit function penalty parameter, an adaptive penalty parameter for the mesh distortion term in the objective function, and, most importantly, a number of practical robustness measures. The most critical robustness measures are dimension- and order-independent simplex element removal via edge collapse that preserves the boundaries of the domain and the tracked shocks (to high-order) and element-wise solution re-initialization that resets the solution in oscillatory elements, identified with standard shock sensors [33], to a constant value to promote high-quality SQP steps.
- We demonstrate implicit shock tracking, when equipped with robust solvers, is practical for two-dimensional, compressible flows with intricate shock structures (curved and reflecting shocks, shock formation, and shock-shock interaction); three-dimensional, compressible flows with a curved bow shock; and high Mach flows.

The remainder of the paper is organized as follows. Section 2 introduces the governing system of inviscid conservation laws, its reformulation on a fixed reference domain, and its discretization using a discontinuous Galerkin method. Section 3 constructs the space of admissible domain mappings (i.e., mesh motion) using nodal basis functions associated with a mesh of the reference domain and a parametrization that guarantees the mapping will approximate the boundary of the physical domain to high-order accuracy; a general, automated procedure to construct the parametrization is introduced for the special case where the boundary is piecewise planar. Section 4 recalls the implicit shock tracking formulation originally proposed in [48] that incorporates the boundary-preserving parametrization of the nodal coordinates. Section 5 introduces the SQP solver with the new robustness measures. Finally, Section 6 presents a series of nine increasingly difficult numerical experiments that demonstrate the robustness of the solver, the high accuracy per degree of freedom of the method, and ability of the method to handle two- and three-dimensional compressible flows with complex features (curved and reflecting shocks, shock formation, and shock-shock interaction).

2. Governing equations and high-order discretization

In this section, we introduce the governing partial differential equations (steady or space-time, inviscid conservation law) (Section 2.1), its transformation to a reference domain so that domain deformations appear explicitly in the governing equations (Section 2.2), and its discretization via a high-order DG method (high-order with respect to both the solution and geometry) (Section 2.3).

2.1. System of conservation laws

Consider a general system of m inviscid conservation laws, defined on the fixed domain $\Omega \subset \mathbb{R}^d$ and subject to appropriate boundary conditions,

$$\nabla \cdot F(U) = S(U) \quad \text{in } \Omega, \quad (1)$$

where $U : \Omega \rightarrow \mathbb{R}^m$ is the solution of the system of conservation laws, $F : \mathbb{R}^m \rightarrow \mathbb{R}^{m \times d}$ is the flux function, $S : \mathbb{R}^m \rightarrow \mathbb{R}^m$ is the source term, $\nabla := (\partial_{x_1}, \dots, \partial_{x_d})$ is the gradient operator in the physical domain, and the boundary of the domain $\partial\Omega$ has outward unit normal $n : \partial\Omega \rightarrow \mathbb{R}^d$. The formulation of the conservation law in (1) is sufficiently general to encapsulate steady conservation laws in a d -dimensional spatial domain or time-dependent conservation laws in a $(d-1)$ -dimensional domain, i.e., a d -dimensional space-time domain. In general, the solution $U(x)$ may contain discontinuities, in which case, the conservation law (1) holds away from the discontinuities and the Rankine-Hugoniot conditions [30] hold at discontinuities.

2.2. Transformed system of conservation laws on a fixed reference domain

Before discretizing (1), it is convenient to explicitly treat deformations to the domain of the conservation law Ω —such deformations will eventually be induced by deformation to the mesh as nodal coordinates are moved to track discontinuities—by transforming to a fixed reference domain $\Omega_0 \subset \mathbb{R}^d$. Let \mathbb{G} be the collection of diffeomorphisms from the reference domain Ω_0 to the physical domain Ω , i.e., for any $\mathcal{G} \in \mathbb{G}$, we have

$$\mathcal{G} : \Omega_0 \rightarrow \Omega, \quad \mathcal{G} : X \mapsto \mathcal{G}(X). \quad (2)$$

Following the approach in [45], for any $\mathcal{G} \in \mathbb{G}$, the conservation law on the physical domain Ω is transformed to a conservation law on the reference domain Ω_0 as

$$\bar{\nabla} \cdot \bar{F}(\bar{U}; G) = \bar{S}(\bar{U}; g) \quad \text{in } \Omega_0, \quad (3)$$

where $\bar{U} : \Omega_0 \rightarrow \mathbb{R}^m$ is the solution of the transformed conservation law, $\bar{F} : \mathbb{R}^m \times \mathbb{R}^{d \times d} \rightarrow \mathbb{R}^{m \times d}$ is the transformed flux function, $\bar{\nabla} := (\partial_{X_1}, \dots, \partial_{X_d})$ is the gradient operator on the reference domain, and the deformation gradient $G : \Omega_0 \rightarrow \mathbb{R}^{d \times d}$ and mapping Jacobian $g : \Omega_0 \rightarrow \mathbb{R}$ are defined as

$$G = \bar{\nabla} \mathcal{G}, \quad g = \det G. \quad (4)$$

The unit outward normal to the reference domain is denoted $N : \partial\Omega_0 \rightarrow \mathbb{R}^d$ and related to the unit normal in the physical domain by

$$n \circ \mathcal{G} = \frac{g G^{-T} N}{\|g G^{-T} N\|}. \quad (5)$$

For any $X \in \Omega_0$, the transformed and physical solution are related as

$$\bar{U}(X) = U(\mathcal{G}(X)) \quad (6)$$

and the transformed flux and source term are defined as

$$\bar{F} : (\bar{W}; \Theta) \mapsto (\det \Theta) F(\bar{W}) \Theta^{-T}, \quad \bar{S} : (\bar{W}; q) \mapsto q S(\bar{W}). \quad (7)$$

Remark 1. In general, the reference domain can be defined such that it maps to the physical domain under the action of a smooth, invertible mapping $\hat{\mathcal{G}} : \mathbb{R}^d \rightarrow \mathbb{R}^d$, i.e., $\Omega_0 = \hat{\mathcal{G}}^{-1}(\Omega)$. In this work, we take the reference and physical domains to be the same set, i.e., $\hat{\mathcal{G}} = \text{Id}$.

2.3. Discontinuous Galerkin discretization of the transformed conservation law

We use a nodal discontinuous Galerkin method [9, 22] to discretize the transformed conservation law (3). Let \mathcal{E}_h represent a discretization of the reference domain Ω_0 into non-overlapping, potentially curved, computational elements. To establish the finite-dimensional DG formulation, we introduce the DG approximation (trial) space of discontinuous piecewise polynomials associated with the mesh \mathcal{E}_h

$$\mathcal{V}_h^p = \{v \in [L^2(\Omega_0)]^m \mid v|_K \in [\mathcal{P}_p(K)]^m, \forall K \in \mathcal{E}_h\}, \quad (8)$$

where $\mathcal{P}_p(K)$ is the space of polynomial functions of degree at most $p \geq 1$ on the element K . Furthermore, we define the space of globally continuous piecewise polynomials of degree q associated with the mesh \mathcal{E}_h as

$$\mathcal{W}_h = \{v \in C^0(\Omega_0) \mid v|_K \in \mathcal{P}_q(K), \forall K \in \mathcal{E}_h\} \quad (9)$$

and discretize the domain mapping with the corresponding vector-valued space $[\mathcal{W}_h]^d$.

Taking the DG test space to be $\mathcal{V}_h^{p'}$, where $p' \geq p$, the DG formulation is: given $\mathcal{G}_h \in [\mathcal{W}_h]^d$, find $\bar{U}_h \in \mathcal{V}_h^p$ such that for all $\bar{\psi}_h \in \mathcal{V}_h^{p'}$, we have

$$\int_{\partial K} \bar{\psi}_h^+ \cdot \bar{\mathcal{H}}(\bar{U}_h^+, \bar{U}_h^-, N_h; \bar{\nabla} \mathcal{G}_h) dS - \int_K \bar{F}(\bar{U}_h; \bar{\nabla} \mathcal{G}_h) : \bar{\nabla} \bar{\psi}_h dV = \int_K \bar{\psi}_h \cdot \bar{S}(\bar{U}_h; \det(\bar{\nabla} \mathcal{G}_h)) dV, \quad (10)$$

where $N_h : \partial K \rightarrow \mathbb{R}^d$ is the unit outward normal to element $K \in \mathcal{E}_h$, \bar{W}_h^+ (\bar{W}_h^-) denotes the interior (exterior) trace of \bar{W}_h to the element K for $\bar{W}_h \in \mathcal{V}_h^s$ for any $s \in \mathbb{N}$ (for $X \in \partial K \cap \partial\Omega_0$, \bar{U}_h^- is a boundary state constructed to enforce the appropriate boundary condition). Furthermore, $\bar{\mathcal{H}} : \mathbb{R}^m \times \mathbb{R}^m \times \mathbb{R}^d \times \mathbb{R}^{d \times d} \rightarrow \mathbb{R}^m$ is the numerical flux function associated with the reference inviscid flux \bar{F} , which ensures the boundary integral is single-valued and can be constructed to ensure the DG discretization is consistent, conservative, and stable [22]. An expression for the reference numerical flux function can be obtained from the standard physical numerical flux function [48]. The residual form of the DG equation in (10) is given by $r_h^{p',p} : \mathcal{V}_h^{p'} \times \mathcal{V}_h^p \times [\mathcal{W}_h]^d \rightarrow \mathbb{R}$

$$r_h^{p',p} : (\bar{\psi}_h, \bar{W}_h, \mathcal{G}_h) \mapsto \sum_{K \in \mathcal{E}_h} r_K^{p',p}(\bar{\psi}_h, \bar{W}_h, \mathcal{G}_h), \quad (11)$$

where the elemental DG form is given by $r_K^{p',p} : \mathcal{V}_h^{p'} \times \mathcal{V}_h^p \times [\mathcal{W}_h]^d \rightarrow \mathbb{R}$

$$\begin{aligned} r_K^{p',p} : (\bar{\psi}_h, \bar{W}_h, \mathcal{G}_h) \mapsto & \int_{\partial K} \bar{\psi}_h^+ \cdot \bar{\mathcal{H}}(\bar{W}_h^+, \bar{W}_h^-, N_h; \bar{\nabla} \mathcal{G}_h) dS \\ & - \int_K \bar{F}(\bar{W}_h; \bar{\nabla} \mathcal{G}_h) : \bar{\nabla} \bar{\psi}_h dV \\ & - \int_K \bar{\psi}_h \cdot \bar{S}(\bar{W}_h; \det(\bar{\nabla} \mathcal{G}_h)) dV. \end{aligned} \quad (12)$$

Next, we introduce a (nodal) basis for the test space ($\mathcal{V}_h^{p'}$), trial space (\mathcal{V}_h^p), and domain mapping space ($[\mathcal{W}_h]^d$) to reduce the weak formulation in residual form to a system of nonlinear algebraic equations in residual form. In the case where $p' = p$, we denote the algebraic residual

$$\mathbf{r} : \mathbb{R}^{N_u} \times \mathbb{R}^{N_x} \rightarrow \mathbb{R}^{N_u}, \quad \mathbf{r} : (\mathbf{u}, \mathbf{x}) \mapsto \mathbf{r}(\mathbf{u}, \mathbf{x}) \quad (13)$$

where $N_u = \dim \mathcal{V}_h^p$ and $N_x = \dim([\mathcal{W}_h]^d)$. In this notation, a standard DG discretization (algebraic form) reads: given $\mathbf{x} \in \mathbb{R}^{N_x}$, find $\mathbf{u} \in \mathbb{R}^{N_u}$ such that $\mathbf{r}(\mathbf{u}, \mathbf{x}) = \mathbf{0}$, where \mathbf{u} are the DG solution coefficients and \mathbf{x} are the coefficients of the domain mapping (nodal coordinates). Typically, \mathbf{x} is known (mesh generation) and fixed; however, in this work, it will be determined via optimization such that the mesh tracks (aligns element faces with) all discontinuities in the flow. Furthermore, we define the algebraic *enriched residual*

$$\mathbf{R} : \mathbb{R}^{N_u} \times \mathbb{R}^{N_x} \rightarrow \mathbb{R}^{N'_u}, \quad \mathbf{R} : (\mathbf{u}, \mathbf{x}) \mapsto \mathbf{R}(\mathbf{u}, \mathbf{x}) \quad (14)$$

associated with a trial space of degree p' , where $N'_u = \dim \mathcal{V}_h^{p'}$, which will be used to construct the implicit shock tracking objective function. In this work, we take $p' = p + 1$. Finally, to maintain a connection between the algebraic and functional representation of the DG solution, we define the operator $\Xi : \mathbb{R}^{N_u} \rightarrow \mathcal{V}_h^p$ that maps $\mathbf{v} \in \mathbb{R}^{N_u}$ to its representation as a function over the reference domain Ω_0 , $V_h = \Xi(\mathbf{v})$, i.e., \mathbf{v} is the encoding of $V_h \in \mathcal{V}_h^p$ as a vector in \mathbb{R}^{N_u} .

3. Construction of admissible domain mappings

In this section, we discretize the domain mapping on the computational mesh \mathcal{E}_h such that the mapped mesh approximates the boundaries of the physical domain to high-order, even as nodes are moved to track flow features (Section 3.1). Then, we construct a general, automated approach for the special case where all boundaries are planar and intersect to form non-smooth edges and corners (Section 3.2).

3.1. Domain mapping discretization and parametrization

Let $\{\hat{X}_I\}_{I=1}^{N_v}$ denote (ordered) nodes associated with the mesh \mathcal{E}_h (including high-order nodes). Then, any element of $[\mathcal{W}_h]^d$ is uniquely determined by its action on the nodes \hat{X}_I . That is, let $\{\Psi_I\}_{I=1}^{N_v}$ be a nodal basis of \mathcal{W}_h associated with the nodes $\{\hat{X}_I\}_{I=1}^{N_v}$, i.e., $\Psi_I(\hat{X}_J) = \delta_{IJ}$, and define

$$\mathcal{G}_h(\cdot; \mathbf{x}) : \Omega_0 \rightarrow \mathbb{R}^d, \quad \mathcal{G}_h(\cdot; \mathbf{x}) : X \mapsto \sum_{I=1}^{N_v} \hat{x}_I \Psi_I(X), \quad (15)$$

where the coefficients $\hat{x}_I \in \mathbb{R}^d$ can be interpreted as the physical coordinates of the reference nodes \hat{X}_I because they coincide with the action of the mapping at \hat{X}_I due to the choice of nodal basis and $\mathbf{x} \in \mathbb{R}^{N_{\mathbf{x}}}$ ($N_{\mathbf{x}} = dN_v$) is the concatenation of $\{\hat{x}_I\}_{I=1}^{N_v}$. To ensure that $\mathcal{G}_h(\cdot; \mathbf{x})$ is a bijection from Ω_0 to Ω , $\mathbf{x} \in \mathbb{R}^{N_{\mathbf{x}}}$ must be defined such that $\mathcal{G}_h(\mathcal{E}_h; \mathbf{x})$ is a valid mesh of Ω , i.e., a partition of Ω into non-overlapping and non-inverted elements. Because $\mathcal{G}_h(\cdot; \mathbf{x})$ is continuous for any $\mathbf{x} \in \mathbb{R}^{N_{\mathbf{x}}}$, the mesh $\mathcal{G}_h(\mathcal{E}_h; \mathbf{x})$ will inherit airtightness (no gaps between elements) from the reference mesh \mathcal{E}_h . Therefore, \mathbf{x} only needs to be restricted to ensure the elements of $\mathcal{G}_h(\mathcal{E}_h; \mathbf{x})$ are not inverted (for injectivity) and 2) conform to the boundary $\partial\Omega$ (for surjectivity with respect to Ω). The first condition is difficult to impose explicitly so it will be accounted for in the implicit tracking optimization problem, whereas the second condition will be explicitly baked into the definition of the admissible mappings. To this end, we will introduce a parametrization of the physical nodes

$$\phi : \mathbb{R}^{N_{\mathbf{y}}} \rightarrow \mathbb{R}^{N_{\mathbf{x}}}, \quad \phi : \mathbf{y} \mapsto \phi(\mathbf{y}) \quad (16)$$

such that $\mathcal{G}_h(\mathcal{E}_h; \phi(\mathbf{y}))$ conforms to $\partial\Omega$ for any $\mathbf{y} \in \mathbb{R}^{N_{\mathbf{y}}}$ that does not cause element inversion. References [11, 46, 48] introduced an approach to directly construct a boundary-preserving parametrization of the mesh motion from the analytical representation of each boundary; however, the approach is cumbersome when multiple boundaries intersect (e.g., at edges or corners). In the next section, we introduce a systematic procedure to define ϕ in the special case where all boundaries are planar; future work will extend the approach to curved boundaries.

Remark 2. For domains with curved boundaries, in particular boundaries that are non-polynomial functions or polynomials of degree greater than q , $\mathcal{G}_h(\mathcal{E}_h; \mathbf{x})$ will not partition Ω exactly because the boundaries will not be perfectly represented by functions in $[\mathcal{W}_h]^d$ (they will be approximated by polynomials of degree q).

3.2. Enforcement of planar physical boundaries

In the special case where all boundaries are planar, we define an affine parametrization of the physical nodes

$$\phi : \mathbf{y} \mapsto \mathbf{A}\mathbf{y} + \mathbf{b}, \quad (17)$$

where $\mathbf{A} \in \mathbb{R}^{N_{\mathbf{x}} \times N_{\mathbf{y}}}$ and $\mathbf{b} \in \mathbb{R}^{N_{\mathbf{x}}}$ are given analytically in terms of the surface normal vectors and the reference nodes. Because we take the reference and physical domains to be the same set (Remark 1), the reference-to-physical mapping can be interpreted as moving nodes throughout the domain. Suppose the boundary of $\partial\Omega$ is the union of N_b planar surfaces $\{\partial\Omega_i\}_{i=1}^{N_b}$, i.e., $\partial\Omega = \bigcup_{i=1}^{N_b} \partial\Omega_i$, that intersect to form non-smooth features, e.g., edges and corners. For each planar surface $\partial\Omega_i$, we denote its unit normal (oriented outward with respect to Ω) as $\eta_i \in \mathbb{R}^d$, which implies any two points $x, \bar{x} \in \partial\Omega_i$ must satisfy $\eta_i^T(x - \bar{x}) = 0$. We assume there are no redundancies in the specification of these N_b boundaries, i.e., the normal vectors of all boundaries passing through a given point are linearly independent. We will require \hat{x}_I to lie on all boundaries on which \hat{X}_I lies, i.e., \hat{x}_I can be obtained by sliding \hat{X}_I along the boundaries on which it lies. This condition is sufficient to ensure the mapped mesh $\mathcal{G}_h(\mathcal{E}_h; \mathbf{x})$ conforms to all boundaries $\{\partial\Omega_i\}_{i=1}^{N_b}$, provided none of the elements in $\mathcal{G}_h(\mathcal{E}_h; \mathbf{x})$ are inverted, because the same element faces/edges used to represent each boundary/intersection in the reference mesh \mathcal{E}_h will be used to represent the same boundary/intersection in the mapped mesh $\mathcal{G}_h(\mathcal{E}_h; \mathbf{x})$ (Figure 1).

Let $\mathcal{B}_I \subset \{1, \dots, N_b\}$ ($N_I^c := |\mathcal{B}_I|$) be the set of boundaries that pass through \hat{X}_I and $B_I \in \mathbb{R}^{N_I^c \times d}$ be the corresponding collection of boundary normals

$$\mathcal{B}_I = \{i \in \{1, \dots, N_b\} \mid \hat{X}_I \in \partial\Omega_i\}, \quad B_I = \begin{bmatrix} \eta_{(\mathcal{B}_I)_1} & \cdots & \eta_{(\mathcal{B}_I)_{N_I^c}} \end{bmatrix}^T. \quad (18)$$

We implicitly assume the set \mathcal{B}_I is ordered with $(\mathcal{B}_I)_i$ denoting its i th entry, although the specific ordering of the entries is unimportant, and define \mathcal{B}_I such that its entries are unique, i.e., $(\mathcal{B}_I)_i = (\mathcal{B}_I)_j$ implies $i = j$. Owing to the assumption that the normal vectors of all boundaries passing through a given point are linearly independent, we have $N_I^c \leq d$ and B_I is full rank. In order for the corresponding physical node \hat{x}_I to remain on all the boundaries in \mathcal{B}_I , it must satisfy

$$B_I(\hat{x}_I - \hat{X}_I) = 0 \quad (19)$$

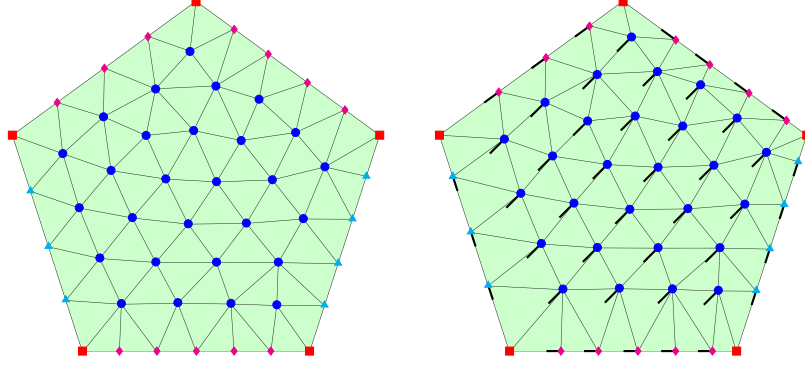


Figure 1: Reference domain Ω_0 (regular pentagon) and mesh \mathcal{E}_h with the reference nodes \hat{X}_I indicated with markers (*left*) and physical domain Ω and mapped mesh obtained by boundary-preserving mapping $\mathcal{G}_h(\cdot; \phi(\mathbf{y}))$ with the physical nodes \hat{x}_I indicated with markers (*right*); the node movement from its original position is indicated by (—). The nodes are partitioned into four categories based on the degree of freedom partitioning in (25)-(26): $\mathcal{I}_I^u = \{1, 2\}$ (\hat{x}_I moves freely) (●), $\mathcal{I}_I^u = \{1\}$ ($(\hat{x}_I)_1$ moves freely, $(\hat{x}_I)_2$ constrained) (♦), $\mathcal{I}_I^u = \{2\}$ ($(\hat{x}_I)_2$ moves freely, $(\hat{x}_I)_1$ constrained) (▲), $\mathcal{I}_I^u = \emptyset$ (\hat{x}_I fixed) (■).

which defines N_I^c unique constraints. We expand the coordinate of the physical node as

$$\hat{x}_I = Y_I \hat{x}_I^c + Z_I \hat{x}_I^u, \quad (20)$$

where $Y_I \in \mathbb{R}^{d \times N_I^c}$ is an orthogonal matrix such that $B_I Y_I$ is non-singular, $Z_I \in \mathbb{R}^{d \times (d - N_I^c)}$ is an orthogonal matrix such that $\text{Ran}(Y_I) \oplus \text{Ran}(Z_I) = \mathbb{R}^d$ ($\text{Ran}(A)$ denotes the range of the matrix A), and $\hat{x}_I^c \in \mathbb{R}^{N_I^c}$ and $\hat{x}_I^u \in \mathbb{R}^{d - N_I^c}$ are the coordinates of \hat{x}_I in the respective basis that will constitute the constrained and unconstrained degrees of freedom of \hat{x}_I , respectively. Substituting (20) into the constraints (19) leads to the following relationship between \hat{x}_I^c and \hat{x}_I^u that must hold for \hat{x}_I to remain on the same boundaries as \hat{X}_I

$$\hat{x}_I^c = [B_I Y_I]^{-1} B_I (\hat{X}_I - Z_I \hat{x}_I^u). \quad (21)$$

This leads to an affine relationship between the physical node coordinate and its unconstrained degrees of freedom

$$\hat{x}_I = A_I \hat{x}_I^u + b_I, \quad A_I := Z_I - Y_I [B_I Y_I]^{-1} B_I Z_I, \quad b_I := Y_I [B_I Y_I]^{-1} B_I \hat{X}_I, \quad (22)$$

which we concatenate over all nodes $I = 1, \dots, N_v$ to define the affine parametrization in (17) with

$$\mathbf{A} = \begin{bmatrix} A_1 & & \\ & \ddots & \\ & & A_{N_v} \end{bmatrix}, \quad \mathbf{y} = \begin{bmatrix} \hat{x}_1^u \\ \vdots \\ \hat{x}_{N_v}^u \end{bmatrix}, \quad \mathbf{b} = \begin{bmatrix} b_1 \\ \vdots \\ b_{N_v} \end{bmatrix} \quad (23)$$

and $N_{\mathbf{y}} = N_{\mathbf{x}} - \sum_{I=1}^{N_v} N_I^c$.

We choose Y_I and Z_I to be non-overlapping subsets of the columns of the $d \times d$ identity matrix

$$Y_I = \begin{bmatrix} e_{(\mathcal{I}_I^c)_1} & \cdots & e_{(\mathcal{I}_I^c)_{N_I^c}} \end{bmatrix}, \quad Z_I = \begin{bmatrix} e_{(\mathcal{I}_I^u)_1} & \cdots & e_{(\mathcal{I}_I^u)_{d - N_I^c}} \end{bmatrix}, \quad (24)$$

where $e_i \in \mathbb{R}^d$ is the i th canonical unit vector, $\mathcal{I}_I^u \subset \{1, \dots, d\}$ ($|\mathcal{I}_I^u| = d - N_I^c$) denotes the unconstrained degrees of freedom, and $\mathcal{I}_I^c = \{1, \dots, d\} \setminus \mathcal{I}_I^u$ denotes the constrained degrees of freedom; similar to \mathcal{B}_I , \mathcal{I}_I^u and \mathcal{I}_I^c are ordered sets with unique elements. This means \hat{x}_I^u and \hat{x}_I^c are subsets of the entries of \hat{x}_I

$$(\hat{x}_I^u)_i = (\hat{x}_I)_{(\mathcal{I}_I^u)_i}, \quad (\hat{x}_I^c)_j = (\hat{x}_I)_{(\mathcal{I}_I^c)_j} \quad (25)$$

for $i = 1, \dots, d - N_I^c$ and $j = 1, \dots, N_I^c$, i.e., \hat{x}_I^u are the components of \hat{x}_I allowed to move freely and \hat{x}_I^c are the components uniquely determined to ensure \hat{x}_I lies on the appropriate boundaries. The decomposition of $\{1, \dots, d\}$ into unconstrained and constrained degrees of freedom is not unique; the only condition is $B_I Y_I$

be non-singular because the $\text{Ran}(Y_I) \oplus \text{Ran}(Z_I) = \mathbb{R}^d$ condition is guaranteed by construction in (24). We choose the unconstrained degrees of freedom \hat{x}_I^u to correspond to the coordinate directions closest to the null space of B_I , denoted $\text{Null}(B_I)$, because this will require the least action on the constrained degrees of freedom. In the extreme case where $d - N_I^c$ coordinate directions lie in $\text{Null}(B_I)$, this choice implies the columns of Z_I will form a basis for $\text{Null}(B_I)$, which implies $B_I Z_I = 0$ and the expression for \hat{x}_I^c in (21) is independent of \hat{x}_I^u . To this end, let $V_I \in \mathbb{R}^{d \times (d - N_I^c)}$ be a matrix whose columns form an orthonormal basis for $\text{Null}(B_I)$, then the set \mathcal{I}_I^u is defined as

$$(\mathcal{I}_I^u)_i := \arg \min_{j \in \mathcal{I}_I^{(i)}} \|e_j - V_I V_I^T e_j\|, \quad \mathcal{I}_I^{(i)} = \{1, \dots, d\} \setminus \{(\mathcal{I}_I^u)_1, \dots, (\mathcal{I}_I^u)_{i-1}\} \quad (26)$$

for $i = 1, \dots, d - N_I^c$ and $\mathcal{I}_I^c = \{1, \dots, d\} \setminus \mathcal{I}_I^u$. The partitioning of the degrees of freedom of each node in a mesh of a regular pentagon using this procedure is illustrated in Figure 1.

Remark 3. *There are other many valid choices for Y_I and Z_I that effectively decompose \hat{x}_I into constrained and unconstrained parts. One choice that mimics approaches for enforcing linear equality constraints in optimization solvers [16] chooses the columns of Z_I to be an orthonormal basis for $\text{Null}(B_I)$ and Y_I to be an orthonormal basis for the range space of B_I^T . This guarantees that $B_I Y_I$ is non-singular and $B_I Z_I = 0$, which simplifies the expressions in (21) to $A_I = Z_I$ and $\hat{x}_I^c = [B_I Y_I]^{-1} B_I \hat{X}_I$ (independent of \hat{x}_I^u). While this approach is clean and elegant, the constrained and unconstrained parts of \hat{x}_I do not have an intuitive physical interpretation as components of \hat{x}_I .*

4. High-order implicit shock tracking formulation

The high-order implicit shock tracking method introduced in [45, 48] simultaneously computes the discrete solution of the conservation law and the nodal coordinates of the mesh that causes element faces to align with discontinuities. This is achieved through a fully discrete, full space PDE-constrained optimization formulation with the optimization variables taken to be the discrete flow solution and nodal coordinates of the mesh. With the boundary-preserving parametrization of the mesh motion in (16), the HOIST method is formulated as

$$(\mathbf{u}^*, \mathbf{y}^*) := \arg \min_{\mathbf{u} \in \mathbb{R}^{N_u}, \mathbf{y} \in \mathbb{R}^{N_y}} f(\mathbf{u}, \mathbf{y}) \quad \text{subject to: } \mathbf{r}(\mathbf{u}, \phi(\mathbf{y})) = \mathbf{0}, \quad (27)$$

where $f : \mathbb{R}^{N_u} \times \mathbb{R}^{N_y} \rightarrow \mathbb{R}$ is the objective function and the nodal coordinates of the aligned mesh are $\mathbf{x}^* = \phi(\mathbf{y}^*)$. The objective function is composed of two terms as

$$f : (\mathbf{u}, \mathbf{y}) \mapsto f_{\text{err}}(\mathbf{u}, \mathbf{y}) + \kappa^2 f_{\text{msh}}(\mathbf{y}), \quad (28)$$

which balances alignment of the mesh with non-smooth features and the quality of the elements and $\kappa \in \mathbb{R}_{\geq 0}$ is the mesh penalty parameter. The mesh alignment term, $f_{\text{err}} : \mathbb{R}^{N_u} \times \mathbb{R}^{N_y} \rightarrow \mathbb{R}$, is taken to be the norm of the enriched DG residual

$$f_{\text{err}} : (\mathbf{u}, \mathbf{y}) \mapsto \frac{1}{2} \|\mathbf{R}(\mathbf{u}, \phi(\mathbf{y}))\|_2^2. \quad (29)$$

To ensure elements of the discontinuity-aligned mesh are high-quality, we define the mesh distortion term, $f_{\text{msh}} : \mathbb{R}^{N_y} \rightarrow \mathbb{R}$, as

$$f_{\text{msh}} : \mathbf{y} \mapsto \frac{1}{2} \|\mathbf{R}_{\text{msh}}(\phi(\mathbf{y}))\|_2^2, \quad (30)$$

where $\mathbf{R}_{\text{msh}} : \mathbb{R}^{N_y} \rightarrow \mathbb{R}^{|\mathcal{E}_h|}$ is the element-wise mesh distortion with respect to an ideal element [48, 26, 36]. Concretely, assume the elements of \mathcal{E}_h are ordered and let $\Omega_{0,e} \in \mathcal{E}_h$ ($\Omega_{0,e} \subset \Omega_0$) for $e = 1, \dots, |\mathcal{E}_h|$ denote the e th element. Furthermore, define the corresponding physical element as $\Omega_e(\mathbf{x}) = \mathcal{G}_h(\Omega_{0,e}; \mathbf{x})$ for a given instance of the physical nodes $\mathbf{x} \in \mathbb{R}^{N_x}$ and let $K_{\star,e} \subset \mathbb{R}^d$ denote the ideal shape of element e . Then, the element-wise mesh distortion is defined as

$$[\mathbf{R}_{\text{msh}}(\mathbf{x})]_e = \frac{1}{|K_{\star,e}|} \int_{K_{\star,e}} \left(\frac{\|\nabla \mathcal{F}_{\star,e}(\cdot; \mathbf{x})\|_F^2}{d \det(\nabla \mathcal{F}_{\star,e}(\cdot; \mathbf{x}))_+^{2/d}} \right)^2 dV, \quad (31)$$

where $\mathcal{F}_{\star,e}(\cdot; \mathbf{x}) : K_{\star,e} \rightarrow \Omega_e(\mathbf{x})$ is a diffeomorphism between the ideal and physical element. We consider two choices for the ideal element ($K_{\star,e}$), which lead to a mesh distortion term with different properties: 1) $\Omega_{0,e}$ (the reference element) and 2) $K_{\star} \subset \mathbb{R}^d$ (the regular d -simplex). The first choice implies $\mathcal{F}_{\star,e}(\cdot; \mathbf{x}) = \mathcal{G}_h(\cdot; \mathbf{x})|_{\Omega_{0,e}}$ and the resulting mesh distortion—identical to the one used in our previous work [48]—penalizes deviation of the physical mesh from the reference mesh, whereas the second choice drives elements toward the regular d -simplex.

To obtain the first-order optimality system of the implicit shock tracking formulation in (27), we introduce the corresponding Lagrangian, $\mathcal{L} : \mathbb{R}^{N_u} \times \mathbb{R}^{N_y} \times \mathbb{R}^{N_u} \rightarrow \mathbb{R}$, defined as

$$\mathcal{L} : (\mathbf{u}, \mathbf{y}, \boldsymbol{\lambda}) \mapsto f(\mathbf{u}, \mathbf{y}) - \boldsymbol{\lambda}^T \mathbf{r}(\mathbf{u}, \phi(\mathbf{y})). \quad (32)$$

Then, the first-order optimality, or Karush-Kuhn-Tucker (KKT), conditions state that $(\mathbf{u}^*, \mathbf{y}^*) \in \mathbb{R}^{N_u} \times \mathbb{R}^{N_y}$ is a first-order solution of the optimization problem in (27) if there exists $\boldsymbol{\lambda}^* \in \mathbb{R}^{N_u}$ such that the Lagrangian is stationary, which leads to the following conditions

$$\begin{aligned} \frac{\partial f}{\partial \mathbf{u}}(\mathbf{u}^*, \mathbf{y}^*)^T - \frac{\partial \mathbf{r}}{\partial \mathbf{u}}(\mathbf{u}^*, \phi(\mathbf{y}^*))^T \boldsymbol{\lambda}^* &= \mathbf{0} \\ \frac{\partial f}{\partial \mathbf{y}}(\mathbf{u}^*, \mathbf{y}^*)^T - \frac{\partial \phi}{\partial \mathbf{y}}(\mathbf{y}^*)^T \frac{\partial \mathbf{r}}{\partial \mathbf{x}}(\mathbf{u}^*, \phi(\mathbf{y}^*))^T \boldsymbol{\lambda}^* &= \mathbf{0} \\ \mathbf{r}(\mathbf{u}^*, \phi(\mathbf{y}^*)) &= \mathbf{0}. \end{aligned} \quad (33)$$

Following [48], we define the Lagrange multiplier estimate, $\hat{\boldsymbol{\lambda}} : \mathbb{R}^{N_u} \times \mathbb{R}^{N_y} \rightarrow \mathbb{R}^{N_u}$, as

$$\hat{\boldsymbol{\lambda}} : (\mathbf{u}, \mathbf{y}) \mapsto \left[\frac{\partial \mathbf{r}}{\partial \mathbf{u}}(\mathbf{u}, \phi(\mathbf{y})) \right]^{-T} \frac{\partial f}{\partial \mathbf{u}}(\mathbf{u}, \mathbf{y})^T, \quad (34)$$

which ensures the first equation in (33) (adjoint equation) is satisfied for any $\mathbf{u} \in \mathbb{R}^{N_u}$ and $\mathbf{y} \in \mathbb{R}^{N_y}$. With this estimate of the Lagrange multipliers, the optimality conditions reduce to

$$\mathbf{c}(\mathbf{u}^*, \mathbf{y}^*) = \mathbf{0}, \quad \mathbf{r}(\mathbf{u}^*, \phi(\mathbf{y}^*)) = \mathbf{0}, \quad (35)$$

where $\mathbf{c} : \mathbb{R}^{N_u} \times \mathbb{R}^{N_y} \rightarrow \mathbb{R}^{N_u}$ is defined as

$$\mathbf{c} : (\mathbf{u}, \mathbf{y}) \mapsto \frac{\partial f}{\partial \mathbf{y}}(\mathbf{u}, \mathbf{y})^T - \frac{\partial \phi}{\partial \mathbf{y}}(\mathbf{y})^T \frac{\partial \mathbf{r}}{\partial \mathbf{x}}(\mathbf{u}, \phi(\mathbf{y}))^T \hat{\boldsymbol{\lambda}}(\mathbf{u}, \mathbf{y}). \quad (36)$$

Remark 4. *Intuitively, the enriched DG residual is an improved approximation of the infinite-dimensional weak formulation of the conservation law than the standard DG residual and, as a result, is sensitive to non-physical oscillations that result from approximating discontinuities on non-aligned meshes. Thus, minimizing this term promotes alignment of the mesh with discontinuities, as demonstrated in [48].*

Remark 5. *Because the DG equations (\mathbf{r}) with standard upwind numerical flux are enforced as constraints, the properties of the DG method are directly inherited by the HOIST method independent of the objective function. Therefore, there is flexibility in the choice of the numerical flux function for the enriched DG residual (\mathbf{R}). In this work, we use a central flux to define the enriched DG residual because it is smooth and conservative [48] and sufficient to reliably track shocks (Section 6).*

Remark 6. *The reference element is a reasonable choice for the ideal element if a high-quality reference mesh \mathcal{E}_h is used; however, the quality of the reference elements degrade as elements are collapsed during the tracking iterations ([48], Section 5.2.1)—particularly prevalent in problems with complex discontinuity surfaces—which has the adverse effect of the mesh distortion term favoring some poor-quality elements. On the other hand, taking the regular d -simplex to be the ideal element for all $e = 1, \dots, |\mathcal{E}_h|$ ensures high-quality elements are always favored by the mesh distortion term; however, it can also lead to substantial movement of the physical mesh away from the reference mesh even in regions away from the shock. In practice, we usually use the mesh distortion term based on the d -regular simplex ideal element, unless the large mesh motion causes many unwanted element collapses.*

Remark 7. In the case where the ideal element is the regular d -simplex, i.e., $K_{\star,e} = K_\star$ for $e = 1, \dots, |\mathcal{E}_h|$, the mapping $\mathcal{F}_{\star,e}$ is described in detail in [36]; we briefly outline its construction. Let $\{\psi_i\}_{i=1}^n$ be a nodal basis of $\mathcal{P}_q(K_\star)$ associated with well-spaced nodes $\{\hat{\xi}_i\}_{i=1}^n \subset K_\star$, where $n = \dim \mathcal{P}_q(K_\star) = \binom{q+d}{d}$. Then, $\mathcal{F}_{\star,e} : \xi \mapsto \sum_{i=1}^n \hat{x}_i^e \psi_i(\xi)$, where $\{\hat{x}_i^e\}_{i=1}^n \subset \{\hat{x}_I\}_{I=1}^{N_v}$ are the physical nodes associated with element e .

Remark 8. The objective function in (28)-(30) can be written as the norm of a residual function, $\mathbf{F} : \mathbb{R}^{N_u} \times \mathbb{R}^{N_y} \rightarrow \mathbb{R}^{N'_u + |\mathcal{E}_h|}$, as

$$f(\mathbf{u}, \mathbf{y}) = \frac{1}{2} \mathbf{F}(\mathbf{u}, \mathbf{y})^T \mathbf{F}(\mathbf{u}, \mathbf{y}), \quad \mathbf{F} : (\mathbf{u}, \mathbf{y}) \mapsto \begin{bmatrix} \mathbf{R}(\mathbf{u}, \phi(\mathbf{y})) \\ \kappa \mathbf{R}_{msh}(\phi(\mathbf{y})) \end{bmatrix}. \quad (37)$$

The implication is the HOIST optimization problem in (27) is a constrained residual minimization problem, which can be exploited in the development of the solver; see [48] and Section 5.1.2.

5. Robust implicit shock tracking solver

In this section, we introduce an iterative solver for the optimization problem in (27) based on the SQP method in [48] with improved robustness and capability. Because the DG system cannot be solved robustly on non-aligned meshes without additional measures to suppress numerical oscillations, nested approaches to solve the discrete PDE-constrained optimization problem in (27) are not appropriate; instead, we use a full-space approach that aims to simultaneously converge the DG solution and the mesh to their optimal values simultaneously. To this end, we define a new variable $\mathbf{z} \in \mathbb{R}^{N_z}$ ($N_z = N_u + N_y$) that combines the DG solution \mathbf{u} and unconstrained mesh coordinates \mathbf{y} as

$$\mathbf{z} = (\mathbf{u}, \mathbf{y}), \quad (38)$$

and use \mathbf{z} interchangeably with the tuple (\mathbf{u}, \mathbf{y}) . For brevity, we introduce the following notation for the derivatives of the objective function, $\mathbf{g} : \mathbb{R}^{N_z} \rightarrow \mathbb{R}^{N_z}$, and the DG residual, $\mathbf{J} : \mathbb{R}^{N_z} \rightarrow \mathbb{R}^{N_u} \times \mathbb{R}^{N_y}$, as

$$\mathbf{g} : \mathbf{z} \mapsto \begin{bmatrix} \frac{\partial f}{\partial \mathbf{u}}(\mathbf{u}, \mathbf{y})^T \\ \frac{\partial f}{\partial \mathbf{y}}(\mathbf{u}, \mathbf{y})^T \end{bmatrix}, \quad \mathbf{J} : \mathbf{z} \mapsto \begin{bmatrix} \frac{\partial \mathbf{r}}{\partial \mathbf{u}}(\mathbf{u}, \phi(\mathbf{y})) & \frac{\partial \mathbf{r}}{\partial \mathbf{x}}(\mathbf{u}, \phi(\mathbf{y})) \frac{\partial \phi}{\partial \mathbf{y}}(\mathbf{y}) \end{bmatrix}. \quad (39)$$

5.1. Sequential quadratic programming method

The SQP method in [48] produces a sequence of iterates $\{\mathbf{z}_k\}_{k=0}^\infty$ such that $\mathbf{z}_k = (\mathbf{u}_k, \mathbf{y}_k) \rightarrow \mathbf{z}^* = (\mathbf{u}^*, \mathbf{y}^*)$, where $(\mathbf{u}^*, \mathbf{y}^*)$ satisfies the first-order optimality conditions in (33). The sequence of iterates is generated as

$$\mathbf{z}_{k+1} = \mathbf{z}_k + \alpha_k \Delta \mathbf{z}_k, \quad (40)$$

where the search direction $\Delta \mathbf{z}_k \in \mathbb{R}^{N_z}$ is computed as the solution of the following quadratic program

$$\begin{aligned} & \underset{\Delta \mathbf{z} \in \mathbb{R}^{N_z}}{\text{minimize}} && \mathbf{g}_k^T \Delta \mathbf{z} + \frac{1}{2} \Delta \mathbf{z}^T \mathbf{B}_k \Delta \mathbf{z}, \\ & \text{subject to} && \mathbf{r}_k + \mathbf{J}_k \Delta \mathbf{z} = \mathbf{0} \end{aligned} \quad (41)$$

$\mathbf{g}_k \in \mathbb{R}^{N_z}$, $\mathbf{r}_k \in \mathbb{R}^{N_u}$, and $\mathbf{J}_k \in \mathbb{R}^{N_u \times N_z}$ are the objective gradient, residual, and residual Jacobian, respectively, evaluated at \mathbf{z}_k

$$\mathbf{r}_k := \mathbf{r}(\mathbf{u}_k, \phi(\mathbf{y}_k)), \quad \mathbf{g}_k := \mathbf{g}(\mathbf{z}_k), \quad \mathbf{J}_k := \mathbf{J}(\mathbf{z}_k), \quad (42)$$

$\mathbf{B}_k \in \mathbb{R}^{N_z \times N_z}$ is a symmetric positive definite (SPD) approximation to the Hessian of the Lagrangian at \mathbf{z}_k , and $\alpha_k \in \mathbb{R}_{>0}$ is the step length. The first-order optimality conditions of the quadratic program leads to the linear system of equations that must be solved at each iteration k

$$\begin{bmatrix} \mathbf{B}_k & \mathbf{J}_k^T \\ \mathbf{J}_k & \mathbf{0} \end{bmatrix} \begin{bmatrix} \Delta \mathbf{z}_k \\ \boldsymbol{\eta}_k \end{bmatrix} = - \begin{bmatrix} \mathbf{g}_k \\ \mathbf{r}_k \end{bmatrix}, \quad (43)$$

where $\boldsymbol{\eta}_k \in \mathbb{R}^{N_u}$ are the Lagrange multipliers associated with the linearized constraint in (41).

5.1.1. Line search globalization

To ensure the sequence converges to a first-order critical point of (27) from any initial guess, the step length, α_k , is computed to guarantee sufficient decrease of a merit function, $\varphi_k : \mathbb{R} \rightarrow \mathbb{R}$, that combines the objective function and constraint violation. In this work, α_k is computed using backtracking [32] such that

$$\varphi_k(\alpha_k) \leq \varphi_k(0) + c\alpha_k\varphi'_k(0), \quad (44)$$

where $c \in (0, 1)$. We use the ℓ_1 merit function, defined as

$$\varphi_k : \alpha \mapsto f(\mathbf{z} + \alpha\Delta\mathbf{z}_k) + \mu_k \|\mathbf{r}(\mathbf{z}_k + \alpha\Delta\mathbf{z}_k)\|_1; \quad (45)$$

with the penalty parameter, $\mu_k \in \mathbb{R}_{>0}$, taken as [32]

$$\mu_0 = 0, \quad \mu_k = \min\{\max\{\varpi\bar{\mu}_k, \mu_{k-1}\}, \mu_{\max}\}, \quad \bar{\mu}_k = \frac{\mathbf{g}_k^T \Delta\mathbf{z}_k + (1/2)\Delta\mathbf{z}_k^T \mathbf{B}_k \Delta\mathbf{z}_k}{(1 - \rho) \|\mathbf{r}_k\|_1}, \quad (46)$$

where $\varpi > 1$ and $\rho \in (0, 1)$ are parameters taken to be $\varpi = 1.2$ and $\rho = 0.95$ in this work.

Remark 9. The choice of penalty parameter in (46) for the ℓ_1 merit function differs from the choice in [48] that defines

$$\mu_k = 2 \|\hat{\boldsymbol{\lambda}}(\mathbf{z}_k)\|_\infty \quad (47)$$

because this guarantees, under some assumptions, the SQP search direction will be a direction of descent for the ℓ_1 merit function [32]. However, we observed this choice can lead to a scaling mismatch between the objective and constraint causing many unnecessary line search iterations and interfering with progress of the iteration, which is consistent with other observations [32].

5.1.2. Levenberg-Marquardt Hessian approximation

We use the modified Levenberg-Marquardt Hessian approximation introduced in [10, 48] to define \mathbf{B}_k . To this end, we expand \mathbf{B}_k as

$$\mathbf{B}_k = \begin{bmatrix} \mathbf{B}_k^{uu} & \mathbf{B}_k^{uy} \\ (\mathbf{B}_k^{uy})^T & \mathbf{B}_k^{yy} \end{bmatrix}, \quad (48)$$

where the individual components $\mathbf{B}_k^{uu} \in \mathbb{R}^{N_u \times N_u}$, $\mathbf{B}_k^{uy} \in \mathbb{R}^{N_u \times N_y}$, and $\mathbf{B}_k^{yy} \in \mathbb{R}^{N_y \times N_y}$ are defined as

$$\begin{aligned} \mathbf{B}_k^{uu} &:= \frac{\partial \mathbf{F}}{\partial \mathbf{u}}(\mathbf{z}_k)^T \frac{\partial \mathbf{F}}{\partial \mathbf{u}}(\mathbf{z}_k) \\ \mathbf{B}_k^{uy} &:= \frac{\partial \mathbf{F}}{\partial \mathbf{u}}(\mathbf{z}_k)^T \frac{\partial \mathbf{F}}{\partial \mathbf{y}}(\mathbf{z}_k) \\ \mathbf{B}_k^{yy} &:= \frac{\partial \mathbf{F}}{\partial \mathbf{y}}(\mathbf{z}_k)^T \frac{\partial \mathbf{F}}{\partial \mathbf{y}}(\mathbf{z}_k) + \gamma_k \frac{\partial \phi}{\partial \mathbf{y}}(\mathbf{y}_k)^T \mathbf{D}_k \frac{\partial \phi}{\partial \mathbf{y}}(\mathbf{y}_k) \end{aligned} \quad (49)$$

and $\mathbf{D}_k \in \mathbb{R}^{N_\pi \times N_\pi}$ is a SPD matrix constructed to regularize the mesh motion and $\gamma_k \in \mathbb{R}_{\geq 0}$ is a regularization parameter. The regularization matrix, \mathbf{D}_k , is taken to be the linear elasticity (isotropic) stiffness matrix with elasticity modulus inversely proportional to the volume of the elements in the reference mesh [48]. The regularization parameter, γ_k , is difficult to choose *a priori* because the performance of the solver is sensitive to its value: small values can lead to an ill-conditioned Hessian approximation that results in poor-quality search directions and large mesh motion, whereas large values over-regularize the Hessian approximation, which can lead to small steps with little information from the actual Hessian. Following [10, 48], we reduce the sensitivity of the SQP method to the choice of the regularization parameter by choosing it adaptively such that the magnitude of the mesh motion lies in a reasonable range. That is, if the magnitude of $\Delta\mathbf{x}_k := \phi(\mathbf{y}_k) - \phi(\mathbf{y}_{k-1})$ is too large (small), we increase (decrease) the regularization parameter for the

next iteration as

$$\gamma_{k+1} = \max\{\bar{\gamma}_{k+1}, \gamma_{\min}\}, \quad \bar{\gamma}_{k+1} = \begin{cases} \tau^{-1}\gamma_k & \text{if } \|\Delta \mathbf{x}_k\| < \sigma_1 L \\ \tau\gamma_k & \text{if } \|\Delta \mathbf{x}_k\| > \sigma_2 L \\ \gamma_k & \text{otherwise,} \end{cases} \quad (50)$$

where $L \in \mathbb{R}_{>0}$ is a reference length for the domain, $\tau \in \mathbb{R}_{>0}$ is a parameter that controls the aggressiveness of the adaptation, $\sigma_1, \sigma_2 \in \mathbb{R}_{>0}$ are parameters that define acceptable magnitudes of the mesh motion relative to the reference length scale, $\gamma_{\min} \in \mathbb{R}_{>0}$ is a minimum value for the regularization parameter, and $\gamma_0 \in \mathbb{R}_{\geq 0}$ is the starting value for the regularization parameter. In this work, we typically choose $\tau \in (1, 2]$, $\sigma_1 = 10^{-2}$, $\sigma_2 = 10^{-1}$, γ_{\min} and γ_0 are problem-specific, and L is determined from the extents of the domain.

Remark 10. *The choice of Hessian approximation in (48)-(49) is identical to that introduced in [48] with the sole exception being the definition of the regularization matrix, \mathbf{D}_k , that was previously defined as the stiffness matrix of independent Poisson equations for each coordinate direction. Both choices lead to similar performance; however, isotropic linear elasticity is a more natural and intuitive choice because it leads to the interpretation of the mesh as a pseudo-structure, which is common in settings that involve mesh motion, e.g., fluid-structure interaction [28].*

5.1.3. Mesh quality parameter adaptation

In addition to the choice of Hessian approximation (Section 5.1.2), the mesh quality parameter (κ) in (28) plays a critical role in obtaining high-quality search directions; however, for complex problems, selecting a single value of κ *a priori* as in [48] does not work well in practice. If κ is taken too small, it can lead to search directions that severely degrade the quality of the mesh, whereas excessively large values of κ will prioritize mesh quality over alignment with discontinuities, potentially resulting in convergence to a non-aligned mesh. This is complicated by the fact that the meaning of “small” and “large” values of κ changes throughout the optimization process as $f_{\text{err}}(\mathbf{z}_k)$ and $f_{\text{msh}}(\mathbf{y}_k)$ change relative to each other. We circumvent this issue by adapting the value of κ during the optimization procedure, i.e., at iteration k of the optimization procedure, κ in the definition of the objective function (28) is replaced with κ_k , where $\{\kappa_k\}_{k=0}^{\infty}$ is a sequence of mesh quality parameters. Because modifying the penalty parameter changes the definition of the objective function, we aim to adapt it infrequently, i.e., $\kappa_k = \kappa_{k-1}$ for many iterations, and for only a finite number of iterations, i.e., $\kappa_k = \bar{\kappa}$ for $k > M$, where $M > 0$ is a constant. The latter condition ensures the definition of the objective function is fixed in the asymptotic regime to not hinder or stall convergence.

Our adaptation procedure aims to keep the contributions from f_{err} and $\kappa^2 f_{\text{msh}}$ to the objective function relatively balanced with f_{err} slightly dominate to ensure tracking discontinuities is prioritized. To this end, we take

$$\kappa_k = \max\{v_k \kappa_{k-1}, \kappa_{\min}\}, \quad v_k = \begin{cases} v & \text{if } f_{\text{err}}(\mathbf{z}_k) < \xi \kappa_{k-1}^2 f_{\text{msh}}(\mathbf{y}_k) \text{ and } k \leq M \\ 1 & \text{otherwise,} \end{cases} \quad (51)$$

where $\xi \in \mathbb{R}_{>0}$ is a constant that defines the target ratio between f_{err} and $\kappa^2 f_{\text{msh}}$, $v \in (0, 1)$ is the rate at which κ decreases, $\kappa_{\min} \in \mathbb{R}_{\geq 0}$ is a lower bound on the mesh quality parameter, and κ_0 is the starting point for the mesh quality parameter, usually chosen as $\kappa_0 = \sqrt{f_{\text{err}}(\mathbf{z}_0)/f_{\text{msh}}(\mathbf{y}_0)}$.

Remark 11. *Based on the updated formula in (51), the value of κ is only modified periodically. To see this, let $k' \ll M$ be the last iteration in which the value of κ was modified, which implies*

$$f_{\text{err}}(\mathbf{z}_{k'}) < \xi \kappa_{k'-1}^2 f_{\text{msh}}(\mathbf{y}_{k'}), \quad (52)$$

and suppose $v\kappa_{k'-1} > \kappa_{\min}$, then $\kappa_{k'} = v\kappa_{k'-1}$. Furthermore, we assume

$$f_{\text{err}}(\mathbf{z}_{k'}) \geq \xi (v\kappa_{k'-1})^2 f_{\text{msh}}(\mathbf{y}_{k'}); \quad (53)$$

although this is not explicitly enforced algorithmically, it will eventually hold because κ_k will decrease geometrically if $f_{\text{err}}(\mathbf{z}_k)$ is dominated by $\kappa_k^2 f_{\text{msh}}(\mathbf{y}_k)$ due to the adaptation criteria in (51). Let $k'' > k'$ be the next iteration in which the value of κ is updated, i.e., the smallest value such that

$$f_{\text{err}}(\mathbf{z}_{k''}) < \xi \kappa_{k''-1}^2 f_{\text{msh}}(\mathbf{y}_{k''}) = \xi (v\kappa_{k'-1})^2 f_{\text{msh}}(\mathbf{y}_{k''}), \quad (54)$$

where we used $\kappa_k = \kappa_{k'} = v\kappa_{k'-1}$ for $k = k', \dots, k'' - 1$ (definition of k''). In the early iterations of the optimization procedure (k' small), the values of $f_{\text{err}}(\mathbf{z}_k)$ and $f_{\text{msh}}(\mathbf{y}_k)$ will change significantly between iterations, which may cause frequent updates depending on the choice of ξ and v . However, in later iterations (k' large), the values of $f_{\text{err}}(\mathbf{z}_k)$ and $f_{\text{msh}}(\mathbf{u}_k)$ stabilize close to their optimal values. If $f_{\text{err}}(\mathbf{z}_k) \approx f_{\text{err}}(\mathbf{z}_{k'})$ and $f_{\text{msh}}(\mathbf{y}_k) \approx f_{\text{msh}}(\mathbf{y}_{k'})$ for $k > k'$, there may not exist a value of k'' such that (54) is satisfied in light of (53), which means the final update to κ occurs at iteration k' . Because of this, in practice, the mesh penalty updates cease naturally and it is not necessary to terminate them after M iterations. In practice, we initially observe numerous successive iterations where updates occur to calibrate the value of κ_k until both (52) and (53) hold, after which updates occur only periodically.

Remark 12. Adapting penalty parameters is a common practice in numerical (constrained) optimization. For example, penalty, augmented Lagrangian, and interior point methods construct unconstrained subproblems whose objective function is the original objective penalized by the constraint violation weighted by a penalty parameter [16, 32]. The penalty parameter is fixed while an approximate local minima to the unconstrained problem is sought and then adapted. The approach in (51) uses the structure of the objective function to update the penalty parameter rather than stationarity of the subproblems.

5.1.4. Incorporation of robustness measures

The SQP solver outlined to this point is identical to the one introduced in [48], barring a few exceptions (Remarks 9-10, Section 5.1.3). Numerical experimentation with this baseline SQP solver revealed it is not sufficiently robust to handle more complex problems than those explored in [48], particularly high Mach flows and flows with complex discontinuity (shock and contacts) surfaces. In this work, we propose a number of modifications to the SQP step with the intention of improving its overall robustness for complex flows. To this end, the iteration update in (40) will be changed to

$$\tilde{\mathbf{z}}_{k+1} = \mathbf{z}_k + \alpha_k \Delta \mathbf{z}_k, \quad \mathbf{z}_{k+1} = \Upsilon_{k+1}(\tilde{\mathbf{z}}_{k+1}), \quad (55)$$

where $\tilde{\mathbf{z}}_{k+1}$ is the step that comes directly from SQP, which is then modified using the mapping $\Upsilon_k : \mathbb{R}^{N_z} \rightarrow \mathbb{R}^{N_z}$ to incorporate robustness measures (Section 5.2). To ensure this perturbation of the SQP step does not hinder or stall convergence, we require $\Upsilon_k = \text{Id}$ for $k > M$, where $M > 0$ is a constant. This ensures the modified update in (55) reduces to the standard SQP update in (40) after M iterations. The remainder of this section provides an algorithmic construction of Υ_k that incorporates critical measures to ensure the modified SQP method can robustly converge, even for complex flows.

5.2. Modifications to SQP step for improved robustness

We introduce three robustness measures that collectively define the mapping Υ_k that are critical for the SQP solver in the previous section to reliably converge for complex flows: 1) boundary-preserving, shock-aware element removal, 2) removal of geometric curvature from inverted or ill-conditioned elements, and 3) element-wise solution re-initialization.

5.2.1. Element removal via edge collapse

For flows with complex shock surfaces, e.g., reflecting and interacting shocks (e.g., Figures 31-33), it is not reasonable to expect smooth deformations to a shock-agnostic mesh (fixed mesh topology) to cause element faces to track all discontinuity surfaces. This intuition was confirmed by numerical experiments that showed, despite measures to keep the mesh well-conditioned, minimization of the enriched residual causes elements to be crushed near discontinuity surfaces. Rather than attempting to prevent this behavior, e.g., by increasing the mesh quality and regularization parameters, the best option is to simply remove the crushed elements. To accomplish this, we remove appropriate elements by collapsing their shortest edge, an operation that is well-defined for simplicial meshes of any polynomial degree in any dimension. As such, in this work, we only consider simplex meshes. Edge collapses are the only topological mesh operation required for the proposed implicit shock tracking method; more complex operations such as edge flips, face swaps, refinement, and complete re-meshing are not required, all of which become more complicated as the polynomial degree and dimension of the mesh increase. This is a substantial distinction of the proposed approach from explicit shock tracking approaches [31, 37] that require sophisticated mesh operations, which limits their utility in

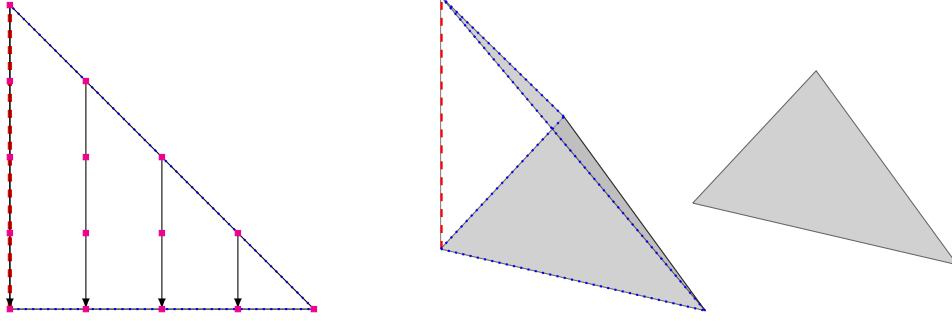


Figure 2: Mechanics of edge collapse for two-dimensional (*left*) and three-dimensional (*middle*) simplex, including the collapsing edge (---), edges/faces that will align after the collapse (..... and gray shaded), and the high-order nodes of the element (•). In the three-dimensional case, the nodes are excluded for clarity and the remaining zero-volume element is included (*right*).

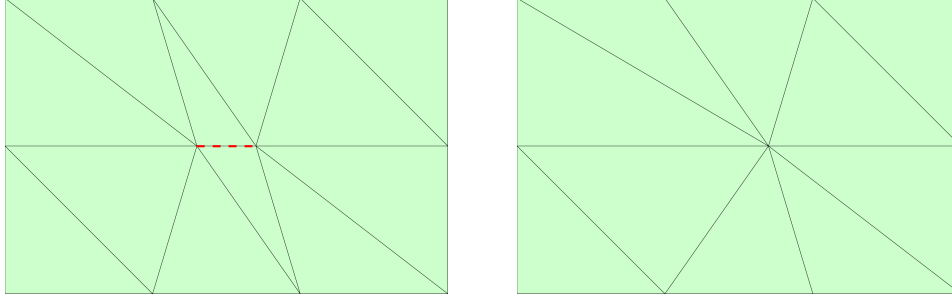


Figure 3: Mesh prior to (*left*) and after (*right*) collapse of the highlighted edge (---) and removal of zero-volume elements.

three dimensions, particularly for complex shock structures. While the concept of element removal via edge collapse is not new in the context of implicit shock tracking [10, 48], we provide implementation details and identify two important considerations, namely, preservation of boundaries and shocks.

Mechanics of simplex collapse. From the definition of a simplex, collapsing any of its edges causes the volume of the element to go to zero; this is not true for other element geometries and the fundamental reason why element removal via edge collapse is simple and straightforward for simplex element, but not necessarily other geometries. Furthermore, the edge collapse causes the surface area of $d - 1$ faces of the simplex (those containing the collapsed edge) to go to zero and the other 2 faces (those the collapsed edge connects) to overlap (Figure 2). In the context of a mesh comprised of (potentially high-order) simplex elements, collapsing an edge causes the volume of all elements containing that edge to go to zero and the faces connected by that edge to overlap; the latter condition ensures there are no gaps in the mesh. Subsequently, these zero-volume elements are removed and the connectivity is adjusted using the information in the newly overlapped faces (Figure 3).

Identification of elements for removal. With the mechanics of simplicial edge collapses established above, it remains to decide which edges to collapse in the mesh. Because the need to collapse elements arises from the desire to remove poor-quality elements that emerge during the implicit shock tracking iterations, we begin by identifying problematic elements and remove each one by collapsing its shortest edge. In this work, problematic elements are elements with a small volume (either in the reference or physical mesh), with a short minimum edge length, or that are inverted or nearly inverted. To this end, define $v_{0,e} \in \mathbb{R}_{\geq 0}$ and $v_e : \mathbb{R}^{N_{\mathbf{x}}} \rightarrow \mathbb{R}_{\geq 0}$ as the volume of the e th element of the reference and physical domain, respectively, i.e.,

$$v_{0,e} := \int_{\Omega_{0,e}} dV, \quad v_e : \mathbf{x} \mapsto \int_{\mathcal{G}_h(\Omega_{0,e}; \mathbf{x})} dv. \quad (56)$$

Furthermore, define $\ell_{e,j} : \mathbb{R}^{N_{\mathbf{x}}} \rightarrow \mathbb{R}_{\geq 0}$, where $\ell_{e,j} : \mathbf{x} \mapsto \ell_{e,j}(\mathbf{x})$ denotes the distance between the endpoints of the j th edge of the e th physical element, $\mathcal{G}_h(\Omega_{0,e}; \mathbf{x})$; this will be the notion of “edge length” used in this work rather than the true arc length of the edge (Remark 13). We define the minimum and maximum edge

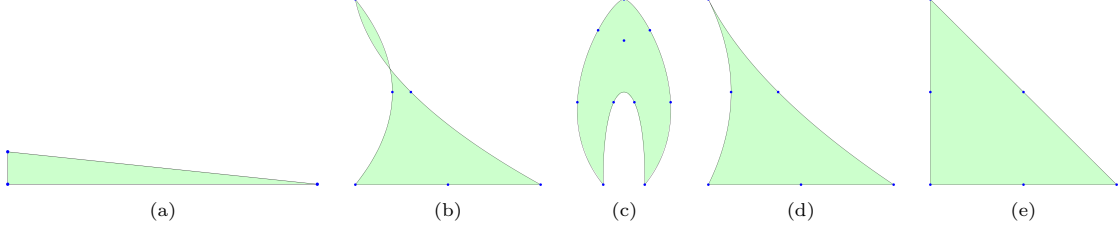


Figure 4: Illustration of problematic two-dimensional simplex elements. (a) An element with a small volume and short edge. (b) An inverted element ($g_{e,\text{inf}} < 0$). (c) A skewed element with a large volume, edges of similar lengths, and the bottom edge with a short distance between its endpoints, which justifies use of distance between edge endpoints rather than edge length in the definition of $\mathcal{E}_{\text{rmv},3}$. (d) An ill-conditioned element with $g_{e,\text{inf}} < (1/60)g_{e,\text{sup}}$. (e) The well-conditioned element that results from straightening the ill-conditioned element in (d).

lengths of the e th element, $\ell_{e,\text{min}} : \mathbb{R}^{N_{\mathbf{x}}} \rightarrow \mathbb{R}_{\geq 0}$ and $\ell_{e,\text{max}} : \mathbb{R}^{N_{\mathbf{x}}} \rightarrow \mathbb{R}_{\geq 0}$, respectively, as

$$\ell_{e,\text{min}} : \mathbf{x} \mapsto \min_{j \in \{1, \dots, N_{\text{ed}}\}} \ell_{e,j}(\mathbf{x}), \quad \ell_{e,\text{max}} : \mathbf{x} \mapsto \max_{j \in \{1, \dots, N_{\text{ed}}\}} \ell_{e,j}(\mathbf{x}), \quad (57)$$

where $N_{\text{ed}} = d(d+1)/2$ is the number of edges in a simplex. Finally, we define the smallest and largest values of the domain mapping Jacobian of the e th element, $g_{e,\text{inf}} : \mathbb{R}^{N_{\mathbf{x}}} \rightarrow \mathbb{R}$ and $g_{e,\text{sup}} : \mathbb{R}^{N_{\mathbf{x}}} \rightarrow \mathbb{R}$, respectively, as

$$g_{e,\text{inf}} : \mathbf{x} \mapsto \inf_{X \in \Omega_{0,e}} \det(\bar{\nabla} \mathcal{G}_h(X; \mathbf{x})), \quad g_{e,\text{sup}} : \mathbf{x} \mapsto \sup_{X \in \Omega_{0,e}} \det(\bar{\nabla} \mathcal{G}_h(X; \mathbf{x})). \quad (58)$$

With these definitions, we define the collection of problematic elements as the set-valued function, $\mathcal{E}_{\text{rmv}} : \mathbb{R}^{N_{\mathbf{x}}} \rightarrow \mathcal{S}_h$, defined as

$$\mathcal{E}_{\text{rmv}} : \mathbf{x} \mapsto \mathcal{E}_{\text{rmv},1}(\mathbf{x}) \cup \mathcal{E}_{\text{rmv},2}(\mathbf{x}) \cup \mathcal{E}_{\text{rmv},3}(\mathbf{x}) \cup \mathcal{E}_{\text{rmv},4}(\mathbf{x}), \quad (59)$$

where \mathcal{S}_h is the collection of all subsets of \mathcal{E}_h and the set-valued functions $\mathcal{E}_{\text{rmv},1} : \mathbb{R}^{N_{\mathbf{x}}} \rightarrow \mathcal{S}_h$, $\mathcal{E}_{\text{rmv},2} : \mathbb{R}^{N_{\mathbf{x}}} \rightarrow \mathcal{S}_h$, $\mathcal{E}_{\text{rmv},3} : \mathbb{R}^{N_{\mathbf{x}}} \rightarrow \mathcal{S}_h$, $\mathcal{E}_{\text{rmv},4} : \mathbb{R}^{N_{\mathbf{x}}} \rightarrow \mathcal{S}_h$ are

$$\begin{aligned} \mathcal{E}_{\text{rmv},1} : \mathbf{x} &\mapsto \{\Omega_{0,e} \in \mathcal{E}_h \mid v_e(\mathbf{x}) \leq c_1 v_{0,e}\} \\ \mathcal{E}_{\text{rmv},2} : \mathbf{x} &\mapsto \{\Omega_{0,e} \in \mathcal{E}_h \mid \min\{v_{0,e}, v_e(\mathbf{x})\} \leq c_2\} \\ \mathcal{E}_{\text{rmv},3} : \mathbf{x} &\mapsto \{\Omega_{0,e} \in \mathcal{E}_h \mid \ell_{e,\text{min}}(\mathbf{x}) \leq c_3 \ell_{e,\text{max}}(\mathbf{x})\} \\ \mathcal{E}_{\text{rmv},4} : \mathbf{x} &\mapsto \{\Omega_{0,e} \in \mathcal{E}_h \mid g_{e,\text{inf}}(\mathbf{x}) \leq c_4 g_{e,\text{sup}}(\mathbf{x})\}, \end{aligned} \quad (60)$$

and $c_1, c_2, c_3, c_4 \in \mathbb{R}_{\geq 0}$ are tolerances. That is, we identify elements for removal if its: 1) physical volume is small relative to that of the corresponding reference element ($\mathcal{E}_{\text{rmv},1}$), 2) absolute volume in either the reference or physical domain is small ($\mathcal{E}_{\text{rmv},2}$), 3) shortest edge is small relative to its longest edge in the physical domain ($\mathcal{E}_{\text{rmv},3}$), or 4) mapping is nearly inverted in a relative sense ($\mathcal{E}_{\text{rmv},4}$). In this work, we usually take $c_1 = 0.2$, $c_2 = 10^{-10}$, $c_3 = 0.2$, $c_4 = 0$, with a few exceptions (Section 6). Commonly occurring problematic elements are illustrated in Figure 4.

Boundary-preserving and shock-aware edge collapse. With the elements identified for removal, we remove them one-by-one by collapsing their shortest edge (edge with smallest distance between endpoints) and updating the connectivity of the resulting mesh as discussed previously. For the edge collapse to be well-defined, the position of the degenerate edge (point) must be defined; the two endpoints of the original edge are natural choices, although any point in the vicinity of the original edge are candidates. In this work, we position the collapsed edge at one of the endpoints of the original edge with constraints on which endpoint is chosen to ensure boundaries are preserved (to high-order) and tracked shocks are maintained to the extent possible. The first condition (boundary preservation) is a strict requirement to ensure the PDE domain does not change, whereas the second condition (shock preservation) enhances the robustness of the SQP solver. To preserve the domain boundary (to high-order), we collapse the edge at whichever of the original endpoints lies at the intersection of more boundaries (constraints). This ensures remaining mesh nodes will not move off boundaries due to an edge collapse, rather they will slide along boundaries (Figure 5). In the common

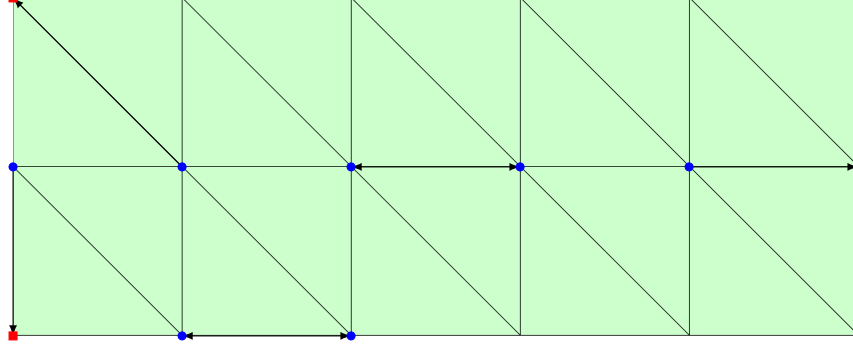


Figure 5: Demonstration of movable (●) and fixed (■) endpoints for potential edge collapses throughout a mesh. A point must be fixed if it lies at the intersection of more boundaries than the opposite endpoint of the edge.

case where both endpoints lie at the intersection of the same boundaries, the position of the degenerate edge will be determined from the value of the DG solution $\Xi(\tilde{\mathbf{u}}_{k+1})$ to maintain the tracked shock. Because the DG solution is multi-valued at edge endpoints, we degenerate the edge at the endpoint at which the range of values in $\Xi(\tilde{\mathbf{u}}_{k+1})$ is largest. Because endpoints that lie on shocks will possess a large range of values (equal to the magnitude of the jump in the discontinuity), this effectively ensures nodes will not be moved off a shock surface. The opposite choice could degrade the representation of the shock, which could either destroy or significantly slow convergence (Figure 6).

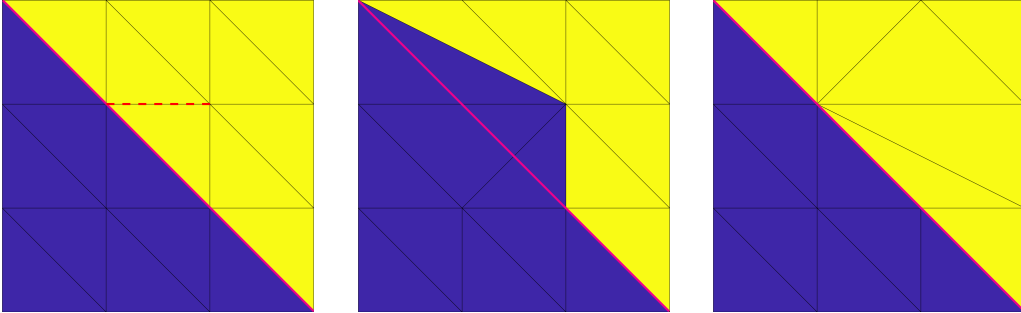


Figure 6: A shock-aligned mesh (true shock given by —) and corresponding solution (left) and two meshes that result from degenerating the highlighted edge (---) at its right endpoint (middle) and its left endpoint (right). Because the jump in the solution at the left endpoint is larger, we choose to degenerate the edge at that point; as a result, the shock is preserved.

Element removal and solution transfer. Because the reference and physical meshes share the same connectivity, edge collapses and subsequent element removal are applied to the reference mesh and inherited by the physical mesh. Once all problematic elements are removed, the DG solution is trivially transferred to the new mesh by removing degrees of freedom corresponding to removed elements. In the context of the SQP iterations, $\tilde{\mathbf{z}}_{k+1} = (\tilde{\mathbf{u}}_{k+1}, \tilde{\mathbf{y}}_{k+1})$ denotes the SQP update at iteration k in (55). Then, the problematic elements $\mathcal{E}_{\text{rmv}}(\phi(\tilde{\mathbf{y}}_{k+1}))$ are removed via edge collapses to produce a new mesh, the parametrization in (16) is reconstructed for the new mesh and the unconstrained degrees of freedom are extracted, and the DG solution is transferred to the new mesh to produce the state $\tilde{\mathbf{z}}_{k+1} = (\tilde{\mathbf{u}}_{k+1}, \tilde{\mathbf{y}}_{k+1})$.

Remark 13. We use the distance between endpoints rather than edge length to avoid favoring edges that have an artificially large length despite its end nodes being close together (Figure 4c); in our experience, these edges are advantageous to collapse because they are indicative of low-quality elements and degenerating it at either of its endpoints induces a relatively small motion to the remaining nodes.

Remark 14. Even though the reference element volume is independent of the physical nodes of the mesh (\mathbf{x}), they will change every time an element is collapsed. We have observed some pathological cases where an element can be small in the reference mesh but not in the physical mesh, leading to an ill-conditioned SQP

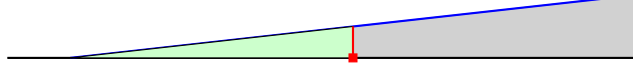


Figure 7: A situation that arises when a shock (—) makes an acute angle with a boundary (—). If the indicated element is targeted for removal, its shortest edge (—) will be collapsed, which makes it impossible to preserve both the shock and boundary. Because preservation of the boundary is a hard constraint, the edge is degenerated at its bottom endpoint (■).

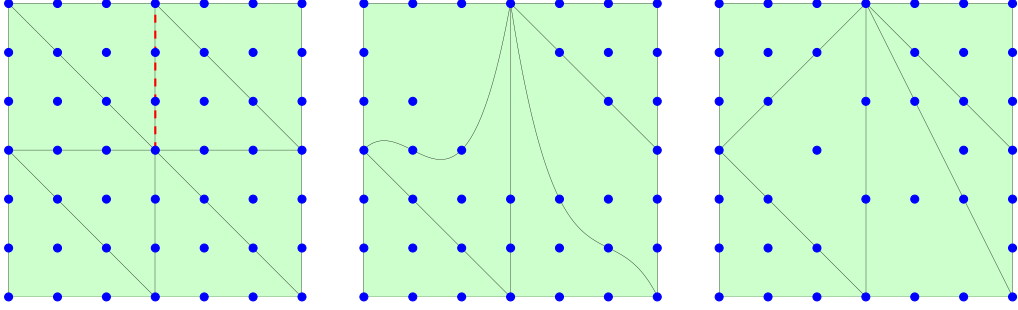


Figure 8: An edge collapse (---) in the reference mesh (left) can lead to highly distorted, artificially curved elements if only the nodes (●) along the collapsed edge are moved (middle). To avoid this situation, we reset all elements whose nodes were affected by the edge collapse to be straight-sided (right).

system (43). A robust algorithm must remove them or use another strategy to prevent them from arising; we opt for the former case by including an absolute tolerance on the reference element volume as a condition for element removal ($\mathcal{E}_{\text{rmv},2}$).

Remark 15. Because domain preservation is prioritized over shock preservation, some pathological cases where the position of the degenerate edge cannot be chosen to maintain the shock, e.g., shocks that form sharp edges with boundaries (Figure 7). In these cases, additional SQP iterations are needed to fix the shock position. Such situations are less likely to occur if the mesh is finer in these regions or the element removal parameters, particularly c_3 , are weakened.

Remark 16. In the situation where the shortest edge of an element identified for removal cannot be collapsed without changing the domain boundary, e.g., its endpoints lie on different boundaries, we collapse the shortest admissible edge (i.e., edges whose collapse will preserve the domain boundary) and use the same logic to identify the endpoint at which to degenerate the edge to preserve the boundary and shock.

Remark 17. In the physical domain, the edge collapse is a relatively benign operation because of the choice to collapse the shortest edge of highly skewed elements; however, in the reference domain, the mesh motion is more severe because the edge being collapsed is not necessarily short. If only the nodes along the degenerated edge are moved as described above, the resulting elements will be distorted (Figure 8). This is particularly problematic if the ideal element is taken to be the reference element, i.e., $K_{\star,e} = \Omega_{0,e}$ (Section 4), because the objective function will drive the corresponding physical element toward this distorted element. In this work, we avoid this situation by removing the curvature from the elements in the reference domain (Figure 8); this approach is simpler than global mesh smoothing and works well in practice.

Remark 18. Element removal constitutes a fundamental change to the optimization problem as it alters the definition of the objective function and constraints and changes the number of optimization variables. Such operations are inconsistent with the spirit of optimization solvers that aim to find the solution of a given optimization problem and poses the risk of never converging to a meaningful solution if the underlying optimization problem is continually changing. In practice, all element collapses occur in the early optimization iterations meaning the optimization problem is fixed in the asymptotic regime and this issue does not arise.

5.2.2. Mesh straightening

For high-order meshes, it is not necessarily advantageous to remove ill-conditioned elements because such elements can be large (Figure 4d) so the associated edge collapse could be a severe mesh operation. This is

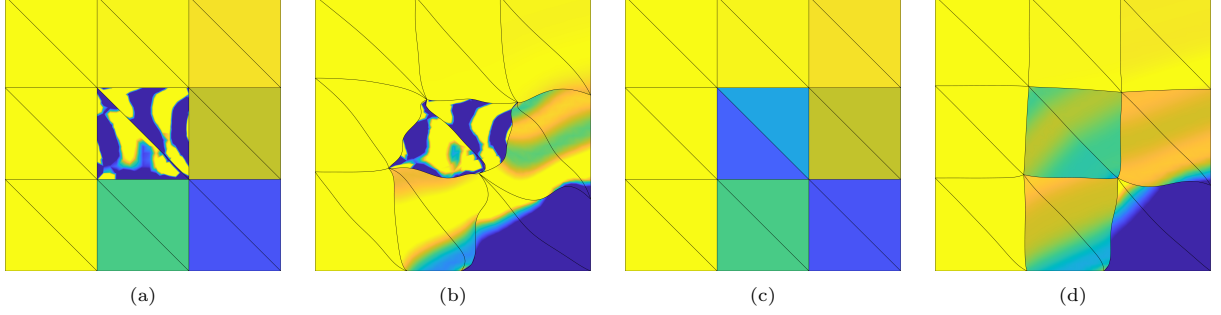


Figure 9: (a) An oscillatory intermediate shock tracking solution and mesh that can arise and (b) the corresponding SQP update (including line search). (c) The intermediate solution in (a) after re-initialization and (d) the corresponding SQP update (including line search). Oscillations in the DG solution lead to an SQP step that degrades the quality of the mesh and spreads the oscillations to neighboring elements, whereas the piecewise constant DG solution has a less severe effect.

not an issue for $q = 1$ (straight-sided) meshes because ill-conditioning is akin to a short edge whose collapse will be a benign mesh operation. Therefore, our approach is to only remove elements if they are inverted (Figure 4b), e.g., take $c_4 = 0$, and reset ill-conditioned elements to be straight-sided (from Figure 4d to Figure 4e). We define ill-conditioned elements to be elements in the set $\mathcal{E}_{\text{ill}}(\mathbf{x})$, where $\mathcal{E}_{\text{ill}} : \mathbb{R}^{N_{\mathbf{x}}} \rightarrow \mathcal{S}_h$ is defined as

$$\mathcal{E}_{\text{ill}} : \mathbf{x} \mapsto \{\Omega_{0,e} \in \mathcal{E}_h \mid g_{e,\text{inf}}(\mathbf{x}) \leq c'_4 g_{e,\text{sup}}(\mathbf{x})\} \quad (61)$$

and $c'_4 \in \mathbb{R}_{\geq 0}$; $c'_4 = 0.05$ in this work. In the SQP setting, this is applied after the element collapses in Section 5.2.1, i.e., we remove the high-order information from the elements in $\mathcal{E}_{\text{ill}}(\phi(\hat{\mathbf{y}}_{k+1}))$ to produce the new unconstrained degrees of freedom \mathbf{y}_{k+1} .

5.2.3. Solution re-initialization

We have observed that non-physical oscillations often arise in the DG solution at intermediate SQP steps, which lead to poor SQP search directions in subsequent iterations that require many line search iterations and substantially degrade both the mesh quality and DG solution. Numerical experiments have shown that resetting the DG solution in elements where it is oscillatory to a constant value promotes high-quality SQP search directions for both the mesh and DG solution (illustration in Figure 9, full numerical experiment in Figure 19). Our approach is to re-initialize the DG solution in an oscillatory element, identified using the Persson-Peraire shock sensor, with the average of the DG solution over a patch of elements in its vicinity.

Identification of oscillatory elements. To identify oscillatory elements, we turn to the shock capturing literature and use the popular shock sensor of Persson and Peraire [33], $s_e : \mathcal{V}_h^p \rightarrow \mathbb{R}$ for $e = 1, \dots, |\mathcal{E}_h|$, defined as

$$s_e : \bar{W}_h \mapsto \log_{10} \left(\sqrt{\frac{\int_{\Omega_{0,e}} (\chi(\bar{W}_h) - \chi(\Pi_{p-1} \bar{W}_h))^2 dV}{\int_{\Omega_{0,e}} \chi(\bar{W}_h)^2 dV}} \right), \quad (62)$$

where $\Pi_{p-1} : \mathcal{V}_h^p \rightarrow \mathcal{V}_h^{p-1}$ is a projection onto the space of piecewise polynomials of total degree $p - 1$ and $\chi : \mathbb{R}^m \rightarrow \mathbb{R}$ is a suitable scalar of the state. In this work, we choose $\chi : (W_1, \dots, W_m) \mapsto W_1$. Then, we define the set of oscillatory elements $\mathcal{E}_{\text{osc}} : \mathbb{R}^{N_{\mathbf{u}}} \rightarrow \mathcal{S}_h$ as all elements where the shock sensor exceeds a threshold, i.e.,

$$\mathcal{E}_{\text{osc}} : \mathbf{u} \mapsto \{\Omega_{0,e} \in \mathcal{E}_h \mid s_e(\Xi(\mathbf{u})) \geq c_5\}, \quad (63)$$

where $c_5 \in \mathbb{R}_{\geq 0}$. Numerical experiments have suggested it is advantageous to re-initialize not only elements in $\mathcal{E}_{\text{osc}}(\mathbf{u})$ but also neighboring elements. To this end, define $\mathcal{N} : \mathcal{S}_h \rightarrow \mathcal{S}_h$ as $\mathcal{N} : A \mapsto \mathcal{N}(A)$, where for any $K \in \mathcal{N}(A)$, there exists $K' \in A$ ($K \neq K'$) such that K and K' share a face (i.e., neighboring elements). Then the set of elements to be re-initialized, $\mathcal{E}_{\text{reinit}} : \mathbb{R}^{N_{\mathbf{u}}} \rightarrow \mathcal{S}_h$, is defined as

$$\mathcal{E}_{\text{reinit}} : \mathbf{u} \mapsto \mathcal{E}_{\text{osc}}(\mathbf{u}) \cup \mathcal{N}(\mathcal{E}_{\text{osc}}(\mathbf{u})). \quad (64)$$

In the case where the number of line search iterations is excessive (defined as more than 5 in this work), we

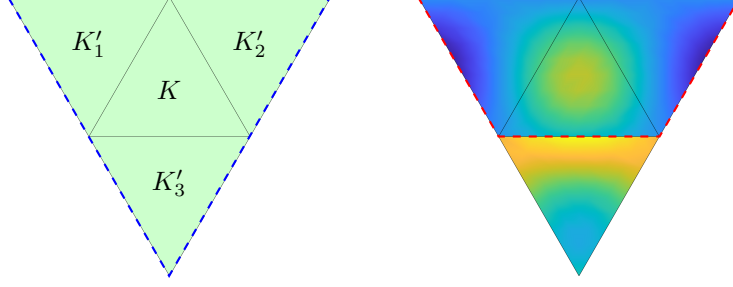


Figure 10: A mesh consisting of element K and its neighbors $\mathcal{N}(K) = \{K'_1, K'_2, K'_3\}$ (left) and a function $W_h \in \mathcal{V}_h^p$ ($p = 4$) with a strong jump between K and K'_3 (right), which leads to the shock-aware neighbors $\tilde{\mathcal{N}}(K, W_h) = \{K'_1, K'_2\}$. The set $K \cup \mathcal{N}(K)$ is enclosed in (---) and the set $K \cup \tilde{\mathcal{N}}(K)$ is enclosed in (- - -).

force re-initialization for a fraction of the most oscillatory elements despite not meeting the criteria in (63). That is, we re-define $\mathcal{E}_{\text{reinit}}$ as

$$\mathcal{E}_{\text{reinit}} : \mathbf{u} \mapsto \left\{ \Omega_{0,e} \in \mathcal{E}_h \mid s_e(\Xi(\mathbf{u})) \geq c_6 \max_{e'=1, \dots, |\mathcal{E}_h|} s_{e'}(\Xi(\mathbf{u})) \right\}, \quad (65)$$

where $c_6 \in \mathbb{R}_{\geq 0}$; in this work, we typically take $c_6 = 0.01$.

Re-initialization from patch of elements. With the oscillatory elements identified, we re-initialize them by resetting the DG solution in each of these elements to a constant value. The constant value assigned to element $K \in \mathcal{E}_{\text{init}}(\mathbf{u})$ is given by the average of the current DG solution (\mathbf{u}) over a patch of elements neighboring K without crossing the shock. To this end, define $a : \mathcal{E}_h \times \mathcal{E}_h \times \mathcal{V}_h^p \rightarrow \mathbb{R}$ as the average jump between two elements, i.e.,

$$a : (K, K', \bar{W}_h) \mapsto \frac{1}{|\partial K \cap \partial K'|} \int_{\partial K \cap \partial K'} \llbracket \chi(\bar{W}_h) \rrbracket dS, \quad |\partial K \cap \partial K'| := \int_{\partial K \cap \partial K'} dS, \quad (66)$$

where $\llbracket \cdot \rrbracket$ denotes the jump operator. Next, we define $\tilde{\mathcal{N}} : \mathcal{E}_h \times \mathbb{R}^{N_u} \rightarrow \mathcal{S}_h$ as

$$\tilde{\mathcal{N}} : (K, \mathbf{u}) \mapsto \{K' \in \mathcal{N}(K) \mid |a(K, K', \Xi(\mathbf{u}))| \leq c_7\}, \quad (67)$$

where $c_7 \in \mathbb{R}_{\geq 0}$, i.e., for $K \in \mathcal{E}_{\text{reinit}}(\mathbf{u})$, $\tilde{\mathcal{N}}(K, \mathbf{u}) \subset \mathcal{N}(K)$ is the set of elements that neighbor K that do not cross the shock (Figure 10). Finally, the DG solution in each element $K \in \mathcal{E}_{\text{reinit}}(\mathbf{u})$ is reset to the constant value $\zeta : \mathcal{E}_h \times \mathbb{R}^{N_u} \rightarrow \mathbb{R}$ given by

$$\zeta : (K, \mathbf{u}) \mapsto \frac{1}{|K \cup \tilde{\mathcal{N}}(K, \mathbf{u})|} \int_{K \cup \tilde{\mathcal{N}}(K, \mathbf{u})} \Xi(\mathbf{u}) dV. \quad (68)$$

In the SQP setting, elements are re-initialized after the mesh operations in Section 5.2.1-5.2.2, i.e., the elements in $\mathcal{E}_{\text{reinit}}(\hat{\mathbf{u}}_{k+1})$ are re-initialized, and \mathbf{u}_{k+1} is defined as

$$\Xi(\mathbf{u}_{k+1})|_K = \begin{cases} \zeta(K, \hat{\mathbf{u}}_{k+1}) & \text{if } K \in \mathcal{E}_{\text{reinit}}(\hat{\mathbf{u}}_{k+1}) \\ \Xi(\hat{\mathbf{u}}_{k+1})|_K & \text{otherwise.} \end{cases} \quad (69)$$

Termination of solution re-initialization. To ensure element re-initialization does not continue indefinitely, we only allow re-initialization for iterations k such that

$$\|\mathbf{r}_k\| > c_8, \quad k \leq M, \quad (70)$$

where $c_8 \in \mathbb{R}_{\geq 0}$ and M is defined in Section 5.1.4. The first condition prevents re-initialization when the constraints are nearly satisfied because this condition usually only happens near convergence where re-

initialization of the DG solution would interfere with clean and rapid convergence. This condition is usually sufficient to ensure re-initialization terminates after a finite number of iterations. The second condition is a safeguard to ensure $\Upsilon_k = \text{Id}$ for $k > M$.

Remark 19. After solution re-initialization, it can be advantageous to also straighten the elements in $\mathcal{E}_{\text{reinit}}$, i.e., remove high-order geometry information, as discussed in Section 5.2.2 to remove highly curved edges from intermediate configurations. This combination is especially helpful for problems with complex shock structures, but not necessary for simpler problems.

Remark 20. A major concern in the context of compressible flows is whether oscillations will lead to catastrophic breakdown of the solution, which usually manifests as negative pressures and densities throughout the domain. While the oscillations that arise during the optimization iterations adversely impact the performance of the SQP solver, negative pressures and densities do not arise at accepted iterations because the line search ensures sufficient decrease of the merit function. That is, suppose iteration \mathbf{z}_k is free of negative pressures and densities and recall $\mathbf{z}_{k+1} = \mathbf{z}_k + \alpha_k \Delta \mathbf{z}_k$. The backtracking line search will choose α_k sufficiently small that \mathbf{z}_{k+1} leads to sufficient decrease of the merit function, which cannot be a state with negative pressures and densities. Therefore, the line search is sufficient to ensure the sequence $\{\mathbf{z}_k\}_{k=0}^\infty$ is free of negative pressures and densities; however, the re-initialization procedure is necessary to avoid steps becoming prohibitively small as the DG solution at intermediate iterations becomes oscillatory.

Remark 21. Both element removal or solution re-initialization are operations that cause abrupt changes to the objective function and constraints, which interferes with the value of κ that has been calibrated as the optimization iterations progress. Suppose either an element is removed or the DG solution is re-initialized at iteration k , then we take

$$\kappa_{k+1} = \max \left\{ v \sqrt{\frac{f_{\text{err}}(\mathbf{z}_{k+1})}{f_{\text{msh}}(\mathbf{y}_{k+1})}}, \kappa_{\min} \right\} \quad (71)$$

to balance the tracking and mesh quality objectives.

5.3. SQP initialization

The HOIST optimization problem in (27) is a nonlinear, non-convex program, which makes the starting point for the optimization solver important. Let $\mathbf{X} \in \mathbb{R}^{N_\star}$ be the nodal coordinates of the reference mesh \mathcal{E}_h , i.e., concatenation of $\{\hat{X}_I\}_{I=1}^{N_\star}$ into a vector, which is produced through a mesh generation procedure agnostic to the shock location. Then, we take the initial physical mesh to be the reference mesh, $\mathbf{x}_0 = \mathbf{X}$, and the corresponding unconstrained degrees of freedom are determined as

$$\mathbf{y}_0 = \mathbf{A}^\dagger(\mathbf{x}_0 - \mathbf{b}), \quad (72)$$

i.e., the least-squares fit to the physical mesh, in the case where all domain boundaries are planar; otherwise, we solve the nonlinear least-square problem: $\mathbf{y}_0 = \arg \min_{\mathbf{y} \in \mathbb{R}^{N_\mathbf{y}}} \|\phi(\mathbf{y}) - \mathbf{x}_0\|$. Because $\mathbf{x}_0 = \mathbf{X}$ lies in the range of \mathbf{A} by construction (Section 3.2), perfect inversion (to the tolerances of the linear solver) of the parametrization is guaranteed ($\mathbf{x}_0 = \mathbf{A}\mathbf{y}_0 + \mathbf{b}$). The corresponding DG solution is initialized from the first-order finite volume or $p = 0$ DG solution on the shock-agnostic initial mesh $\mathcal{G}_h(\mathcal{E}_h; \mathbf{x}_0)$ because it is simple, fast, and does not require stabilization. Numerical investigations into more sophisticated initialization of the DG solution— L^2 projection of the exact solution and shock capturing solutions based on artificial viscosity—did not offer noticeable advantages over this simple choice.

Remark 22. The approach described in this section is always used to initialize the SQP solver, regardless of polynomial degrees (p and q). This is in stark contrast to the predecessor to this work [48] that required a homotopy procedure: the strategy described in this section was used to initialize a $p = q = 1$ simulation, which was in turn used to initialize $p > 1, q > 1$ simulations. The robustness measures in Section 5.2 are the key innovations of this work that enable reliable convergence for complex flows from a simple, generic starting point (shock agnostic mesh and corresponding first-order finite volume solution) for any polynomial degrees.

5.4. Complete algorithm

The complete HOIST method described in Section 5 is summarized in Algorithm 1 for domains with planar boundaries. The only generalization required for non-planar boundaries is the definition of ϕ for curved surfaces [11, 46, 48] and definition of \mathbf{y}_0 via nonlinear least-squares (Section 5.3).

Algorithm 1 HOIST method

Input: Reference mesh \mathcal{E}_h with nodal coordinates \mathbf{X} , the parameters in Table A.4, and tolerances ϵ_1, ϵ_2

Output: Shock-aligned mesh $\phi(\mathbf{y}^*)$ and corresponding DG solution \mathbf{u}^*

- 1: **Construct parametrization:** Construct \mathbf{A} and \mathbf{b} according to Section 3.2 and define ϕ from (17)
 - 2: **Solution initialization:** Define \mathbf{y}_0 from (72) and \mathbf{u}_0 as the DG($p = 0$) solution on the reference mesh
 - 3: **for** $k = 0, 1, 2, \dots$ **do**
 - 4: **SQP search direction:** Compute $\Delta \mathbf{z}_k$ from (43)
 - 5: **Line search:** Determine α_k that satisfies (44) by backtracking
 - 6: **SQP update:** Compute $\tilde{\mathbf{z}}_{k+1} = \mathbf{z}_k + \alpha_k \Delta \mathbf{z}_k$
 - 7: **Check convergence:** Terminate iterations with $(\mathbf{u}^*, \mathbf{y}^*) = (\tilde{\mathbf{z}}_{k+1})$ if $\|\mathbf{r}(\tilde{\mathbf{z}}_{k+1})\| \leq \epsilon_1$, $\|\mathbf{c}(\tilde{\mathbf{z}}_{k+1})\| \leq \epsilon_2$
 - 8: **Modify SQP step:** Compute $\mathbf{z}_{k+1} = \Upsilon_{k+1}(\tilde{\mathbf{z}}_{k+1})$
 - **Remove elements** in set $\mathcal{E}_{\text{rmv}}(\phi(\tilde{\mathbf{y}}_{k+1}))$
 - Fix connectivity to define new mesh (\mathcal{E}_h) with physical nodes $\hat{\mathbf{x}}_{k+1}$
 - Reconstruct parametrization ϕ and unconstrained degrees of freedom $\hat{\mathbf{y}}_{k+1} = \mathbf{A}^\dagger(\hat{\mathbf{x}}_{k+1} - \mathbf{b})$
 - Transfer solution to new mesh $\hat{\mathbf{u}}_{k+1}$
 - **Straighten elements** in set $\mathcal{E}_{\text{ill}}(\phi(\hat{\mathbf{y}}_{k+1}))$ to yield \mathbf{x}_{k+1} and $\mathbf{y}_{k+1} = \mathbf{A}^\dagger(\mathbf{x}_{k+1} - \mathbf{b})$
 - **Re-initialize solution** in elements in set $\mathcal{E}_{\text{reinit}}(\hat{\mathbf{u}}_{k+1})$ to yield \mathbf{u}_{k+1} from (69), provided $\|\mathbf{r}(\tilde{\mathbf{z}}_{k+1})\| > c_8$ and $k \leq M$
 - 9: **end for**
-

6. Numerical experiments

In this section, we demonstrate the HOIST framework on a sequence of increasingly difficult inviscid conservation laws with discontinuous solutions in $d = 1, 2, 3$. In particular, we show the HOIST method achieves optimal $\mathcal{O}(h^{p+1})$ convergence rates and the proposed solver is able to robustly track complex discontinuity surfaces (e.g., contact discontinuities, curved and reflecting shocks, shock formation, and shock-shock interaction) as well as surfaces along which the solution is continuous but its derivative is discontinuous (e.g., head and tail of rarefactions).

6.1. Linear advection

Consider steady, linear advection of a scalar quantity $U : \Omega \rightarrow \mathbb{R}$ through a domain $\Omega \subset \mathbb{R}^d$

$$\nabla \cdot (U(x)\beta(x)^T) = 0 \quad \text{for } x \in \Omega, \quad U(x) = U_\infty(x) \quad \text{for } x \in \Gamma_{\text{in}}, \quad (73)$$

where $\beta : \Omega \rightarrow \mathbb{R}^d$ is the local flow direction, $\Gamma_{\text{in}} := \{x \in \partial\Omega \mid \beta(x) \cdot n(x) < 0\}$ is the inflow boundary, and $U_\infty : \Omega \rightarrow \mathbb{R}$ is the inflow boundary condition. For the DG discretization, we use the smoothed upwind flux described in [48, 47] as the inviscid numerical flux function.

6.1.1. Straight shock, piecewise constant solution

First, we consider a three-dimensional problem ($d = 3$) with a planar shock surface and piecewise constant solution (test case: `advect-planar`) to demonstrate the HOIST method in a simple three-dimensional setting.

Table 1: Legend for SQP convergence history and parameter adaption plots, including the DG residual ($\|\mathbf{r}(\mathbf{u}_k, \phi(\mathbf{y}_k))\|$), enriched DG residual ($\|\mathbf{R}(\mathbf{u}_k, \phi(\mathbf{y}_k))\|$), optimality condition ($\|\mathbf{c}(\mathbf{u}_k, \mathbf{y}_k)\|$) ($\text{---}\bullet\text{---}$), mesh distortion ($\|\kappa_k \mathbf{R}_{\text{msh}}(\phi(\mathbf{y}_k))\|$), step size (α_k), mesh regularization parameter (γ_k), and mesh distortion parameter (κ_k).

$\ \mathbf{r}(\mathbf{u}_k, \phi(\mathbf{y}_k))\ $	$\ \mathbf{R}(\mathbf{u}_k, \phi(\mathbf{y}_k))\ $	$\ \mathbf{c}(\mathbf{u}_k, \mathbf{y}_k)\ $	$\ \kappa_k \mathbf{R}_{\text{msh}}(\phi(\mathbf{y}_k))\ $	α_k	γ_k	κ_k
(\bullet)	(\bullet)	($\text{---}\bullet\text{---}$)	($\text{---}\bullet\text{---}$)	(---)	(---)	(---)

Consider the domain $\Omega := (-1, 1) \times (0, 1) \times (0, 1)$ with constant advection field and piecewise constant boundary condition

$$\beta : x \mapsto (-1.25, 1, 0), \quad U_\infty : x \mapsto H(x_1), \quad (74)$$

where $H : \mathbb{R} \rightarrow \{0, 1\}$ is the Heaviside function; this is the three-dimensional extrusion of the problem considered in [48]. We label the six planar boundaries $\{\partial\Omega_i\}_{i=1}^6$, where $\partial\Omega_i$ has outward unit normal $\eta_i = -e_i$ for $i = 1, 2, 3$ and $\partial\Omega_{i+d}$ has outward unit normal $\eta_i = e_i$ for $i = 1, 2, 3$. The choice of advection field implies $\Gamma_{\text{in}} = \partial\Omega_2 \cup \partial\Omega_4$. To ensure the Heaviside function is accurately represented and integrated in the weak form along boundary $\partial\Omega_2$, we require the reference mesh to have element edges aligned with the line $\{(0, 0, s) | s \in [0, 1]\}$ and do not allow the corresponding nodes to move throughout the HOIST iterations (Figure 11).

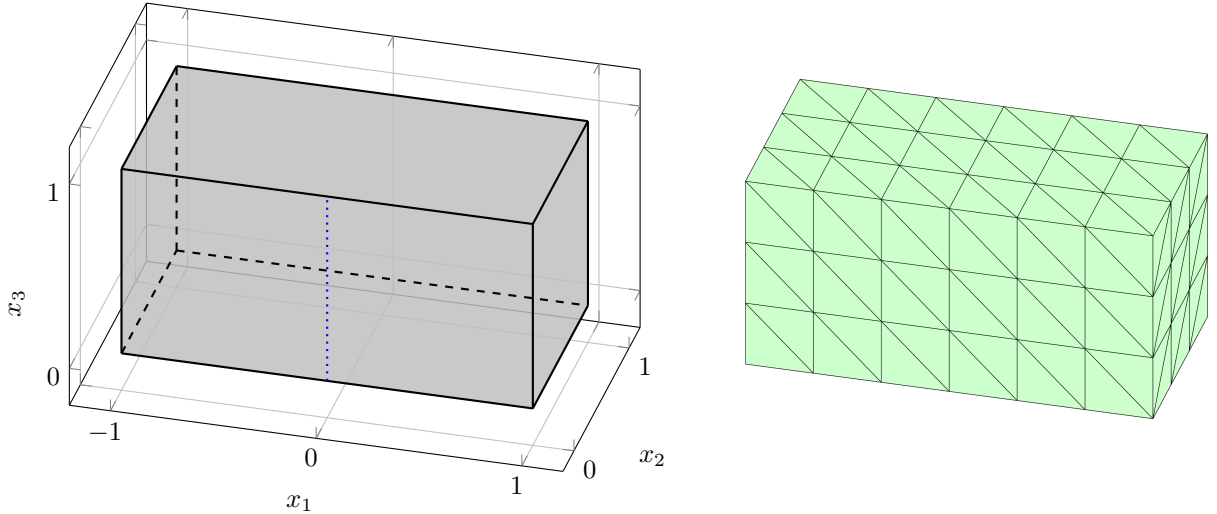


Figure 11: The domain for the advection experiments in Sections 6.1.1 and 6.1.2; the reference mesh is constructed such that element edges lie along ($\text{---}\bullet\text{---}$) and the corresponding nodes are constrained to slide along ($\text{---}\bullet\text{---}$) to ensure the Heaviside function is integrated accurately.

We discretize the domain using a structured mesh consisting of 324 uniform right tetrahedra. Because the analytical solution is piecewise constant with a straight-sided discontinuity surface, we choose a $p = 0$ solution and $q = 1$ mesh approximation. The HOIST parameters are defined in Table A.4. Because of the piecewise constant ($p = 0$) DG solution, we do not perform re-initialization and the mesh quality term in the objective function is not necessary (the enriched residual induces minute mesh motion away from the shock).

Starting from a shock-agnostic (structured) mesh and first-order finite volume solution, only 29 SQP iterations are required to track the discontinuity surface with the mesh (Figure 12) and reduce the standard DG residual to a magnitude of $\mathcal{O}(10^{-10})$ and the enriched residual to $\mathcal{O}(10^{-8})$ with no elements being removed during the solution procedure. The SQP convergence history and behavior of the adaptive parameters are shown in Figure 13. The mesh tracks the shock nearly perfectly at iteration 23 and exhibits Newton-like convergence after that point (Figure 13).

6.1.2. Curved shock, piecewise constant solution

Next, we consider a three-dimensional problem ($d = 3$) with a curved (trigonometric) shock surface (test case: `advect-trig`) to demonstrate the HOIST method is able to represent curved discontinuity surfaces in

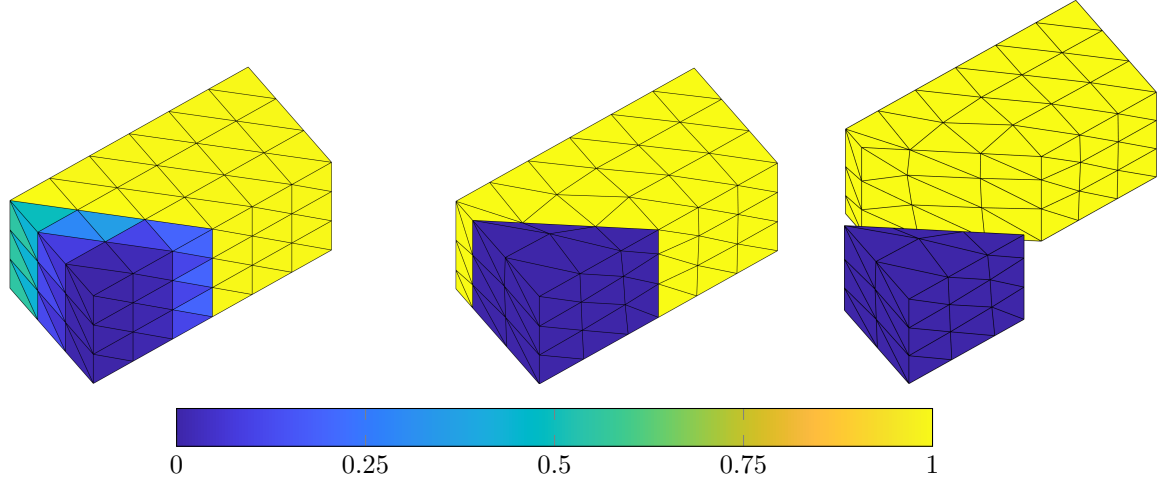


Figure 12: The starting point (*left*) and the tracked configuration (*middle*) for the **advect-planar** test case. The mesh is separate along the discontinuity surface for a clearer view of the tracked mesh (*right*).

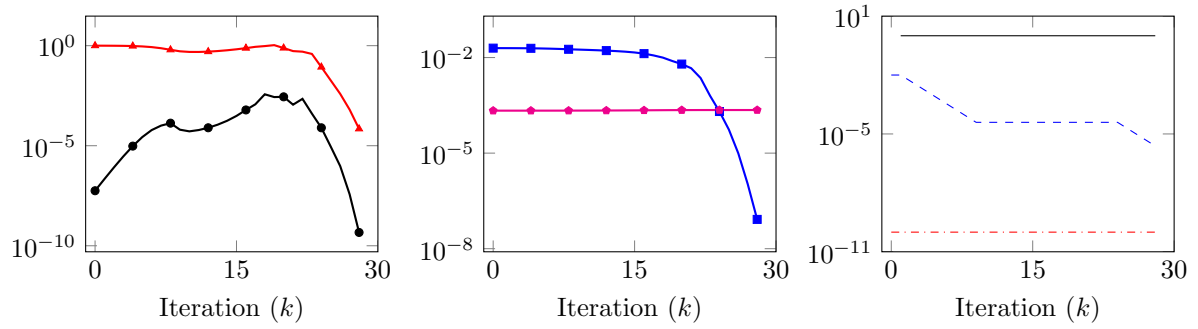


Figure 13: SQP convergence history and behavior of adaptive parameters for the **advect-planar** test case (legend in Table 1).

three dimensions. Consider the domain $\Omega := (-1, 1) \times (0, 1) \times (0, 1)$ with trigonometric advection field and piecewise constant boundary condition

$$\beta : x \mapsto (-\sin(\pi x_2), 1, 0), \quad U_\infty : x \mapsto H(x_1); \quad (75)$$

this is the three-dimensional extrusion of the problem considered in [48]. Similar to the previous section, we require the reference mesh to have element edges aligned with the line $\{(0, 0, s) | s \in [0, 1]\}$ to ensure the Heaviside function is accurately represented and integrated along boundary $\partial\Omega_2$ (same boundary labeling as Section 6.1.1) and discretize the domain using a structured mesh consisting of 324 uniform right tetrahedra (Figure 11). Because the analytical solution is piecewise constant, we again use a $p = 0$ DG solution; however, we use a $q = 2$ mesh to approximate the shock surface to third-order accuracy. The HOIST parameters are defined in Table A.4, which are identical to the planar case except we take $c'_4 = 0.05$ to prevent high-order elements from becoming singular.

Starting from a shock-agnostic (structured) mesh and first-order finite volume solution, the HOIST method leads to an accurate solution and a curved mesh that is well-aligned with the discontinuity surface (Figure 14) and the magnitude of the standard and enriched DG residual are reduced $\mathcal{O}(10^{-8})$ and $\mathcal{O}(10^{-4})$, respectively; 12 element collapses are required. Unlike the planar case, we do not see Newton-like convergence; however, we observe a rapid drop in the residual from $\mathcal{O}(10^{-2})$ to $\mathcal{O}(10^{-6})$ in just 11 iterations ($k = 33$ to $k = 45$) once the discontinuity surface is nearly tracked (Figure 15). The main difference between the planar and trigonometric shock case is that the analytical solution lies in the nonlinear approximation space (defined as the composition of the DG solution with the domain mapping) in the planar case, whereas it does not in the trigonometric case. As a result, the enriched DG residual also converged to a near-zero optimal value $\mathcal{O}(10^{-8})$ in the planar case, whereas it was much larger in the trigonometric case $\mathcal{O}(10^{-4})$, which implies the Levenberg-Marquardt Hessian in (48)-(49) is a better approximation to the true Hessian of the objective function in the planar case and likely the reason for the different convergence rates.

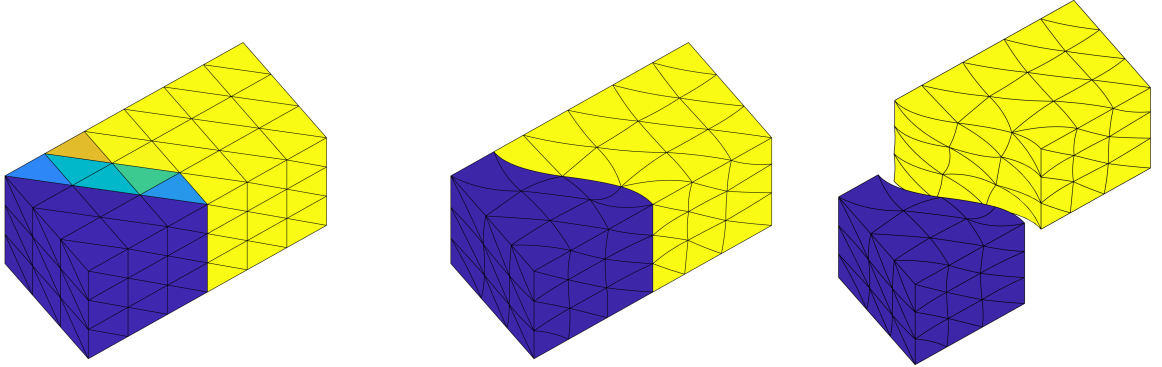


Figure 14: The starting point (*left*) and the tracked configuration (*middle*) for the **advect-trig** test case. The mesh is separate along the discontinuity surface for a clearer view of the tracked mesh (*right*). Colorbar in Figure 12.

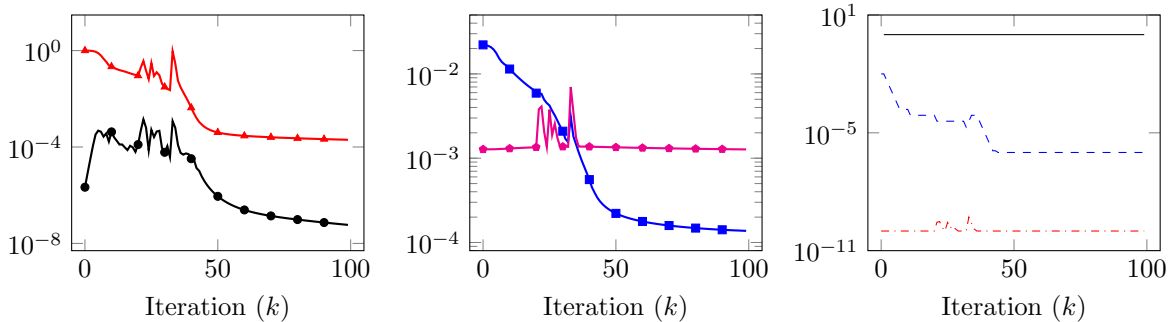


Figure 15: SQP convergence history and behavior of adaptive parameters for for the **advect-trig** test case (legend in Table 1).

6.2. Inviscid Burgers' equation

Next, we consider the time-dependent, inviscid Burgers' equation that governs nonlinear advection of a scalar quantity $\phi : \Omega \rightarrow \mathbb{R}$ through a one-dimensional domain $\bar{\Omega} \subset \mathbb{R}$

$$\frac{\partial}{\partial t} \phi(z, t) + \phi(z, t) \frac{\partial}{\partial z} \phi(z, t) = 0, \quad \phi(z, 0) = \phi_0(z) \quad (76)$$

for all $z \in \bar{\Omega}$ and $t \in \mathcal{T}$ with the initial condition $\phi_0 : \Omega \rightarrow \mathbb{R}$. This leads to a conservation law of the form (1) over the space-time domain $\Omega := \bar{\Omega} \times \mathcal{T}$ with conservative variable $U : \Omega \rightarrow \mathbb{R}$ and flux function $F : \mathbb{R} \rightarrow \mathbb{R}^{1 \times 2}$

$$U : x \mapsto \phi(x_1, x_2), \quad F : W \mapsto [W^2/2 \quad W]. \quad (77)$$

that is identical to the advection equation in (73) with local space-time flow direction $\beta : x \mapsto (U(x)/2, 1)$. For the DG discretization, we use the smoothed upwind flux described in [48] as the inviscid numerical flux function.

6.2.1. Shock acceleration

First, we consider an accelerating shock (test case: **iburg-acc**) in the one-dimensional spatial domain $\bar{\Omega} := (-0.2, 1)$ and temporal domain $\mathcal{T} = (0, 1.2)$ produced by the initial condition

$$\phi_0 : z \mapsto \mu_1 H(-z) - \mu_2 H(z) \quad (78)$$

and boundary condition $\phi(-0.2, t) = \mu_1$ for $t \in \mathcal{T}$; in this work, we take $\mu_1 = 4$ and $\mu_2 = 3$. The analytical solution is

$$\phi : (z, t) \mapsto \mu_1 H(z_s(t) - z) + \frac{\mu_2(z - 1)}{1 + \mu_2 t} H(z - z_s(t)), \quad (79)$$

where $z_s : \mathcal{T} \rightarrow \mathbb{R}$ is the shock speed

$$z_s : t \mapsto (\mu_1/\mu_2 + 1)(1 - \sqrt{1 + \mu_2 t}) + \mu_1 t; \quad (80)$$

both are shown in Figure 16. The purpose of this numerical experiment is to provide a detailed investigation into the proposed HOIST solver for polynomial degrees $p = 1, 2, 3$ and verify optimal convergence rate of the PDE solution (ϕ) and shock position (z_s) of the method for a two-dimensional, nonlinear problem.

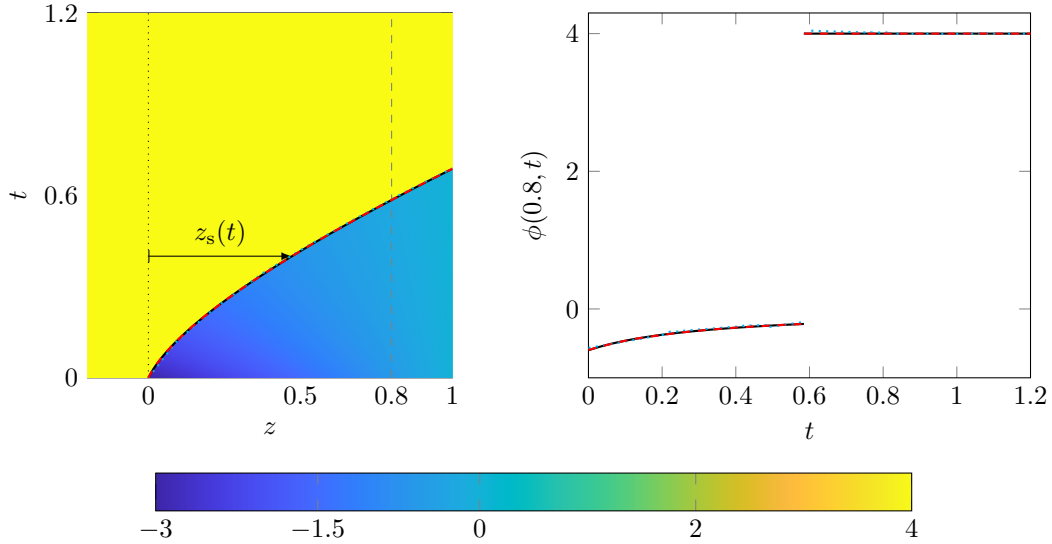


Figure 16: Analytical space-time solution to the **iburg-acc** test case with shock surface (—) (left) and the corresponding solution along the line $\{(0.8, t) \mid t \in [0, 1]\}$ (---) (right). The corresponding quantities for the $p = 1$ (.....) and $p = 2$ (---) HOIST simulations are also shown for comparison. The $p > 2$ HOIST solutions are not shown for clarity because they are visually indistinguishable from the $p = 2$ solution, which in turn overlaps the analytical quantity.

Due to the curvature of the shock in space-time, we choose to approximate the mesh with the same polynomial degree as the solution field, i.e., $q = p$. We discretize the space-time domain with a structured mesh of 72 right triangles and use this mesh to initialize all HOIST simulations. Furthermore, the mesh was constructed such that the hypotenuse of each triangle traverses the discontinuity surface making the initial mesh far from alignment with the shock (Figure 17). The same HOIST parameters are used for all polynomial degrees considered (Table A.4), except we take $\gamma_0 = \gamma_{\min} = 1$ in the $p = 1$ case because the solution is under-resolved and the more conservative choice is required.

For all three cases, the proposed solver simultaneously updates the mesh and solution until the discontinuity is tracked, the fully discrete PDE is satisfied on the discontinuity-aligned mesh, and elements away from the discontinuity approach equilateral triangles (owing to the choice of $K_{\star,e} = K_\star$) (Figure 17). The number of elements removed in each case is: 1 ($p = 1$), 1 ($p = 2$), and 7 ($p = 3$). In the $p = 1$ case, the solution is somewhat underresolved as evident by the faceted approximation to the discontinuity, although this is expected given the coarseness of the mesh. For all other cases, the shock is tracked using curved, high-order elements and the solution is well-resolved. Both the space-time discontinuity surface and slice of the conserved variable from the HOIST solution are visually indistinguishable from the corresponding analytical quantity for $p \geq 2$ (Figure 16).

The SQP solver converges to the solution the optimization problem (27) rapidly considering the starting point is far from the HOIST solution. The discontinuity is mostly tracked after only 20 iterations and tracked to the extent possible given the resolution limits of the discretization by iteration 30 (Figure 17). In all cases, the first-order optimality criteria are driven to relatively tight tolerances within 100 iterations; after the element collapses cease and the topology of the shock has been discovered (around iteration 20), the DG residuals and optimality condition decrease sharply (Figure 18). The $p = 2$ simulation is an outlier because it is effectively converged by iteration 10, which is significantly faster than the other polynomial degrees considered. We attribute this to the $p = 1$ simulation being under-resolved (requires more conservative parameters) and the $p > 2$ elements requiring more frequent re-initializations because they are more susceptible to oscillations. In our experience, $p = 2$ tends to be the “sweet” spot for the HOIST method and is used extensively in the remaining numerical experiments.

Oscillatory solutions arise in some elements during intermediate iterations, particularly for the higher polynomial degrees (Figure 17); however, the element-wise re-initialization (Section 5.2.3) removes them, which ensures the solver can continue without solution and mesh degradation. Without re-initializations, the SQP solver can effectively stall because the oscillatory solution leads to poor search directions (Section 5.2.3) that eventually cause the step length (α_k) to become very small to satisfy the line search criteria in (44). To demonstrate this, we consider the $p = 3$ HOIST simulation without re-initialization (all other parameters unchanged) and see that while the shock is mostly tracked, a few oscillatory elements have stalled progress to the solution (Figure 19). By contrasting to the HOIST solution (Figure 17) and SQP solver performance (Figure 18) with re-initialization, it is clear that re-initialization is important for robust convergence.

Finally, we study the h -convergence of the HOIST method for this problem using the analytical solution to confirm it achieves optimal convergence rates $\mathcal{O}(h^{p+1})$ for the polynomial degrees $p = 1, 2, 3$. Because HOIST shock will not be exactly aligned with the analytical shock position, it is difficult to compute standard integral-based errors over the space-time domain as one would need to intersect the HOIST mesh with exact shock location to accurately compute the integrals using numerical quadrature, which is far from straightforward for curved meshes, e.g., see [21]. Instead, we consider two one-dimensional error metrics: $E_\phi : \mathbb{R}^{N_u} \times \mathbb{R}^{N_x} \rightarrow \mathbb{R}$, the L^1 error in the solution along the line $\{(0.8, t) \mid t \in [0, 1]\}$, and $E_{z_s} : \mathbb{R}^{N_x} \rightarrow \mathbb{R}$, the L^2 error in the shock position, i.e.,

$$E_\phi : (\mathbf{u}, \mathbf{x}) \mapsto \int_0^1 \left| \phi(\bar{z}, t) - \hat{\phi}(\bar{z}, t; \mathbf{u}, \mathbf{x}) \right| dt, \quad E_{z_s} : \mathbf{x} \mapsto \sqrt{\int_0^1 |z_s(t) - \hat{z}_s(t; \mathbf{x})|^2 dt}, \quad (81)$$

where $\hat{\phi} : \mathcal{T} \times \bar{\Omega} \times \mathbb{R}^{N_u} \times \mathbb{R}^{N_x} \rightarrow \mathbb{R}$ is the HOIST approximation to ϕ given by $\hat{\phi} : (z, t, \mathbf{u}, \mathbf{x}) \mapsto \Xi(\mathbf{u}) \circ \mathcal{G}_h^{-1}((z, t); \mathbf{x})$ and $\hat{z}_s : \mathcal{T} \times \mathbb{R}^{N_x} \rightarrow \mathbb{R}$ is the HOIST approximation to the shock position. The integral in E_ϕ is computed accurately by slicing the physical mesh to create a one-dimensional mesh, intersecting it with the exact position of the shock, and integrating using Gaussian quadrature over each element of the one-dimensional super-mesh. We use the L^1 error for the solution because it contains a discontinuity and we expect the L^1 error to converge at a given rate provided the smooth solution and position of the discontinuity

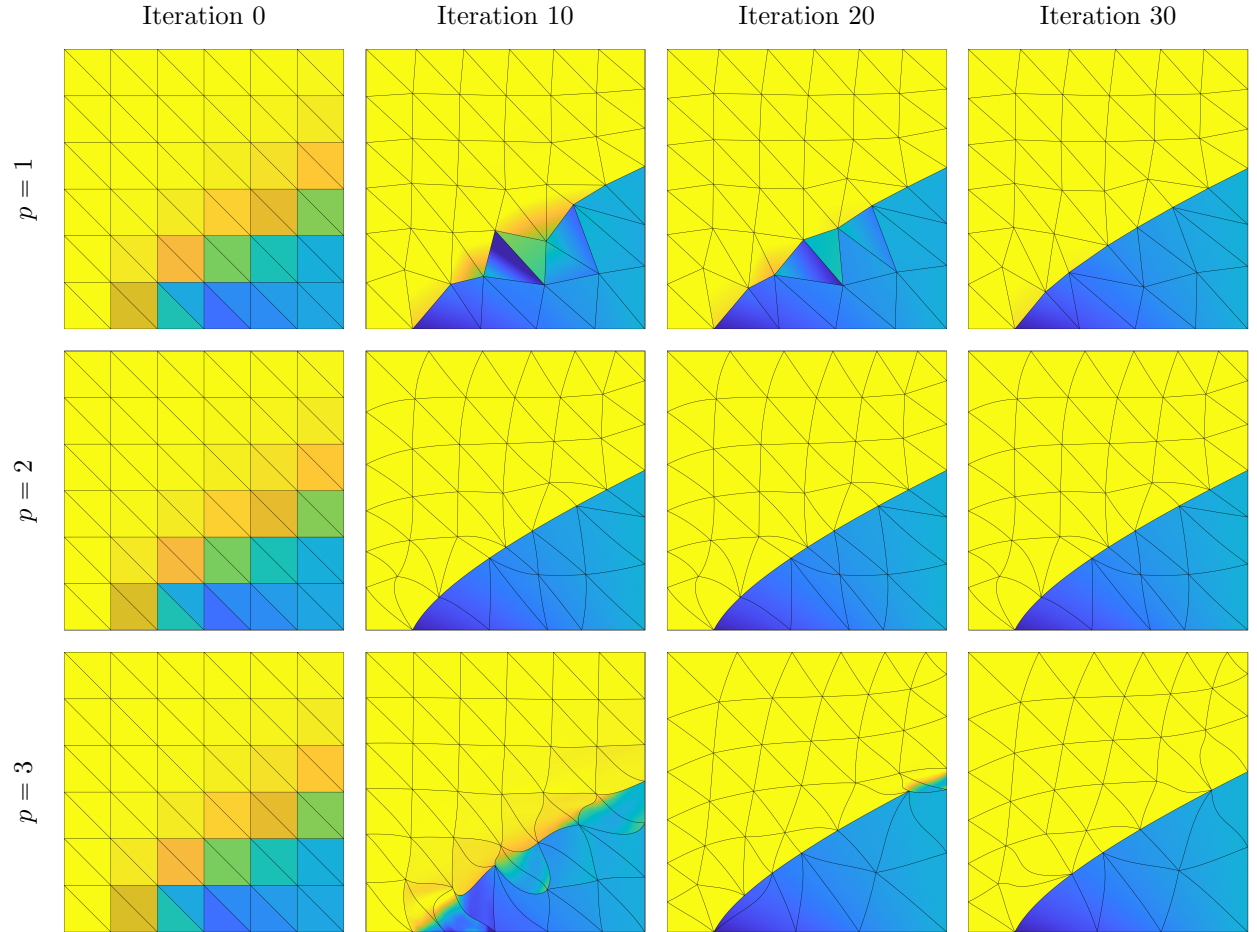


Figure 17: Selected HOIST iterations for the **iburg-acc** test case for $p = 1, 2, 3$ (*top-to-bottom*) at iterations $k = 0, 10, 20, 30$ (*left-to-right*). Colorbar in Figure 16.

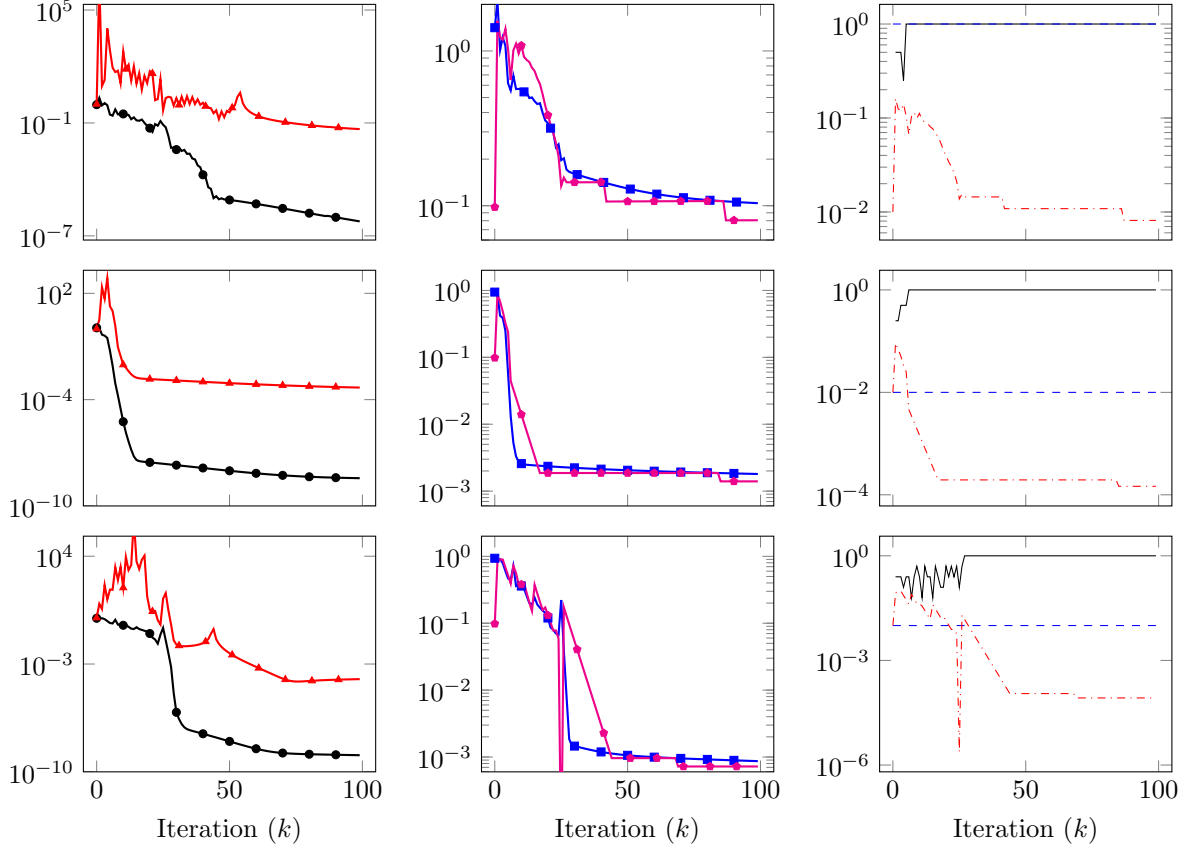


Figure 18: SQP convergence history and behavior of adaptive parameters for the **iburg-acc** test case (legend in Table 1) for $p = 1, 2, 3$ (top-to-bottom).

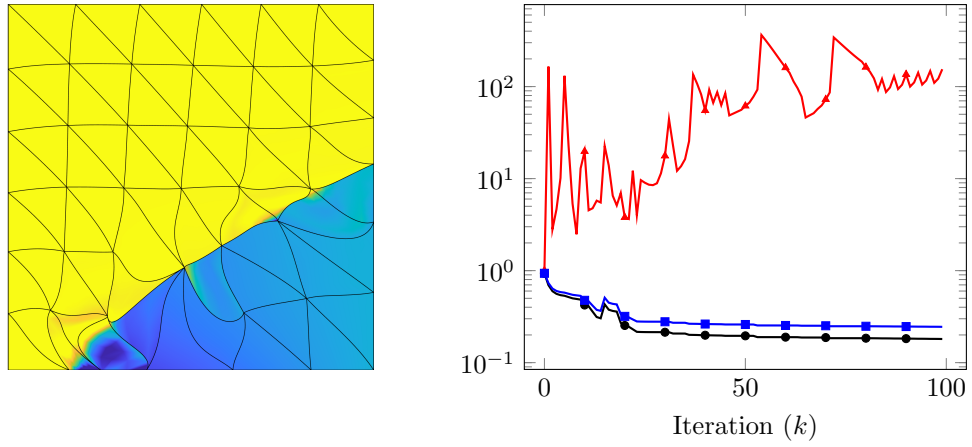


Figure 19: HOIST solution ($p = 3$) to the **iburg-acc** test case without re-initialization (left) (colorbar in Figure 16) and the corresponding SQP convergence history (right) (legend in Table 1).

Table 2: Tabulated convergence results for the **iburg-acc** test case corresponding to the curves in Figure 20. The segment-wise slope of the curves ($m(\cdot)$) tends to at least the optimal rate ($p + 1$) as the mesh is refined.

p	q	$ \mathcal{E}_h $	h	E_ϕ	$m(E_\phi)$	E_{z_s}	$m(E_{z_s})$
1	1	38	1.45e-01	2.72e-02	-	2.32e-03	-
1	1	152	7.25e-02	7.18e-03	1.92	1.09e-03	1.09
1	1	598	3.66e-02	1.91e-03	1.93	1.93e-04	2.53
1	1	2392	1.83e-02	4.69e-04	2.03	3.92e-05	2.30
2	2	38	1.45e-01	5.68e-03	-	4.83e-05	-
2	2	152	7.25e-02	9.64e-05	5.88	2.70e-07	7.48
2	2	608	3.63e-02	6.36e-06	3.92	1.20e-08	4.49
2	2	2432	1.81e-02	8.66e-07	2.88	7.70e-10	3.96
3	3	32	1.58e-01	1.57e-03	-	2.06e-05	-
3	3	128	7.91e-02	1.62e-05	6.60	3.37e-07	5.93
3	3	512	3.95e-02	4.37e-07	5.21	5.90e-09	5.84
3	3	2040	1.98e-02	3.31e-08	3.73	1.87e-10	5.00

converge at that rate [48]. We consider four levels of refinement generated by uniformly refining a coarse initial mesh (each triangular element split into four elements); due to element collapses, the number of elements in each refinement level does not necessarily contain four times the elements of the previous level. We observe optimal convergence rate for E_ϕ and better-than-optimal convergence rates in E_{z_s} (Figure 20, Table 2).

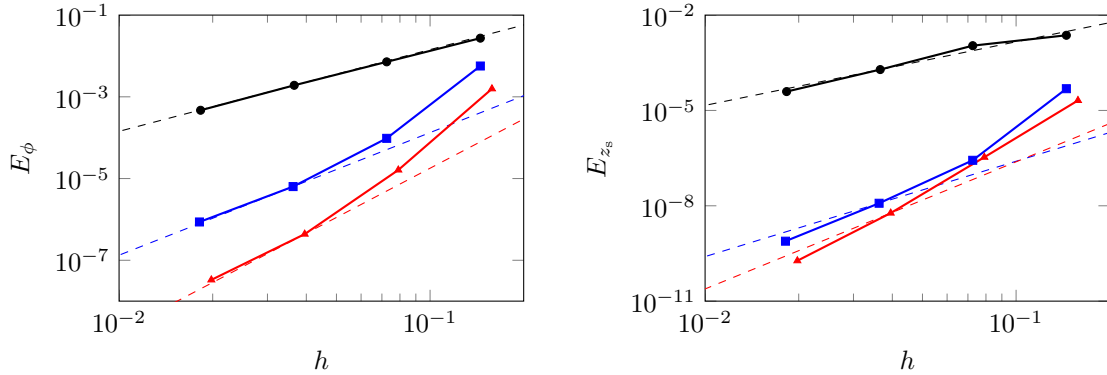


Figure 20: h -convergence of the HOIST method for the **iburg-acc** test case for both error metrics, E_ϕ (left) and E_{z_s} (right), for polynomial degrees $p = 1$ (—●—), $p = 2$ (—■—), and $p = 3$ (—▲—). The dashed lines indicate the optimal convergence rate ($p + 1$).

6.2.2. Shock formation and merge

Next, we consider a problem in which a smooth initial condition forms two distinct shock waves that eventually merge (test case: **iburg-form**) to demonstrate the ability of the HOIST method to handle shock formation and intersection. Consider Burgers' equation in (76) over the one-dimensional spatial domain $\bar{\Omega} := (-1, 1)$ and temporal domain $\mathcal{T} = (0, 1)$ with the initial condition

$$\phi_0 : z \mapsto 1.2 \exp\left(-\frac{(z + 0.5)^2}{0.025}\right) - \exp\left(-\frac{(z - 0.5)^2}{0.025}\right) \quad (82)$$

and boundary conditions $\phi(-1, t) = \phi_0(-1)$ and $\phi(1, t) = \phi_0(1)$ for $t \in \mathcal{T}$.

We discretize the space-time domain using a structured mesh of 400 right triangles and, because shock formation requires substantial resolution to represent the steepening shock, we only consider polynomial degrees $p = 2, 3$. Similar to the accelerating shock case, the shocks are curved in space-time so we choose the

mesh and solution approximation to be the same polynomial degree ($q = p$). The same HOIST parameters are used for both the $p = 2, 3$ simulations (Table A.4).

For both polynomial degrees, the HOIST method is able to track the shocks during and after formation, including the point at which they merge (a triple point in space-time) despite starting from a mesh that incorporates no knowledge of the discontinuity surface (Figure 21). In space-time, shock formation essentially requires infinite resolution because the smooth features continually steepen until the instant at which they become discontinuities. For this reason, any space-time discretization will be under-resolved in the vicinity of shock formation. In the region where the steepness of the forming shock has exceeded the resolution in the discretization, the HOIST method approximates the steep, continuous feature with a discontinuity that grows until the shock is fully formed (Figure 22). Despite the features present in this problem (shock formation and a triple point), the proposed solver converges rapidly to a critical point, especially the $p = 2$ simulation (Figure 23). The $p = 3$ simulation is slightly slower because the solution becomes more oscillatory at intermediate iterations, which requires more re-initializations (jumps in the convergence plots in Figure 23).

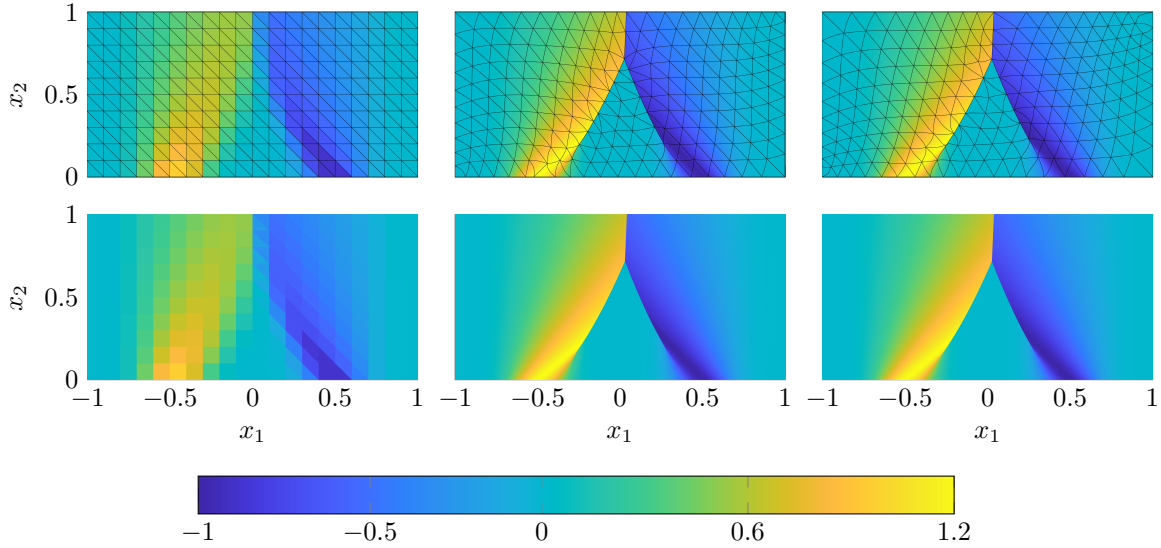


Figure 21: Starting point (left) and HOIST solution for polynomial degrees $p = 2$ (middle) and $p = 3$ (right) for the **iburg-form** test case, with (top row) and without (bottom row) the mesh edges.

6.3. Inviscid, compressible flow through area variation

Next, we consider inviscid, compressible flow through an area variation (test case: **nozzle**) governed by the quasi-one-dimensional Euler equations

$$\begin{aligned} \frac{\partial}{\partial x} (A(x)\rho(x)v(x)) &= 0 \\ \frac{\partial}{\partial x} (A(x) [\rho(x)v(x)^2 + P(x)]) &= P(x) \frac{\partial A}{\partial x}(x) \\ \frac{\partial}{\partial x} (A(x) [\rho(x)E(x) + P(x)] v(x)) &= 0, \end{aligned} \tag{83}$$

for $x \in \Omega \subset (0, 10)$, where $\rho : \Omega \rightarrow \mathbb{R}_{>0}$ is the density of the fluid, $v : \Omega \rightarrow \mathbb{R}$ is the velocity of the fluid, and $E : \Omega \rightarrow \mathbb{R}_{>0}$ is the total energy of the fluid, implicitly defined as the solution of (83). For a calorically ideal fluid, the pressure of the fluid, $P : \Omega \rightarrow \mathbb{R}_{>0}$, is related to the energy via the ideal gas law

$$P = (\gamma - 1) (\rho E - \rho v^2/2), \tag{84}$$

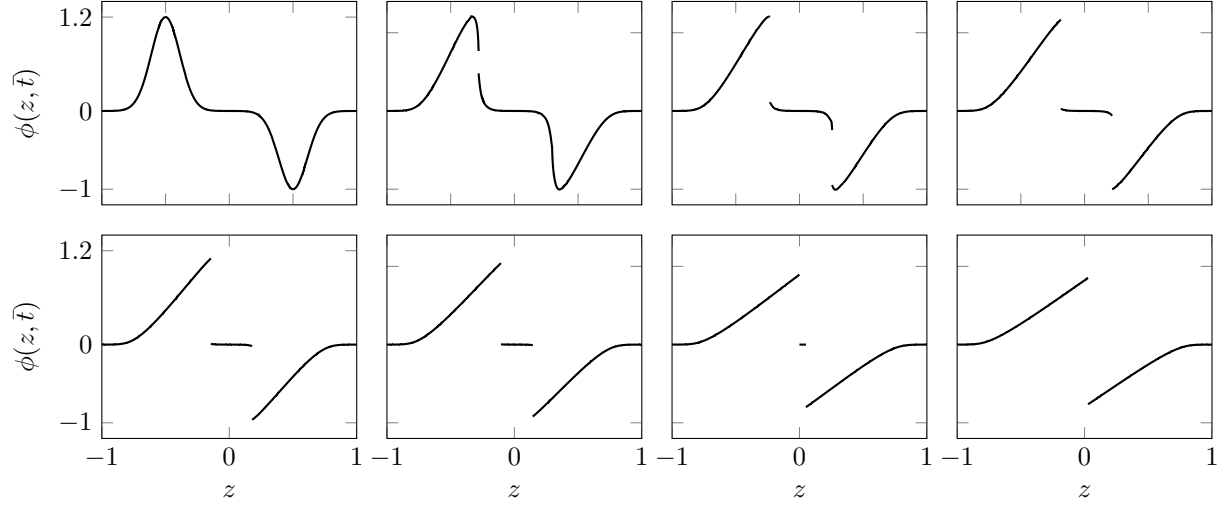


Figure 22: Temporal slices of the $p = 3$ HOIST solution for the **iburg-form** test case at time instances $\bar{t} = 0, 0.146, 0.218, 0.364, 0.436, 0.655, 0.727$ (left-to-right, top-to-bottom). The time instances are not uniformly spaced to show relevant features of solution.

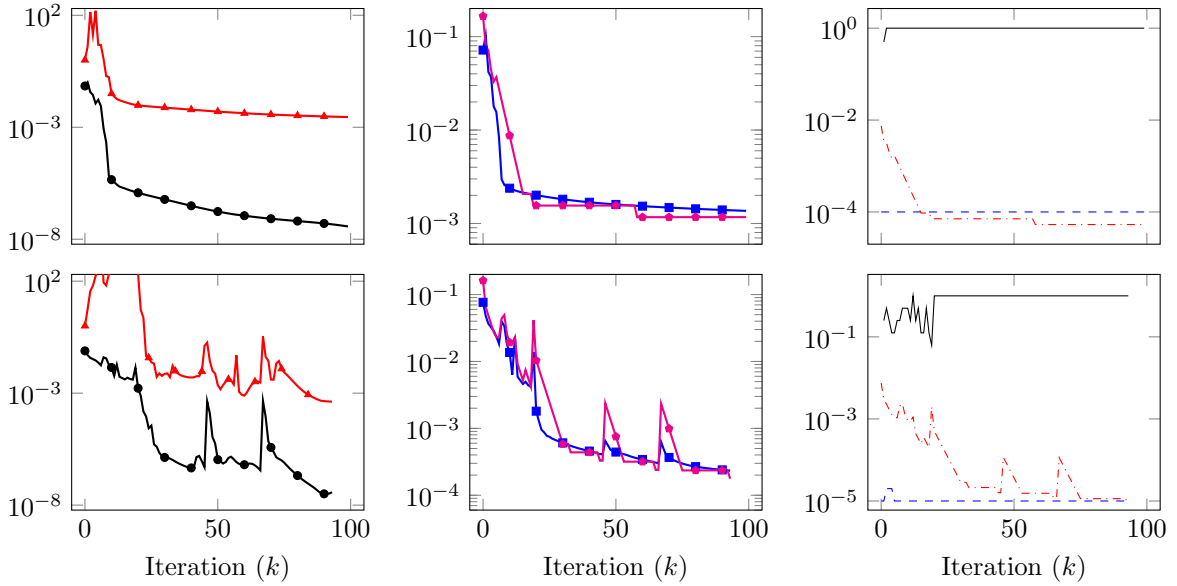


Figure 23: SQP convergence history and behavior of adaptive parameters for the **iburg-form** test case (legend in Table 1) for $p = 2$ (top) and $p = 3$ (bottom).

where $\gamma \in \mathbb{R}_{>0}$ is the ratio of specific heats. The area beneath the nozzle is given by $A : \Omega \rightarrow \mathbb{R}$, which we take to be

$$A : x \mapsto \mu_1 + (\mu_2 - \mu_1) \frac{(10 - x)x}{25}, \quad (85)$$

which has an exit and throat area of μ_1 and μ_2 , respectively, with the throat located midway through the domain ($x = 5$); in this work, we take $\mu_1 = 3$, $\mu_2 = 1$. The boundary conditions are $\rho(0) = 1$ and $\rho(10) = 0.7$, which will lead to a shock at $x_s = 7.94$. By combining the area, density, momentum, and energy into a vector of conservative variables $U : \Omega \rightarrow \mathbb{R}^3$, defined as

$$U : x \mapsto \begin{bmatrix} A(x)\rho(x) \\ A(x)\rho(x)v(x) \\ A(x)\rho(x)E(x) \end{bmatrix}, \quad (86)$$

the quasi-one-dimensional Euler equations in (83) are a conservation law of the form (1). For the DG discretization, we use a smoothed variant of Roe's flux described in [47] with Harten-Hyman entropy fix [20] as the inviscid numerical flux function. The purpose of this numerical experiment is to verify optimal convergence rate of the HOIST method for a compressible flow and provide a direct comparison to popular shock capturing methods based on artificial viscosity.

We discretize the one-dimensional domain with 12 elements of degree $q = 1$ (no benefit to using high-order geometry approximation in one dimension) and use the HOIST method with polynomial degrees $p = 1, \dots, 5$ (HOIST parameters in Table A.4, except $c_8 = 10^{-1}$ in the case $p = 1$). The $p = 2$ HOIST solution on this coarse discretization (12 elements) provides an excellent approximation that is indistinguishable from the exact solution to (83). The shock capturing method based on artificial viscosity in [33] requires 50 elements with a $p = 4$ approximation to achieve a similar solution, although the discontinuity is approximated by a steep gradient, which is a noticeable deviation from the exact solution (Figure 24). Due to the geometric simplicity in the one-dimensional setting, the HOIST solvers converge rapidly, achieving tight tolerances on the optimality system in only 20 iterations (Figure 25).

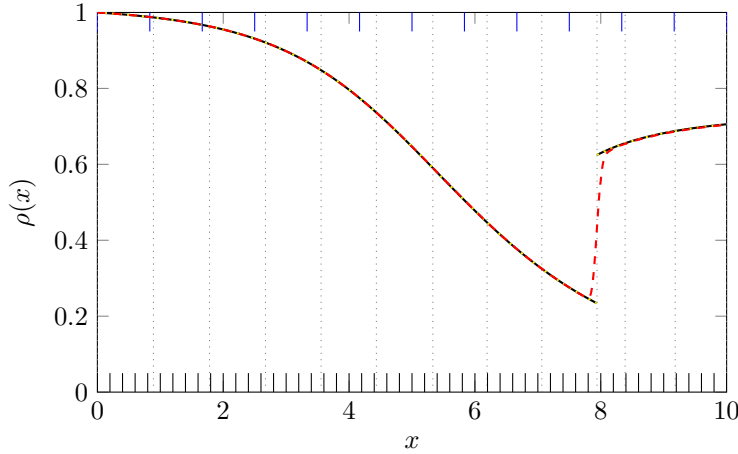


Figure 24: The solution (density) of the `nozzle` test case (—) and the corresponding HOIST (·····) and shock capturing (---) approximations. The HOIST simulation uses 12 quadratic elements; the element boundaries of the initial (—) and final (·····) mesh are included to show the initial mesh is far from alignment with the discontinuity. The shock capturing simulation uses 50 quartic elements with the element boundaries indicated with (—).

Finally, we study the h -convergence of the HOIST method for this problem and compare to the shock capturing method in [33]. We consider two error metrics: $E_\rho : \mathbb{R}^{N_u} \times \mathbb{R}^{N_x} \rightarrow \mathbb{R}$, the L^1 error in the density, and $E_{x_s} : \mathbb{R}^{N_x} \rightarrow \mathbb{R}$, the error in the shock position, which are defined as

$$E_\rho : (\mathbf{u}, \mathbf{x}) \mapsto \int_0^{10} |\rho(x) - \hat{\rho}(x; \mathbf{u}, \mathbf{x})| dx, \quad E_{x_s} : \mathbf{x} \mapsto |x_s - \hat{x}_s(\mathbf{x})|, \quad (87)$$

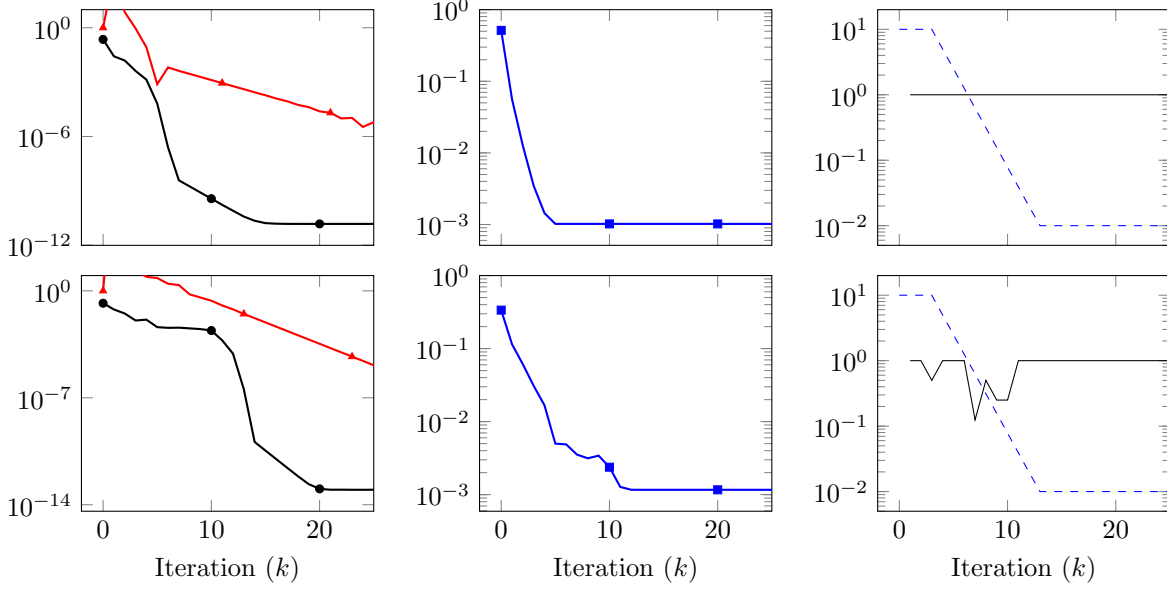


Figure 25: SQP convergence history and behavior of adaptive parameters for **nozzle** test case (legend in Table 1). Only the $p = 3$ (top) and $p = 5$ (bottom) simulations are included for brevity. The mesh quality term is not used for one-dimensional problems and not included in the convergence plots.

where $\hat{\rho} : \Omega \times \mathbb{R}^{N_u} \times \mathbb{R}^{N_x} \rightarrow \mathbb{R}$ and $\hat{x}_s : \mathbb{R}^{N_x} \rightarrow \mathbb{R}$ are the HOIST approximations to ρ and the shock position, respectively. Because the shock position is not well-defined for the shock capturing method, we only consider its E_ρ error. We consider polynomial degrees $p = 1, \dots, 5$ with at least four levels of uniform refinement (up to seven levels for the lower polynomial degrees). The HOIST method achieves optimal convergence rates, $\mathcal{O}(h^{p+1})$, for all polynomial degrees considered for both error metrics, while the shock capturing method is limited to sub-first-order convergence rate (Figure 26, Table 3). The slow convergence rate of the shock capturing method is due to the smooth approximation to the discontinuity and downstream corruption [27, 5].

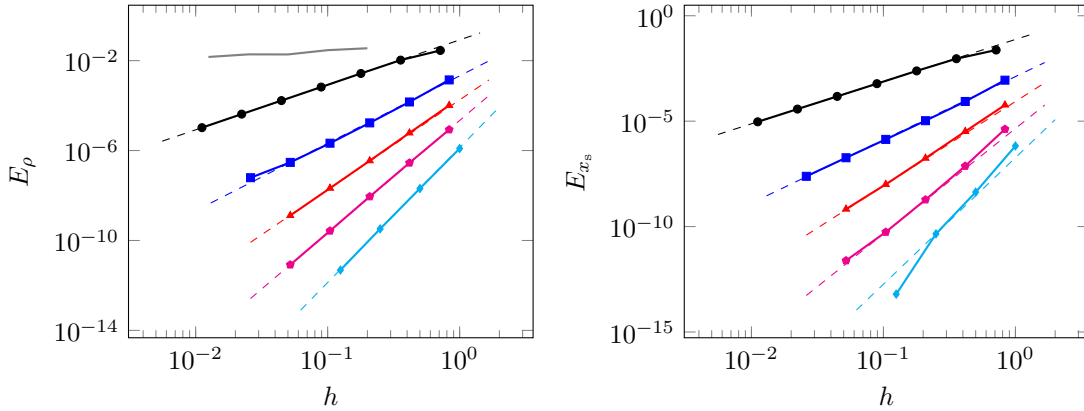


Figure 26: h -convergence of the HOIST method for the **nozzle** test case for both error metrics, E_ρ (left) and E_{x_s} (right), for polynomial degrees $p = 1$ (—●—), $p = 2$ (—■—), $p = 3$ (—▲—), $p = 4$ (—◆—), and $p = 5$ (—★—), as well as the shock capturing method of [33] for polynomial degree $p = 2$ (—). The dashed lines indicate the optimal convergence rate $(p + 1)$.

Table 3: Tabulated convergence results for the **nozzle** test case in Figure 26. The segment-wise slope of the curves ($m(\cdot)$) tends to at least the optimal rate ($p + 1$) as the mesh is refined.

p	q	$ \mathcal{E}_h $	h	E_ρ	$m(E_\rho)$	E_{x_s}	$m(E_{x_s})$
1	1	112	8.93e-02	6.68e-04	-	6.00e-04	-
1	1	224	4.46e-02	1.67e-04	2.00	1.49e-04	2.01
1	1	448	2.23e-02	4.18e-05	2.00	3.74e-05	2.00
1	1	896	1.12e-02	1.04e-05	2.00	9.31e-06	2.00
2	2	48	2.08e-01	1.70e-05	-	1.05e-05	-
2	2	96	1.04e-01	2.13e-06	3.00	1.37e-06	2.94
2	2	192	5.21e-02	2.97e-07	2.84	1.84e-07	2.90
2	2	384	2.60e-02	6.19e-08	2.26	2.42e-08	2.92
3	3	24	4.17e-01	6.09e-06	-	3.25e-06	-
3	3	48	2.08e-01	3.53e-07	4.11	1.75e-07	4.21
3	3	96	1.04e-01	2.11e-08	4.06	1.00e-08	4.13
3	3	192	5.21e-02	1.29e-09	4.03	6.72e-10	3.90
4	4	24	4.17e-01	2.83e-07	-	7.41e-08	-
4	4	48	2.08e-01	8.95e-09	4.98	1.88e-09	5.30
4	4	96	1.04e-01	2.67e-10	5.07	5.50e-11	5.10
4	4	192	5.21e-02	8.28e-12	5.01	2.44e-12	4.50
5	5	10	1.00e+00	1.23e-06	-	6.68e-07	-
5	5	20	5.00e-01	2.04e-08	5.92	4.31e-09	7.28
5	5	40	2.50e-01	3.29e-10	5.96	4.50e-11	6.58
5	5	80	1.25e-01	4.82e-12	6.09	6.22e-14	9.50

6.4. Inviscid, compressible flow

Finally, we consider flow of an inviscid, compressible fluid through a domain $\bar{\Omega} \subset \mathbb{R}^d$, which are governed by the Euler equations

$$\begin{aligned}
\frac{\partial}{\partial t} \rho(z, t) + \frac{\partial}{\partial z_j} (\rho(z, t) v_j(z, t)) &= 0 \\
\frac{\partial}{\partial t} (\rho(z, t) v_i(z, t)) + \frac{\partial}{\partial z_j} (\rho(z, t) v_i(z, t) v_j(z, t) + P(z, t) \delta_{ij}) &= 0 \\
\frac{\partial}{\partial t} (\rho(z, t) E(z, t)) + \frac{\partial}{\partial z_j} ([\rho(z, t) E(z, t) + P(z, t)] v_j(z, t)) &= 0
\end{aligned} \tag{88}$$

for all $z \in \bar{\Omega}$ (spatial domain) and $t \in \mathcal{T} \subset \mathbb{R}$ (temporal domain), where $i = 1, \dots, d$ and summation is implied over the repeated index $j = 1, \dots, d$. The density of the fluid $\rho : \bar{\Omega} \times \mathcal{T} \rightarrow \mathbb{R}_{>0}$, the velocity of the fluid $v_i : \bar{\Omega} \times \mathcal{T} \rightarrow \mathbb{R}$ in the z_i direction for $i = 1, \dots, d$, and the total energy of the fluid $E : \bar{\Omega} \times \mathcal{T} \rightarrow \mathbb{R}_{>0}$ are implicitly defined as the solution of (88). For a calorically ideal fluid, the pressure of the fluid, $P : \bar{\Omega} \times \mathcal{T} \rightarrow \mathbb{R}_{>0}$, is related to the energy via the ideal gas law

$$P = (\gamma - 1) \left(\rho E - \frac{\rho v_i v_i}{2} \right), \tag{89}$$

where $\gamma \in \mathbb{R}_{>0}$ is the ratio of specific heats. This leads to a conservation law of the form (1) over the space-time domain $\Omega := \bar{\Omega} \times \mathcal{T} \subset \mathbb{R}^{d+1}$ by combining the density, momentum, and energy into a vector of conservative variables $U : \Omega \rightarrow \mathbb{R}^{d+2}$, defined as

$$U : x \mapsto \begin{bmatrix} \rho((x_1, \dots, x_d), x_{d+1}) \\ \rho((x_1, \dots, x_d), x_{d+1}) v((x_1, \dots, x_d), x_{d+1}) \\ \rho((x_1, \dots, x_d), x_{d+1}) E((x_1, \dots, x_d), x_{d+1}) \end{bmatrix}. \tag{90}$$

For the DG discretization, we use a smoothed variant of Roe's flux described in [47] with Harten-Hyman entropy fix [20] as the inviscid numerical flux function. For steady problems, the temporal domain is

empty ($\mathcal{T} = \emptyset$), all variables are independent of time, the space-time and spatial domains are the same d -dimensional set ($\Omega = \bar{\Omega}$), and the vector of conservative variables is

$$U : x \mapsto \begin{bmatrix} \rho(x) \\ \rho(x)v(x) \\ \rho(x)E(x) \end{bmatrix}. \quad (91)$$

6.4.1. Sod's shock tube

Sod's shock tube (test case: **sod**) is a Riemann problem for the Euler equations that models an idealized shock tube where the membrane separating a high pressure region from a low pressure one is instantaneously removed. This is a commonly used validation problem since it has an analytical solution that features a shock wave, rarefaction wave, and contact discontinuity. The flow domain is $\bar{\Omega} = (0, 1)$, the time domain is $\mathcal{T} = (0, 0.2)$, the initial condition is given in terms of the density, velocity, and pressure as

$$\rho(z, 0) = \begin{cases} 1 & z < 0.5 \\ 0.125 & z \geq 0.5 \end{cases}, \quad v(z, 0) = 0, \quad P(z, 0) = \begin{cases} 1 & z < 0.5 \\ 0.1 & z \geq 0.5, \end{cases} \quad (92)$$

and the density, velocity, and pressure are prescribed at $z = 0$ and the velocity is prescribed at $z = 1$ (values can be read from the initial condition). The solution of this problem contains three waves (shock, contact, rarefaction) that emanate from $z = 0.5$ and move at different speeds, which is a generalized triple point in space-time. The purpose of this numerical experiment is to demonstrate the HOIST method is able to track various types of features that are discontinuous (shocks and contacts) or non-smooth (head and tail of rarefactions) and locate triple points without seeding with *a priori* information.

All of the discontinuity surfaces in this problem are straight-sided so we choose to approximate the geometry using straight-sided elements ($q = 1$) and approximate the conservative variables using $p = 2$ elements. We discretize the domain using an unstructured mesh of 108 triangular elements, generated using DistMesh [34], with a refinement region at the point $x = (0.5, 0)$ from which the waves originate because it separates the flow into multiple regions. Furthermore, we place a node at $x = (0.5, 0)$ and fix it throughout the HOIST iterations to ensure the discontinuity in the boundary condition is accurately integrated in the weak formulation of the conservation law. Using this unstructured mesh and the corresponding first-order finite volume solution to initialize the HOIST method (parameters in Table A.4), it converges to a mesh that tracks the shock, contact discontinuity, and the head and tail of the rarefaction (Figure 27), which leads to an accurate approximation to the exact solution (Figure 28) on a space-time mesh with only 84 elements (24 elements removed during the solution procedure). This shows the error-based HOIST indicator successfully tracks both discontinuous features and continuous features with discontinuous derivatives. The SQP solver tracks the features individually based on their relative strength, i.e., discontinuities are tracked first based on the magnitude of their jump and then non-smooth features are tracked based on the magnitude of the derivative jump. The strongest feature, the shock, is tracked by the mesh first (around iteration 27), next the contact discontinuity is tracked (around iteration 52), then the head of the rarefaction is tracked (around iteration 66), and the tail of the rarefaction, the weakest feature, is tracked (around iteration 106) (Figure 29).

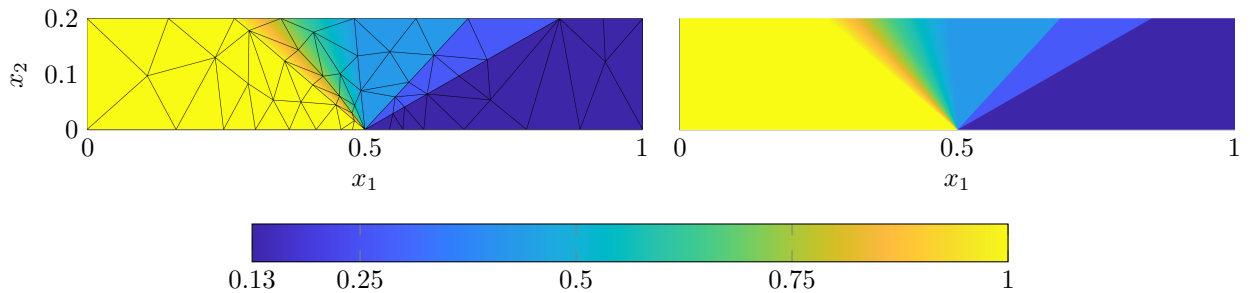


Figure 27: HOIST solution to the **sod** test case with (*left*) and without (*right*) mesh. All non-smooth features (shock, contact, head and tail of rarefaction) are tracked by the mesh, which leads to a well-resolved solution on the coarse mesh.

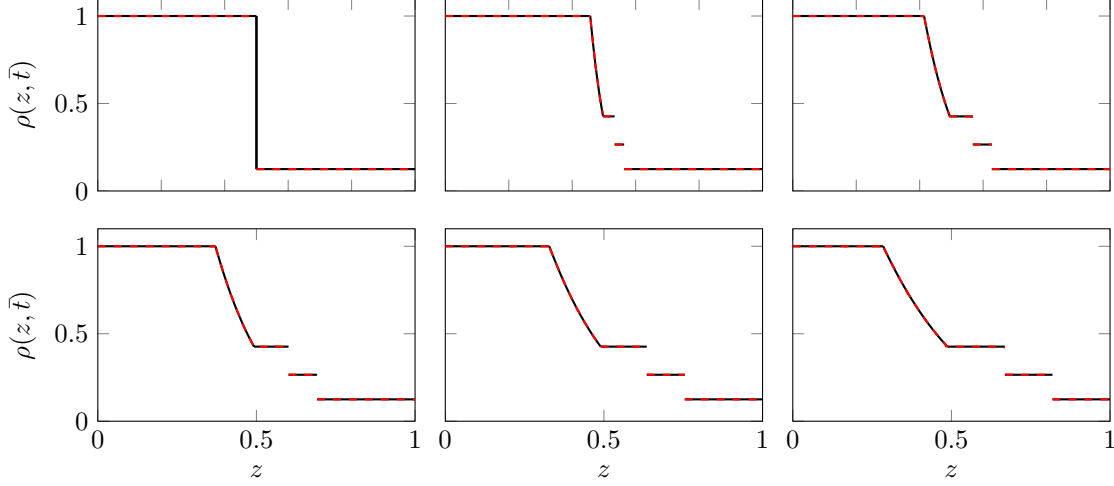


Figure 28: Temporal slices of the analytical solution (—) and HOIST approximation (---) to the `sod` test case at time instances $\bar{t} = 0, 0.0364, 0.0727, 0.109, 0.146, 0.182$ (left-to-right, top-to-bottom).

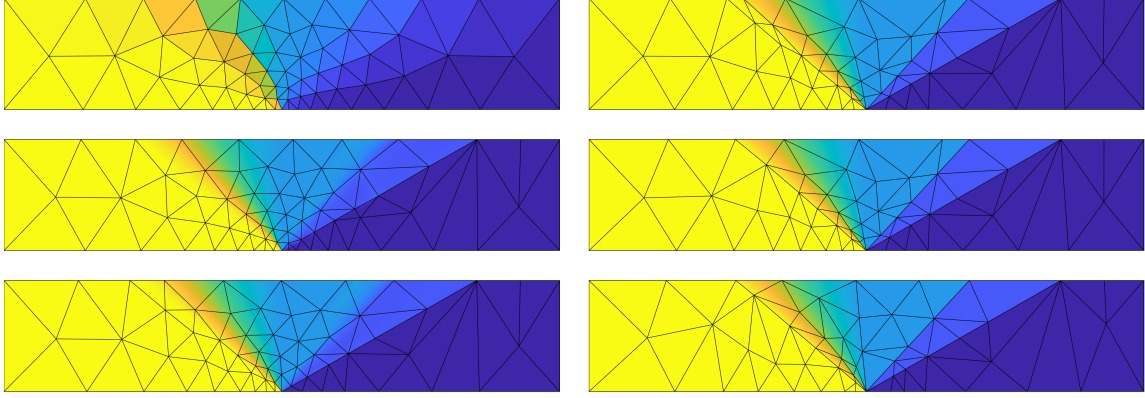


Figure 29: Selected HOIST iterations for `sod` test case at iterations $k = 0, 10, 27, 52, 66, 106$ (top-to-bottom, left-to-right). The SQP solver tracks the non-smooth features in order based on the strength of the feature (strongest to weakest): shock, contact discontinuity, head of rarefaction, and tail of rarefaction. Colorbar in Figure 27.

6.4.2. Supersonic flow over two-dimensional diamond in tunnel

Next, we consider steady, supersonic (Mach 2) flow through a two-dimensional diamond in a tunnel (Figure 30; test case: `diamond`) that features reflecting, intersecting, and curved shocks to demonstrate the HOIST method can accurately track these features with a high-order mesh and resolve the corresponding flow features.

We discretize the domain using an unstructured triangular mesh, generated using DistMesh [34], consisting of 220 elements and use a third-order approximation for the geometry and flow variables ($p = q = 2$). Using this unstructured mesh and the corresponding first-order finite volume solution to initialize the HOIST method (parameters in Table A.4), it converges to a mesh that tracks all shocks and their intersections with the final mesh containing 201 elements (19 elements removed during the solution procedure). The coarse, high-order (curved) elements conform to the curvature of the discontinuity surfaces and the four generalized triple points are tracked (Figure 31). A shock capturing method would require refined elements in the vicinity of all discontinuity surfaces, particularly the triple points, which would lead to a mesh with many more elements.

Remark 23. *There should be a slip line (a line along which there is a weak discontinuity in the density, but the pressure and velocity direction are continuous) emerging from the triple point near the trailing edge*

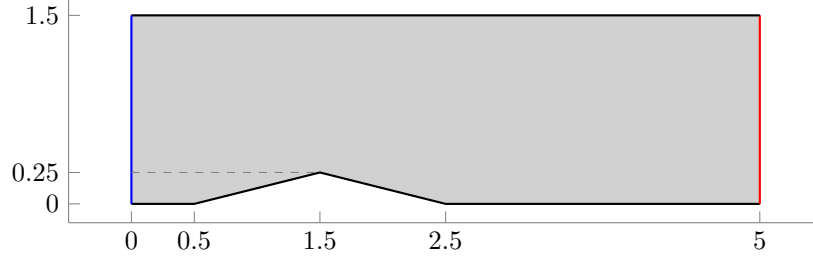


Figure 30: Geometry and boundary conditions for the **diamond** test case. Boundary conditions: slip walls (—), Mach 2 supersonic inflow (—), and supersonic outflow (—).

of the diamond (at $x = (3.16, 0.26)$) that is not resolved or tracked because the mesh in that region is too coarse. As the mesh is refined, the HOIST method will track all slip lines; we defer a refinement study to the scramjet example in Section 6.4.3.

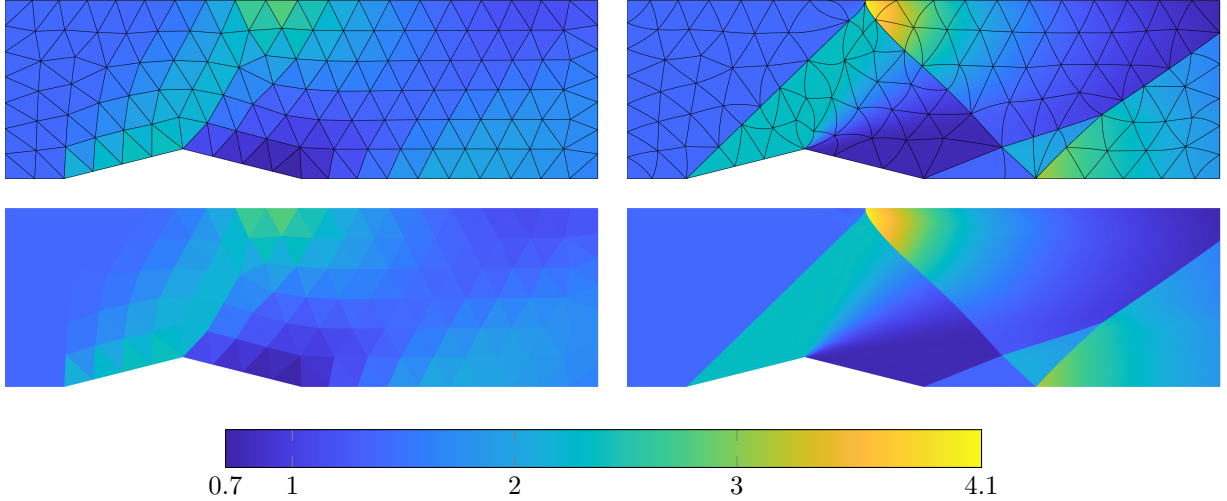


Figure 31: Starting point (left) and HOIST solution (right) for the **diamond** test case with (top) and without (bottom) mesh edges. The high-order mesh tracks the curved shocks, shock-shock interactions, and shock reflections and the solution is well-resolved throughout the domain.

6.4.3. Hypersonic flow through two-dimensional scramjet

Next, we consider steady, hypersonic (Mach 5) flow through a two-dimensional scramjet (Figure 32; test case: **scramjet**); it possesses similar features to the diamond case (Section 6.4.3) with more complex discontinuity surfaces. We discretize the domain using two unstructured triangular meshes, generated using DistMesh [34], consisting of 1442 and 2679 elements and use a third-order approximation for the geometry and flow variables ($p = q = 2$). Using these unstructured meshes and the corresponding first-order finite volume solution to initialize the HOIST method (parameters in Table A.4), it converges to a mesh that tracks all shocks and their intersections with the final meshes containing 1299 and 2523 elements (143 and 156 elements removed during the solution procedure), respectively. The high-order (curved) elements conform to the curvature of the discontinuity surfaces and the various triple points and reflection points are tracked (Figure 33-34). Both the coarse and fine mesh lead to highly accurate solution as seen from the flow field without the mesh edges; the main difference between the two simulations is that the fine mesh is able to completely track all discontinuities emanating from the corner at $x = (w_5, h_2)$ (Figure 34), including the slip line that is only partially tracked on the coarse mesh (Figure 33).

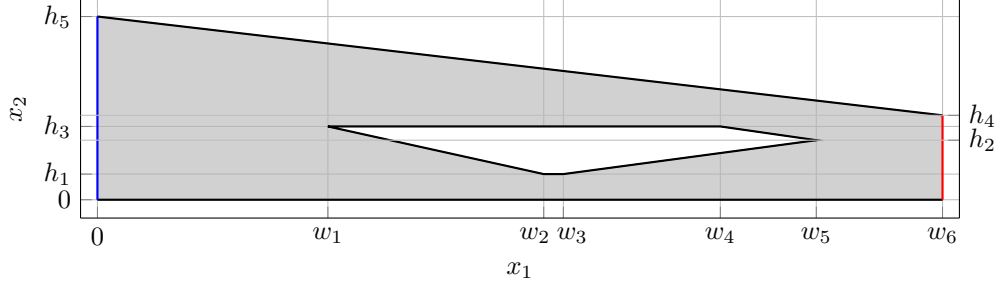


Figure 32: Geometry and boundary conditions for the **scramjet** test case. Geometry: $w_1 = 1.088$, $w_2 = 2.1071$, $w_3 = 2.1998$, $w_4 = 2.9410$, $w_5 = 3.3940$, $w_6 = 3.9899$, $h_1 = 0.1211$, $h_2 = 0.2811$, $h_3 = 0.3460$, $h_4 = 0.3986$, $h_5 = 0.8650$. Boundary conditions: slip walls (—), Mach 5 supersonic inflow (—), and supersonic outflow (—).

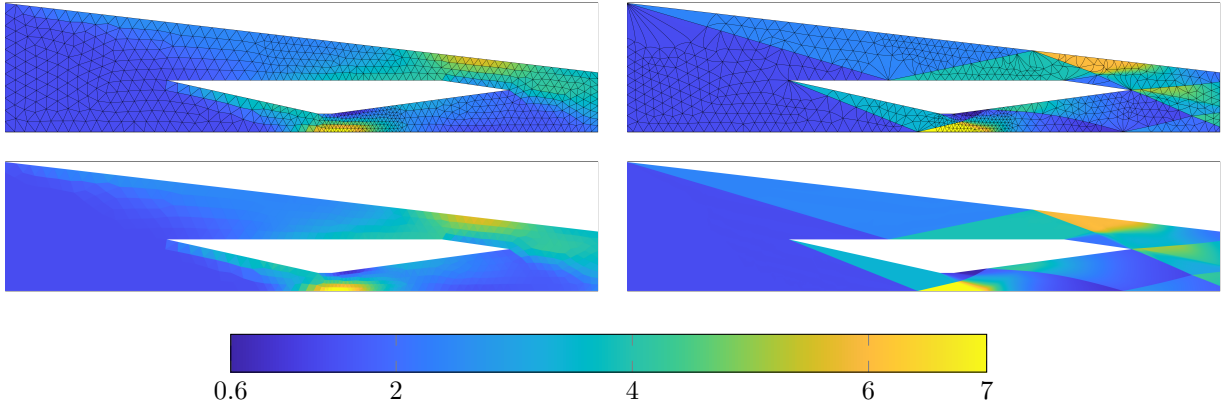


Figure 33: Starting point (*left*) and HOIST solution (*right*) for the **scramjet** test case on the coarse mesh with (*top*) and without (*bottom*) mesh edges. The high-order mesh tracks the curved shocks, shock-shock interactions, and shock reflections (except the discontinuity emanating from $x = (w_5, h_2)$) and the solution is well-resolved throughout the domain.

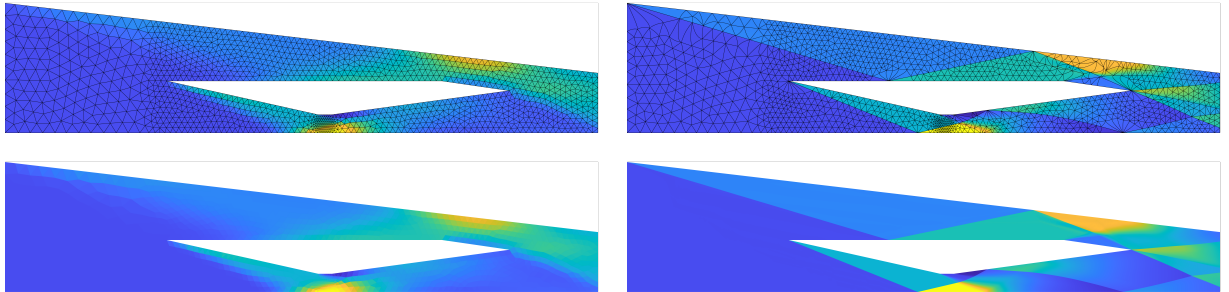


Figure 34: Starting point (*left*) and HOIST solution (*right*) for the **scramjet** test case on the fine mesh with (*top*) and without (*bottom*) mesh edges. The high-order mesh tracks the curved shocks, shock-shock interactions, and shock reflections (including the discontinuity emanating from $x = (w_5, h_2)$) and the solution is well-resolved throughout the domain. Colorbar in Figure 33.

6.4.4. Supersonic flow over sphere

Finally, we consider steady, supersonic (Mach 2) flow over a sphere (test case: **sphere**) that features a bow shock to demonstrate the HOIST method reliably tracks curved shocks in three-dimensional compressible flows with a coarse, high-order mesh. To reduce the computational cost, we model only a portion of the geometry and use symmetry boundary conditions (Figure 35). We discretize the domain using a high-order unstructured, tetrahedra mesh consisting of 511 elements and use a third-order approximation for the geometry and flow variables ($p = q = 2$). A straight-sided mesh is generated using DistMesh [34] then high-order nodes of element faces that lie on the sphere are projected onto the curved boundary. Since this problem contains a bow shock that does not intersect the sphere, we choose to fix the nodes on the sphere surface (rather than allow them to slide along the sphere). Using this unstructured mesh and the corresponding first-order finite volume solution to initialize the HOIST method (parameters in Table A.4), it converges to a mesh that tracks the bow shock and a high-quality flow solution (Figure 36); the final mesh contains 491 elements (20 elements removed during the solution procedure). The high-order elements conform to the curvature of the bow shock and the high-order approximation of the flow field leads to a highly accurate approximation on an extremely coarse mesh. The analytical stagnation pressure (at $x = (-1, 0, 0)$) for this flow configuration is 5.6404 (non-dimensional) and the corresponding quantity computed from the HOIST simulation is 5.6465, a relative error of 0.11%. Because the mesh conforms to the bow shock, an accurate representation of the shock layer (region between bow shock and sphere surface) and shock surface are directly available (Figure 37).

Remark 24. The HOIST parameters used for this simulation are mostly consistent with those used in previous sections. The main difference is the reference elements are used as the ideal elements ($K_{\star,e} = \Omega_{0,e}$), which is related to our choice to fix nodes along the sphere. Tests with our standard approach that takes $K_{\star,e} = K_{\star}$ (equilateral tetrahedra) indicated numerous element collapses occur near the surface of the sphere as elements in that region are driven toward equilateral tetrahedra, which can cause the HOIST simulation to fail.

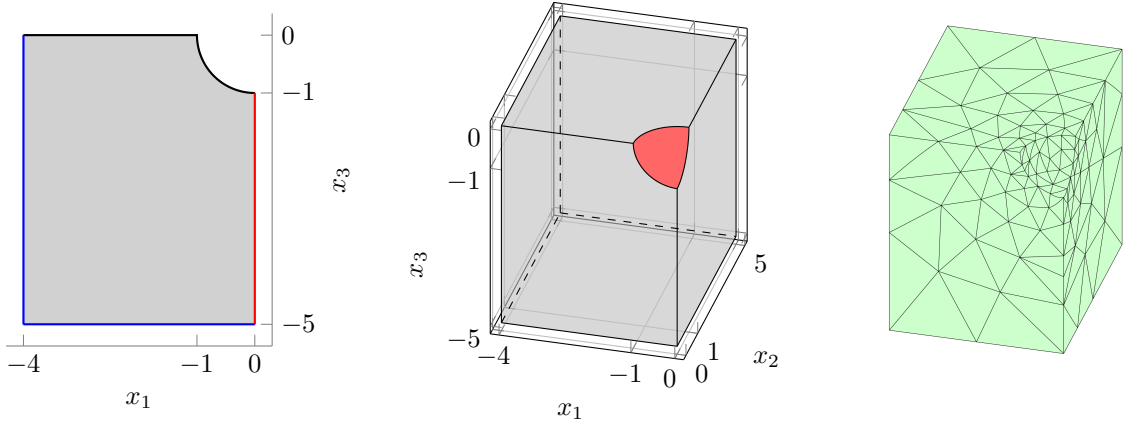


Figure 35: Geometry of the **sphere** test case including a slice along the $x_2 = 0$ plane (*left*) and a three-dimensional view (*middle*) and the unstructured, high-order mesh with 511 quadratic tetrahedral elements (*right*) used to initialize the HOIST simulation. Boundary conditions are indicated in the left figure: slip walls (—), Mach 2 supersonic inflow (—), and supersonic outflow (—); the $x_2 = 0$ plane uses slip wall, and the $x_2 = 5$ plane uses supersonic inflow condition.

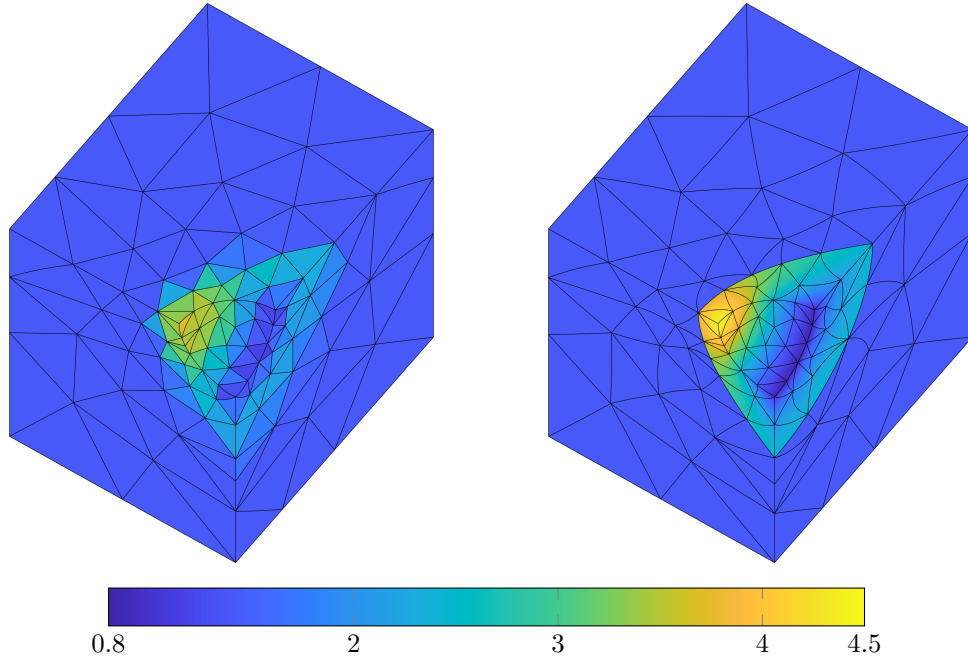


Figure 36: Starting point (*left*) and HOIST solution (*right*) for the **sphere** test case (colored by density). The high-order, high-quality tetrahedral elements track the curved bow shock and the solution is well-resolved throughout the domain.

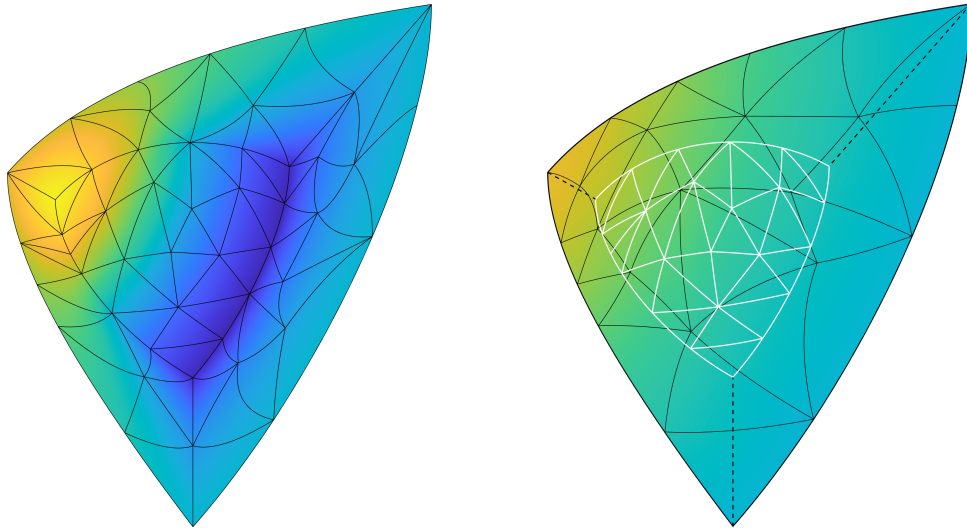


Figure 37: The HOIST approximation to the shock layer (*left*) and the surface of the bow shock (*right*; surface mesh of the sphere included in white for reference) for the **sphere** test case (colored by density); the latter is produced by extracting the high-order surface triangles of the shock-aligned mesh. Both the shock layer and shock surface are represented to high accuracy on the extremely coarse mesh due to optimal, automated alignment of the high-order mesh with the bow shock. Colorbar in Figure 36.

7. Conclusion

The HOIST method is a high-order numerical method that approximates solutions of conservation laws using a high-order DG discretization on a mesh whose elements are aligned with non-smooth features in the flow. This allows the non-smooth features to be represented by the inter-element jumps in the DG solution and high-order basis functions approximate smooth regions of the flow, which eliminates the need for nonlinear stabilization. As a result, the method produces highly accurate solutions on coarse meshes and recovers optimal convergence rates of the DG discretization even for flows with non-smooth features. While these advantages are shared by explicit shock tracking approaches [31, 37], HOIST [45, 48, 47] and other implicit shock tracking methods (e.g., MDG-ICE [10, 24, 25]) provide several additional benefits: formulated for a general, nonlinear conservation law (not tailored to a specific set of equations) and the formulation is well-suited for problems with intricate discontinuity surfaces (curved and reflecting shocks, shock formation, shock-shock interaction). The latter is due to the geometrically complex problem of generating a feature-aligned mesh being re-cast to solving an optimization problem over the discrete DG solution and nodal coordinates of the mesh.

In this work, we introduced an improved solver for the implicit shock tracking optimization problem based on the SQP solver originally developed in [48]. The new solver features a new merit function penalty parameter (Section 5.1.1), an adaptive mesh penalty parameter in the objective function (Section 5.1.3), and, most importantly, a number of practical robustness measures (Section 5.2). The most critical robustness measures are 1) dimension- and order-independent simplex element collapses that are boundary-preserving and shock-aware and 2) element-wise solution re-initialization that resets the flow solution in oscillatory elements to a constant value. In addition to the solver developments, we also introduced a general, automated procedure to parametrize the mesh motion (i.e., nodal coordinates) that guarantees all planar boundaries will be preserved throughout the implicit tracking iterations. These advances to the HOIST method were critical to enable robust convergence for two- and three-dimensional flows with complex shock surfaces and they eliminated the need for continuation in the polynomial degree. A series of nine numerical experiments demonstrated the robustness of the solver even for two- and three-dimensional flows with complex shock surfaces, the meshes produced are high-quality and track non-smooth features in the flow (shocks, contacts, rarefactions), and the method achieves the optimal convergence rate of the DG method even for flows with non-smooth features. In particular, the diamond and scramjet problems demonstrated the method can track curved, reflecting, and interacting shocks, which leads to a highly accurate solution on coarse meshes, even in the hypersonic flow regime. The sphere problem demonstrated the robustness and generality of the method for three-dimensional, compressible flows.

Additional research is required to develop iterative solvers and preconditioners for the SQP linear system in (43) to make the approach practical for large-scale problems. Furthermore, development of a general, automated approach to construct boundary-preserving parametrizations for curved boundaries is needed for the method to be useful for complex, three-dimensional geometries. Other interesting avenues of future research include extension of the method to viscous conservation laws, investigation into slab-based space-time approaches to handle complex unsteady flows, and using the method to study relevant hypersonic flows.

Appendix A. Parameters used for numerical experiments

The HOIST parameters used for the numerical experiments are included in Table A.4. The only problems we choose to straighten re-initialized elements (Remark 19) are Burgers' equation with shock formation (**iburg-form**), the diamond (**diamond**), the scramjet (**scramjet**), and the sphere (**sphere**).

Table A.4: HOIST parameters used for numerical experiments

	$K_{*,e}$	$(\gamma_0, \gamma_{\min}, \tau, \sigma_1, \sigma_2)$	$(\kappa_0, \kappa_{\min}, \nu, \xi)$	$(c_1, c_2, c_3, c_4, c'_4)$	(c_5, c_6, c_7, c_8)
advec-planar	K_*	$(10^{-2}, 10^{-6}, 2, 10^{-2}, 10^{-1})$	$(10^{-10}, 10^{-10}, -, -)$	$(0.2, 10^{-10}, 0.2, 0, -)$	-
advec-trig	K_*	$(10^{-2}, 10^{-6}, 2, 10^{-2}, 10^{-1})$	$(10^{-10}, 10^{-10}, -, -)$	$(0.2, 10^{-10}, 0.2, 0, 0.05)$	-
iburg-acc	K_*	$(10^{-2}, 10^{-2}, 2, 10^{-2}, 10^{-1})$	$(10^{-2}, 10^{-10}, 0.75, 1)$	$(0.2, 10^{-10}, 0.2, 0, 0.05)$	$(10^{-1}, 10^{-2}, 1, 10^{-2})$
iburg-form	K_*	$(10^{-4}, 10^{-4}, 2, 10^{-2}, 10^{-1})$	$(10^{-2}, 10^{-10}, 0.75, 1)$	$(0.2, 10^{-10}, 0.33, 0, 0.01)$	$(10^{-1}, 10^{-2}, 0.2, 10^{-6})$
nozzle	-	$(10, 10^{-2}, 2, 10^{-2}, 10^{-1})$	-	$(0.2, 10^{-10}, 0.2, 0, 0.05)$	$(10^{-2}, 10^{-2}, 0.25, 10^{-6})$
sod	K_*	$(10^{-5}, 10^{-8}, 1.2, 10^{-2}, 10^{-1})$	$(10^{-6}, 10^{-10}, 0.75, 2)$	$(0.15, 10^{-10}, 0.2, 0.05, 0.05)$	$(10^{-2}, 10^{-2}, 0, 10^{-6})$
diamond	K_*	$(1, 10^{-2}, 1.2, 10^{-2}, 10^{-1})$	$(10^{-3}, 10^{-8}, 0.5, 0.5)$	$(0.25, 10^{-10}, 0.25, 10^{-3}, 0)$	$(10^{-2}, 10^{-2}, 0.5, 10^{-4})$
scramjet	K_*	$(1, 10^{-2}, 1.1, 10^{-2}, 10^{-1})$	$(1, 10^{-2}, 0.8, 1)$	$(0.2, 10^{-10}, 0.05, 10^{-3}, 10^{-4})$	$(10^{-3}, 10^{-1}, 0.2, 10^{-2})$
sphere	$\Omega_{0,e}$	$(10^{-3}, 10^{-3}, 1.5, 10^{-2}, 10^{-1})$	$(10^{-1}, 10^{-4}, 0.5, 1)$	$(0.2, 10^{-10}, 0.2, 10^{-3}, 10^{-4})$	$(10^{-2}, 10^{-1}, 1, 10^{-2})$

Acknowledgments

This material is based upon work supported by the Air Force Office of Scientific Research (AFOSR) under award numbers FA9550-20-1-0236, FA9550-22-1-0002, FA9550-22-1-0004. The content of this publication does not necessarily reflect the position or policy of any of these supporters, and no official endorsement should be inferred.

References

- [1] M. J. Baines, S. J. Leary, and M. E. Hubbard. Multidimensional least squares fluctuation distribution schemes with adaptive mesh movement for steady hyperbolic equations. *SIAM Journal on Scientific Computing*, 23(5):1485–1502, 2002.
- [2] Garrett E. Barter and David L. Darmofal. Shock capturing with PDE-based artificial viscosity for DGFEM: Part I. Formulation. *Journal of Computational Physics*, 229(5):1810–1827, March 2010.
- [3] J. B. Bell, G. R. Shubin, and J. M. Solomon. Fully implicit shock tracking. *Journal of Computational Physics*, 48(2):223–245, 1982.
- [4] A. Bonfiglioli, R. Paciorri, and L. Campoli. Unsteady shock-fitting for unstructured grids. *International Journal for Numerical Methods in Fluids*, 81(4):245–261, 2016.
- [5] Aldo Bonfiglioli and Renato Paciorri. Convergence analysis of shock-capturing and shock-fitting solutions on unstructured grids. *AIAA Journal*, 52(7):1404–1416, 2014.
- [6] Graham V. Candler, Pramod K. Subbareddy, and Joseph M. Brock. Advances in computational fluid dynamics methods for hypersonic flows. *Journal of Spacecraft and Rockets*, 52(1):17–28, January 2015.
- [7] Eric J. Ching, Yu Lv, Peter Gnoffo, Michael Barnhardt, and Matthias Ihme. Shock capturing for discontinuous Galerkin methods with application to predicting heat transfer in hypersonic flows. *Journal of Computational Physics*, 376:54–75, January 2019.
- [8] Mirco Ciallella, Mario Ricchiuto, Renato Paciorri, and Aldo Bonfiglioli. Extrapolated Shock Tracking: Bridging shock-fitting and embedded boundary methods. *Journal of Computational Physics*, 412:109440, July 2020.
- [9] Bernardo Cockburn and Chi-Wang Shu. Runge–Kutta discontinuous Galerkin methods for convection-dominated problems. *Journal of Scientific Computing*, 16(3):173–261, September 2001.
- [10] Andrew T. Corrigan, Andrew D. Kercher, and David A. Kessler. A moving discontinuous Galerkin finite element method for flows with interfaces. *International Journal for Numerical Methods in Fluids*, 89(9):362–406, 2019.
- [11] Andrew T. Corrigan, Andrew D. Kercher, David A. Kessler, and Devon A. Wood-Thomas. Convergence of the Moving Discontinuous Galerkin Method with Interface Condition Enforcement in the Presence of an Attached Curved Shock. AIAA Paper 2019-3207, June 2019.
- [12] Luke M. D’Aquila, Brian T. Helenbrook, and Alireza Mazaheri. A novel stabilization method for high-order shock fitting with finite element methods. *Journal of Computational Physics*, 430:110096, April 2021.
- [13] Alain Dervieux, David Leservoisier, Paul-Louis George, and Yves Coudière. About theoretical and practical impact of mesh adaptation on approximation of functions and PDE solutions. *International Journal for Numerical Methods in Fluids*, 43(5):507–516, 2003.
- [14] Pablo Fernandez, Cuong Nguyen, and Jaime Peraire. A physics-based shock capturing method for unsteady laminar and turbulent flows. Kissimmee, Florida, January January 2018. AIAA Paper 2018-0062.

- [15] Markus Geisenhofer, Florian Kummer, and Martin Oberlack. An extended discontinuous Galerkin method for high-order shock-fitting. *arXiv:2012.08860 [physics]*, December 2020.
- [16] Philip E. Gill, Walter Murray, and Margaret H. Wright. *Practical Optimization*. Academic Press, London ; New York, 1981.
- [17] J. Glimm, X.-L. Li, Y.-J. Liu, Z.-L. Xu, and N. Zhao. Conservative front tracking with improved accuracy. *SIAM Journal on Numerical Analysis*, 41(5):1926–1947, 2003.
- [18] A. Harten and J. M. Hyman. Self adjusting grid methods for one-dimensional hyperbolic conservation laws. *Journal of Computational Physics*, 50(2):235–269, 1983.
- [19] Ami Harten, Bjorn Engquist, Stanley Osher, and Sukumar R Chakravarthy. Uniformly high order accurate essentially non-oscillatory schemes, III. *Journal of Computational Physics*, 71(2):231–303, August 1987.
- [20] Ami Harten and James M Hyman. Self adjusting grid methods for one-dimensional hyperbolic conservation laws. *Journal of Computational Physics*, 50(2):235–269, May 1983.
- [21] Danny Hermes and Per-Olof Persson. High-order solution transfer between curved triangular meshes. *arXiv:1810.06806 [math]*, October 2018.
- [22] Jan S. Hesthaven and Tim Warburton. *Nodal Discontinuous Galerkin Methods: Algorithms, Analysis, and Applications*. Texts in Applied Mathematics. Springer-Verlag, New York, 2008.
- [23] Guang-Shan Jiang and Chi-Wang Shu. Efficient implementation of weighted ENO schemes. *Journal of Computational Physics*, 126(1):202–228, June 1996.
- [24] Andrew D. Kercher and Andrew Corrigan. A least-squares formulation of the Moving Discontinuous Galerkin Finite Element Method with Interface Condition Enforcement. *Computers & Mathematics with Applications*, pages 1490–1519, November 2020.
- [25] Andrew D. Kercher, Andrew Corrigan, and David A. Kessler. The moving discontinuous Galerkin finite element method with interface condition enforcement for compressible viscous flows. *International Journal for Numerical Methods in Fluids*, 93(5):1490–1519, 2021.
- [26] Patrick M. Knupp. Algebraic mesh quality metrics. *SIAM Journal on Scientific Computing*, 23(1):193–218, January 2001.
- [27] Theodore Kai Lee and Xiaolin Zhong. Spurious numerical oscillations in simulation of supersonic flows using shock-capturing schemes. *AIAA Journal*, 37(3):313–319, 1999.
- [28] Michel Lesoinne, Marcus Sarkis, Ulrich Hetmaniuk, and Charbel Farhat. A linearized method for the frequency analysis of three-dimensional fluid/structure interaction problems in all flow regimes. *Computer Methods in Applied Mechanics and Engineering*, 190(24):3121–3146, March 2001.
- [29] Xu-Dong Liu, Stanley Osher, and Tony Chan. Weighted essentially non-oscillatory schemes. *Journal of Computational Physics*, 115(1):200–212, November 1994.
- [30] Andrew Majda. *Compressible fluid flow and systems of conservation laws in several space variables*, volume 53. Springer Science & Business Media, 2012.
- [31] G. Moretti. Thirty-six years of shock fitting. *Computers & Fluids*, 31(4-7):719–723, 2002.
- [32] Jorge Nocedal and Stephen Wright. *Numerical Optimization*. Springer Science & Business Media, 2006.
- [33] Per-Olof Persson and Jaime Peraire. Sub-cell shock capturing for discontinuous Galerkin methods. AIAA Paper 2006-112, January 2006.
- [34] Per-Olof Persson and Gilbert Strang. A simple mesh generator in MATLAB. *SIAM Review*, 46(2):329–345, January 2004.

- [35] P. S. Rawat and X. Zhong. On high-order shock-fitting and front-tracking schemes for numerical simulation of shock–disturbance interactions. *Journal of Computational Physics*, 229(19):6744–6780, 2010.
- [36] Xevi Roca, Abel Gargallo-Peiró, and Josep Sarrate. Defining quality measures for high-order planar triangles and curved mesh generation. In William Roshan Quadros, editor, *Proceedings of the 20th International Meshing Roundtable*, pages 365–383, Berlin, Heidelberg, 2012. Springer.
- [37] M.D. Salas. *A shock-fitting primer*. CRC Press, 2009.
- [38] G. R. Shubin, A. B. Stephens, and H. M. Glaz. Steady shock tracking and Newton’s method applied to one-dimensional duct flow. *Journal of Computational Physics*, 39(2):364–374, 1981.
- [39] G. R. Shubin, A. B. Stephens, H. M. Glaz, A. B. Wardlaw, and L. B. Hackerman. Steady shock tracking, Newton’s method, and the supersonic blunt body problem. *SIAM Journal on Scientific and Statistical Computing*, 3(2):127–144, 1982.
- [40] J.-Y. Trepanier, M. Paraschivoiu, M. Reggio, and R. Camarero. A conservative shock fitting method on unstructured grids. *Journal of Computational Physics*, 126(2):421–433, 1996.
- [41] Bram Van Leer. Towards the ultimate conservative difference scheme. V. A second-order sequel to Godunov’s method. *Journal of Computational Physics*, 32(1):101–136, 1979.
- [42] J. Van Rosendale. Floating shock fitting via lagrangian adaptive meshes. Technical Report ICASE Report No. 94-89, Institute for Computer Applications in Science and Engineering, 1994.
- [43] Z. J. Wang, Krzysztof Fidkowski, Rémi Abgrall, Francesco Bassi, Doru Caraeni, Andrew Cary, Herman Deconinck, Ralf Hartmann, Koen Hillewaert, H. T. Huynh, Norbert Kroll, Georg May, Per-Olof Persson, Bram van Leer, and Miguel Visbal. High-order CFD methods: current status and perspective. *International Journal for Numerical Methods in Fluids*, 72(8):811–845, 2013.
- [44] Jian Yu and Jan S. Hesthaven. A study of several artificial viscosity models within the discontinuous galerkin framework. *Communications in Computational Physics*, 27(5):1309–1343, 2020.
- [45] Matthew J. Zahr and Per-Olof Persson. An optimization-based approach for high-order accurate discretization of conservation laws with discontinuous solutions. *Journal of Computational Physics*, 365:105–134, July 2018.
- [46] Matthew J. Zahr and Per-Olof Persson. An r-adaptive, high-order discontinuous Galerkin method for flows with attached shocks. In *AIAA Scitech 2020 Forum*. American Institute of Aeronautics and Astronautics, 2020.
- [47] Matthew J. Zahr and Joseph M. Powers. High-order resolution of multidimensional compressible reactive flow using implicit shock tracking. *AIAA Journal*, 59(1):150–164, December 2020.
- [48] Matthew J. Zahr, Andrew Shi, and Per-Olof Persson. Implicit shock tracking using an optimization-based high-order discontinuous Galerkin method. *Journal of Computational Physics*, 410:109385, June 2020.